Development of a Magnetoelastic Resonance Sensing System for Water Cut Applications

by
Liam Swanepoel

Thesis presented in partial fulfilment of the requirements for the degree of Master of Engineering (Mechatronic) in the Faculty of Engineering at Stellenbosch University

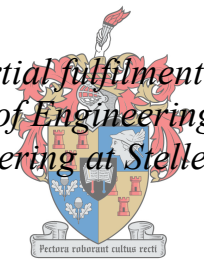

UNIVERSITEIT
iYUNIVESITHI
STELLENBOSCH
UNIVERSITY

Supervisor: Dr. Cobus Müller
Co-supervisor: Dr. Jurgen Kosel

December 2018

DECLARATION

By submitting this thesis electronically, I declare that the entirety of the work contained therein is my own, original work, that I am the sole author thereof (save to the extent explicitly otherwise stated), that reproduction and publication thereof by Stellenbosch University will not infringe any third party rights and that I have not previously in its entirety or in part submitted it for obtaining any qualification.

Date: December 2018

Plagiaatverklaring/*Plagiarism Declaration*

1 Plagiaat is die oorneem en gebruik van die idees, materiaal en ander intellektuele eiendom van ander persone asof dit jou eie werk is.
Plagiarism is the use of ideas, material and other intellectual property of another's work and to present is as my own.

2 Ek erken dat die pleeg van plagiaat 'n strafbare oortreding is aangesien dit 'n vorm van diefstal is.
I agree that plagiarism is a punishable offence because it constitutes theft.

3 Ek verstaan ook dat direkte vertalings plagiaat is.
I also understand that direct translations are plagiarism.

4 Dienooreenkomstig is alle aanhalings en bydraes vanuit enige bron (ingesluit die internet) volledig verwys (erken). Ek erken dat die woordelikse aanhaal van teks sonder aanhalingstekens (selfs al word die bron volledig erken) plagiaat is.
Accordingly all quotations and contributions from any source whatsoever (including the internet) have been cited fully. I understand that the reproduction of text without quotation marks (even when the source is cited) is plagiarism.

5 Ek verklaar dat die werk in hierdie skryfstuk vervat, behalwe waar anders aangedui, my eie oorspronklike werk is en dat ek dit nie vantevore in die geheel of gedeeltelik ingehandig het vir bepunting in hierdie module/werkstuk of 'n ander module/werkstuk nie.
I declare that the work contained in this assignment, except otherwise stated, is my original work and that I have not previously (in its entirety or in part) submitted it for grading in this module/assignment or another module/assignment.

16968298 **Studentenommer / *Student number***	**Handtekening / *Signature***
L Swanepoel **Voorletters en van / *Initials and surname***	**04/09/2018** **Datum / *Date***

Abstract

Precise measurement of the water fraction in oil (i.e. water cut) is of critical importance in numerous applications. In the oil and gas industry, for example, knowledge of the amount of water production and where it comes from is necessary before any remedial action can be taken. Currently, cost-effective, reliable and accurate measurement technologies capable of full range three phase measurements are not commercially available.

The development of an ultra-low power, low-cost, wireless and non-corrosive resonance sensor is considered. The sensor is based on magnetoelastic technology that has been implemented by an amorphous ribbon and electromagnetic interrogation. The magnetoelastic ribbon's resonant frequency is dependent on the vibrational damping effect of the surrounding medium, which in turn is determined by the dynamic viscosity of the medium. This enables distinguishing all three gas, water, and oil phases with measured sensor signal amplitude changes of 75% and 99% and resonant frequency shifts of 0.46% and 3.88% respectively, compared to the gas phase. The sensor shows sensitivity in the water-cut range from 10% - 90% WC and is characterised by a linear response from 10% - 80% WC. When immersed in water/oil emulsions the sensor power consumption ranges from 160 nW to 500 nW. A rapid decay of the magnetic properties has been observed in high salinity solutions due to corrosion of the sensor material, which represent typical environments in industrial applications. A solution for this has been found through coating the sensor ribbons with Teflon by dip coating, acting as an anti-corrosion layer that enables sensor deployment for extended periods of time in harsh environments. This study shows that a magnetoelastic resonance sensor possesses the required characteristics and sensitivity which make it suitable for use in water-cut applications. The possibility of inline WC measurement has been explored through the design of a modified sensor housing. The sensor incorporates a set of excitation and detection coils and allows the flow of liquid across the amorphous ribbon surface. Tests conducted in a flowrate controlled water flow loop show a shift of 150 Hz in resonant frequency from flowrates of 0.2 m/s – 0.63 m/s due to the increased surface drag on the sensor surface. However, this is considered insignificant as viscosity induced shifts are in the kHz range, therefore concluding that the sensor is insensitive to variations in flow rate.

Furthermore, the sensor system design is expanded as a Portable Readout Device (PRD) capable of in-field measurements. The design consists of a battery powered microcontroller

circuit that integrates with a smartphone via a mobile application. The peak frequency data sampled from the sensor is displayed on the smartphone. The PRD sampling algorithm has been tested with a 100% correlation in sampled data compared to a bench setup using Helmholtz coils and an oscilloscope. The PRD consumes 3.25 W of power during sampling and is capable of remote operation through the implementation of Bluetooth connectivity.

Opsomming

Die akkurate monitering van waterinhoud in olie is belangrik in menige toepassings. Met die olie en gas industrie as voorbeeld, moet daar inligting wees oor die waterinhoud in ruolie voor enige poging om die olie uit die grond uit te haal kan begin. Tans bestaan daar geen koste effektiewe, betroubare en akkurate waterinhoud moniteringstelsel vir vol-spektrum drie-fase monitering nie.

Die ontwikkeling van ‘n lae-drywing, lae-koste, koordlose en korrosie bestande resonansie sensor word oorweeg. Die sensor is gebaseer op magneto-elastiese tegnologie wat geïmplementeer is met ‘n metaal strokie en elektromagnetiese induksie. Die metaal strokie se resonante frekwensie word beïnvloed deur die dinamiese viskositeit van die omliggende medium. Dit bemoontlik die identifisering van al drie fases naamlik: gas, water en olie. Die sein wat gemeet word deur middel van induksie ervaar amplitude demping van 75% en 99% en resonante frekwensie veranderinge van 0.46 % en 3.88 % vir water en olie onderskeidelik, gemeet relatief tot lug as gas media. Die sensor is sensitief vir veranderinge in media van 10% - 90% water inhoud, maar kan liniêr gekarakteriseer word tussen 10% - 80% waterinhoud. Tydens monitering in olie en water emulsies wissel die elektriese drywingsbehoeftes tussen 160 nW en 500 nW. ‘n Spoedige afname in magnetiese karakteristieke en werking word gesien na gebruik in hoë soutinhoud media, wat aandui dat die sensormetaal korrodeer. ‘n Oplossing is gevind deur die sensor met ‘n laag Teflon te bedek deur middel van dip-dekking. Die Teflon laag beskerm die sensormetaal teen korrosie en laat die gebruik in korrosiewe omgewings vir lang periodes op ‘n slag toe. Hierdie studie bewys dat ‘n magneto-elastiese sensor die nodige sensitiwiteit en karakteristieke besit vir gebruik in water-in-olie moniterings toepassings. Die in-lyn implimentering van die sensor in ‘n pyplyn is ondersoek deur die ontwikkeling van ‘n aangepaste sensor omhulsel. Die omhulsel bestaan uit ‘n primêre en sekondêre induktor waarop die metaal strokie gemonteer is. Die ontwerp van die sekondêre induktor stel die medium in staat om oor die sensor oppervlak te vloei. ‘n Totale verskuiwing in resonante frekwensie van 150 Hz is gemeet vir vloeitempo’s van 0.2m/s tot 0.63 m/s. Hierdie verskuiwing is as gevolg van toenemende sleur kragte wat inwerk op die sensor oppervlak, maar word ignoreer in die lig van kHz grote-orde verskuiwings wat gemeet word as gevolg van veranderinge in media viskositeit. Die sensor word dus beskou as onsensitief tot veranderinge in die media vloeitempo.

Die sensor sisteem word uitgebrei deur middel van ‘n handtoestel vir buitelug metings. Die sisteem is geïntegreer met ‘n mikrobeheerder wat met ‘n battery aangedryf word en kommunikeer met ‘n slimfoon. Die slimfoon lewer instruksies aan die mikrobeheerder en word ook gebruik om die data vanaf die sensor sisteem te toon aan die verbruiker. Die algoritme wat in beheer is van die monitering van die sensor is getoets teenoor ‘n ossilloskoop en Helmholtz induktors met 100% korrelasie in metings. Die operationele sensor sisteem verbruik slegs 3.25 W drywing en skakel met die slimfoon deur draadlose Bluetooth kommunikasie.

Acknowledgements

I would like to express my sincerest gratitude to my parents who have supported me during every phase of my life, whose phone calls motivated me to press on and do what needed to be done. Thank you to Kaylynn and Bertus, who were the voices of reason during this period and reminded me why we do what we do. Thank you to Cobus Müller, whose guidance and high standards are reflected in this work. Also, thank you to Cobus Visser, who aided me when staring at a seemingly unsolvable design problem during the beginning phases of this project.

Thank you to Jürgen, who gave me an opportunity awarded to few. Being part of an academic institution like KAUST is the highest of honors, and working with a team as highly motivated and capable as the SMM group is truly inspiring. What I learned there I will take with me through my entire career.

Lastly, thank you to all the technical staff at Stellenbosch University and King Abdullah University of Science and Technology. Whether its cleaning the offices late after everyone is gone and early morning before everyone comes in (Jenrico), or helping with a quick machining solution (Julian and PJ) or supplying a required electrical component - this project would have been far less of a pleasure if not for your efforts.

Contents

List of Figures

List of Tables

1. Introduction

1.1. Background

In the oil industry water is produced as a by-product when extracting oil or gas from a reservoir. This water, called "produced water", is located either under the oil body or within the same zone. Since the underground pressure is not sufficient to force the oil to the surface, various enhanced oil recovery (EOR) methods are applied to stimulate oil production. One of these EOR methods is the injection of water through pipelines to increase the pressure within the well and force the oil to the surface. While traditional oil production can recover up to 35-45% of the original oil, the application of water injection and other similar techniques may add an additional 5-15%, thereby extending the life of the oilfield (Tzimas et al, 2005). The injected water eventually reaches the production wells. The high viscosity and emulsified water droplets in sludge have a significant impact on the dewatering efficiency and de-oiling efficiency, as well as recovering oil quality (Zheng et al, 2017). The cost of managing produced water is as high as $5/barrel and is a significant factor in the profitability of oil and gas production. This cost includes the construction and operation of treatment and disposal facilities, the acquisition of chemical additives and the transportation of byproducts ("About produced water", 2016).

Water cut (WC) sensors are implemented to monitor production parameters including multiphase flow rates and contactless water fraction of produced hydrocarbons. Detection may be done in-line at production plants or downhole, thereby allowing the quantification of produced water quantity. The inline detection of water fraction in oil is achieved either by measuring the mixture viscosity, the effective electric permittivity, or IR/gamma-ray absorption characteristics of oil-water mixtures (Karimi et al, 2016). Downhole WC measurement presents both challenges and opportunities. The challenge is that the design of the metering hardware must withstand the harsh conditions where hydrostatic pressure and

temperature can reach 206 MPa and 232 °C, respectively. Due to high pressure, water is likely to be absent in its gas phase, thereby simplifying the system design (Xiao, 2015). Technical advances in electronics, low-power sensors, and wireless communications have enabled a paradigm shift in wireless monitoring and control for an extensive range of applications in the oil and gas industry. The abundance of remote and hazardous locations in the industry has fueled an increasing demand for remote sensor applications (Ahmad et al, 2015). With the ever-growing energy demand and the proliferation of multilateral oil wells, the need for low-cost WC sensing nodes used in both horizontal as well as vertical installations has increased. The real-time monitoring through inline WC sensors allows for efficient reservoir management and production allocation. WC sensors currently available are either costly, heavy, intrusive, severely sensitive to water salinity or incapable of covering the full WC range (Karimi et al, 2017; Black et al, 2013).

In this study, a novel WC sensor based on magnetoelastic resonance technology is proposed that provides real-time information about water-in-oil concentrations remotely. Magnetoelastic sensors have been utilized for various sensing applications (Kaniusas et al, 2006; Mehnen et al, 2004; Viswanath et al, 2013) while providing high performance and wireless operation (Kosel et al, 2005; Traxler et al, 2008). This includes the monitoring of several physical parameters like temperature, humidity, pressure, flow viscosity and the viscosity of liquids (Grimes et al, 2002). The proposed sensor consists of a magnetoelastic ribbon in combination with an interrogation module that electromagnetically excites and detects flux changes in the soft magnetic ribbon. The sensor is scalable in size and consequently resonating frequency, meaning it can be altered for a specific bore diameter and avoiding frequency noise that may be present. Such a sensor requires very little power due to the low biasing field required to excite a signal from the ribbon. Furthermore, a biasing field can be provided by an additional magnetised ribbon, shown in this study. With a thickness of 28 µm, the ribbon and its mechanical resonant frequency are sensitive to slight changes in surface damping caused by viscosity changes in the surrounding medium. The characteristic behavior of the ribbon vibration is modelled as:

$$\Delta f = \frac{\sqrt{\pi f_o}}{2\pi\rho_s d}\sqrt{\eta\rho_l}, \tag{1.1}$$

where f_o is the resonant frequency of the ribbon in a vacuum, ρ_s and d the density and thickness of the ribbon respectively, and η and ρ_l the effective dynamic viscosity and density of the surrounding medium. The frequency shift measured is, therefore, a function of the viscosity-density product of the medium, and thus also of the WC.

1.2. Motivation

The development of a novel magnetoelastic resonance-based sensor system for water-cut applications is considered. The exploration of oil reservoirs using EOR methods result in large quantities of produced water mixed in with the crude oil in production wells. The measurement of WC inline or downhole across the full 0-100% WC range allows for the optimization of production, control, and management of processes in applications with high water-in-oil content. This will allow for the extraction of oil from half depleted wells. As previously mentioned, current WC sensors suffer from a range of drawbacks that includes cost, availability, sensitivity, intrusiveness, and resolution. This makes a WC sensor free of these drawbacks an attractive option for commercial use.

Laboratory methods of WC detection are accurate but not appropriate for real-time monitoring of water content during oil production (Karimi, 2016). Apart from the equipment not being application specific, a key reason for this may be the heavy and non-portable nature of the required laboratory equipment. A functional, portable and practical magnetoelastic sensor system requires compact design, portability, ease of operation and reliability in terms of signal-to-noise ratio (Grimes et al, 2011).

1.3. Research Objectives

The aim is the development of an innovative method of water-cut measurement that utilises the magnetostrictive and magnetoelastic characteristics of an amorphous ribbon. The system magnetically excites an amorphous ribbon and detects the resonant signal response using induction coils. A benchtop analysis to determine an adequate resolution suitable for peak detection is performed. An algorithm is developed that utilizes this information and calculates the WC of the oil-water mixture.

Following the validation of the concept, focus is placed on the development of a Portable Readout Device (PRD) capable of in-field and remote measurements. To increase the portability of the system, it integrates with a smartphone that records and displays the results of the measurement. The system is battery powered. A benchtop analysis is performed to determine an adequate sampling rate for sensor signal acquisition. The sensor is optimized for continuous use and exposure to corrosive conditions through the addition of a non-corrosive layer.

1.4. Outline

This study commences with a literature survey in Chapter 2, which offers the necessary insight into several relevant topics and presents evidence and theoretical background required for decisions made during the study. Chapter 3 presents the principle approach to measuring the WC of a non-homogeneous mixture using magnetoelastic technology and magnetic induction. This includes the validation of the concept. Chapter 4 describes the detailed design phases that were followed in the development of a modular microcontroller-based WC sensing system. Specific complications and pitfalls in the use of the system are anticipated and addressed in Chapter 5. Chapter 6 concludes the study and recommends the course for future work that is built on this topic.

2. Literature Survey and Theory

2.1. Overview

A healthy growth in the oil and gas industry has been fueled by the proliferation of the world's reliance on fossil fuels. With the increase in energy demand over the past century, oil conglomerates have gradually increased their yearly production. The International Energy Agency (IEA) reported in their yearly *Oil Market Report* (IEA, 2018) a world demand increase from 91 million barrels per day (mb/d) in 2013 to 97 in 2017. BP Global (2016) states that a proved oil reserve of 1717 billion barrels will last 50.6 years at current production levels. Adelman (2004) states that as well output falls over time with decreased pressure, the unit operating cost of the well's output will rise. This includes the cost of further exploration of half depleted wells and an increased dependency on EOR methods for improved production. Furthermore, when the operating cost rises above the price that the oil will fetch on the marketplace, the well will shut down. Any oil left underground will not be worth producing, given current prices and technology.

Watercut in oil exploration, transportation and storage is a vital parameter to assess crude oil production accurately (Song, 2016). Due to water flooding and other EOR techniques currently in use in oil exploration, the water content in the majority of mines are high. As a result, sensors capable of measurement in the high WC range are required. The technology proposed in this study is based on the detection of density and viscosity (density/viscosity product) changes in an oil-water mixture. The vibration of the amorphous ribbon is sensitive to damping induced by the surrounding medium. A medium with a viscosity of 1 g/cm·s will produce a sharp spike in the sensor signal at the resonant peak due to low damping, whereas a medium with a viscosity of 1000 g/cm·s will create more damping and result in a smaller peak at resonance. This means that the sensor will possess a greater sensitivity at higher WCs due to a sharp measurable peak. An important consideration with the use of this technology and the validation thereof is the rheological behavior of oil-water mixtures with different ratios. Oil and water

together form an immiscible liquid or emulsion. The emulsion consists of a dispersed phase suspended in a continuous phase which exhibits non-Newtonian fluid behavior. This means that the rheological behavior and viscosity/density product of the oil-water emulsions used in the validation of the sensor must be accurately modelled. Subsequently, the calculated theoretical frequency shift is compared to the sensor response to support the experimental results.

2.2. Magnetoelastic Sensors

Magnetostrictive resonance sensors have been well researched over the past two decades. They have been used for various applications, including sensing and actuation. Regarding sensing applications, multiple papers have been published on the detection and measurement of fluid flow rate (Kouzoudis et al, 2000), temperature (Mungle et al, 2002), pressure (Kouzoudis et al, 2000) and liquid viscosity and density (Grimes et al, 2000; Stoyanov, 2000; Loiselle, 2000). There are numerous benefits to wireless sensor systems. For example, in technical applications measurements inside fully closed objects is possible. More specifically, in biomedical applications the sensors can be implanted and accessed without transcutaneous wires or catheterization, thereby drastically reducing the discomfort of the patients (Kosel et al, 2007). Changes in viscosity of the fluid on the surface of the ribbon, or changes in force loadings will affect the damping and alter the harmonic response (Green, 2008). The theoretical model of the magnetoelastic ribbon (Equation 1.1) is derived from the equation of motion and is presented in Appendix A.

Magnetoelastic sensors consist of a single or multiple magnetoelastic ribbons, made from an amorphous alloy. As described by Stoyanov and Grimes (2000), magnetoelastic amorphous ferromagnetic alloys are made by rapid melt-quenching with a constant magnetic field across the width of the ribbon to define an easy axis. When magnetised with an oscillating magnetic field, magnetoelastic alloys efficiently translate magnetic energy into elastic energy in the form of longitudinal vibrations which mechanically deforms the material. Furthermore, this mechanical

deformation is greatest along the easy axis at the resonant frequency which is inversely proportional to the sample length. The induced magnetostrictive strain within the material act to generate magnetic flux that can be detected using a remotely located pickup coil (Stoyanov & Grimes, 2000).

All the applications mentioned up to now were completed with the required use of laboratory amplifiers and impedance analysers. This means that the measurement system is heavy and immobile. To address this problem, Zeng (2006) described a microcontroller-based design that uses four solenoid coils and a computer-generated user interface (GUI) to detect vibrations from the resonance sensor through impedance measurement. However, since the authors used a computer to visualise the results their system is not fully portable, which means that improvements can be made. This work proves that a Portable Readout Device (PRD) can be constructed and used to excite a magnetic response from a magnetoelastic sensor.

2.3. Magnetostriction and the Magnetoelastic Effect

Magnetostriction is a phenomenon that occurs in all ferromagnetic materials during magnetization and causes them to change their shape or dimensions. During magnetization, a material is subjected to a magnetic field, causing the magnetic dipoles to rotate parallel with the applied magnetic field (See Figure 1(a)). This creates a magnetic domain which is an area wherein the magnetic dipoles all point in the same direction. As the applied magnetic field is increased the magnetic domain grows, resulting in the decrease of other domains present (See Figure 1(b)). When the applied magnetic field direction is changed the magnetic dipole molecules change shape slightly, making the crystal lattice longer in one direction and shorter in the other dimensions. However, since the magnetic domain boundaries are held rigid by the surrounding material, it cannot change shape. Instead, mechanical stresses are induced in the material, which changes the magnetic permeability of the material. These changes in magnetic permeability cause a change in magnetic flux around the sample when excited.

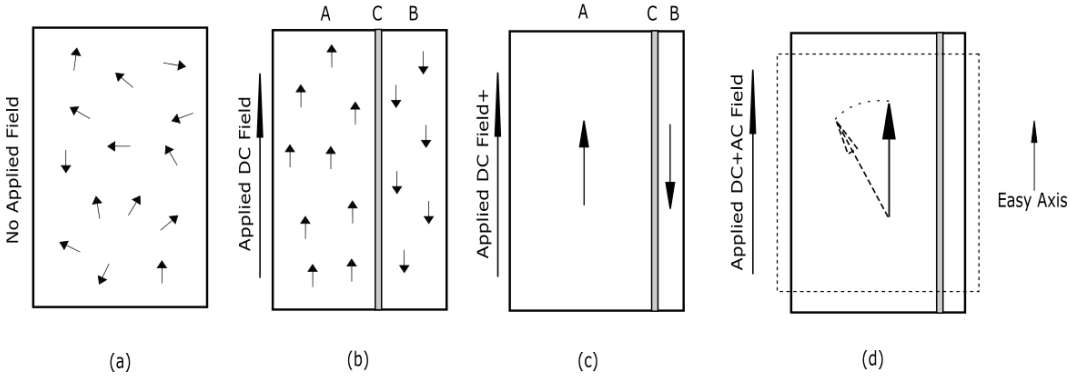

Figure 1: (a) Unmagnetised material showing the random orientation of magnetic dipoles. (b) A magnetic biasing field is applied along the easy axis and the magnetic dipoles align, creating magnetic domains A and B, separated by a domain wall C. (c) When a larger magnetic field is applied domain A increases in size until the entire sample is magentised. (d) When the sample is magnetised and an alternative magnetic field is applied, the magnetic dipoles rotate, creating internal stresses that change the material's magnetic permeability and dimensions (Primarily along the easy axis).

2.4. Excitation and Detection Methods

Magnetic excitation of the amorphous ribbon is achieved by sending an alternating current through an inductor. The generated magnetic field causes the ribbon to vibrate and subsequently generate magnetic flux changes around the ribbon. Various techniques have been used to detect resonant frequencies from magnetoelastic sensors.

2.4.1. Magnetic induction

According to *Faradays Laws of Induction*, a current is generated in the inductor directly proportional to the change in magnetic flux through the coil. With knowledge of the impedance of the coil, the voltage over the two coil ends can be used to characterise the sensor response. Alternatively, an impedance measurement device (Impedance Analyser) can be used to determine the resonant frequency of the sensor. The impedance analyser measures the change in impedance due to a change in magnetic permeability caused by magnetostriction over a frequency band. This method is advantageous in applications where the medium surrounding the

ribbon is not restricted to air. It is equally effective when the sensor is very small (few mm) because the resulting vibrations in the sensor are in the MHz range and nearly undetectable through alternative methods. The downside to this is that the pickup coil must be close to the ribbon and its orientation locked co-axially to the easy axis of the ribbon to ensure the maximum measured amplitude. Figure 2 below shows the co-axial orientations of the excitation and pickup coils.

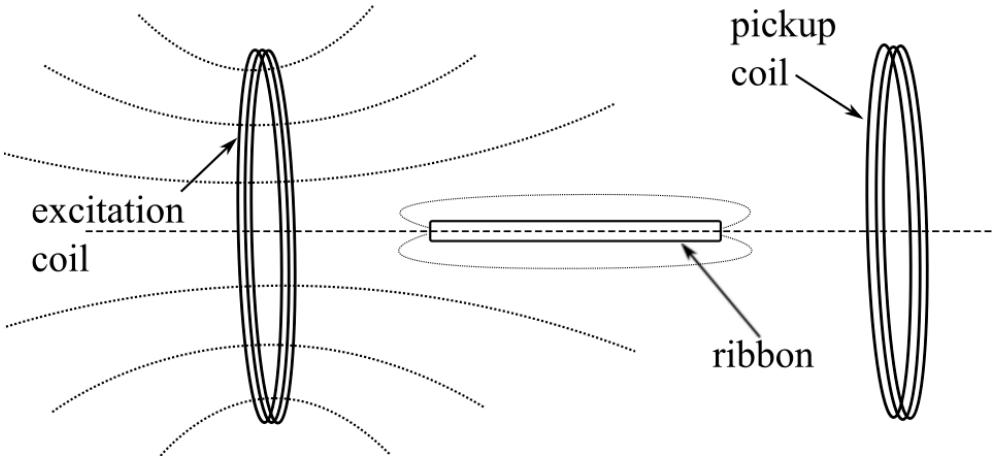

Figure 2: An excitation coil generates a magnetic field that is time-varying in nature. This excites flux changes around the ribbon, which is detected with the pickup coil. The measured signal amplitude increases with a reduction in distance from the ribbon.

2.4.2. Optical reflection and detection

Another method for detecting the resonant frequency of a ribbon in air is by using an infra-red source (laser) and sensor. A laser beam is reflected from the surface of the sensor as shown in Figure 3, and the response of the sensor characterised by recording the changes in the returned beam intensity (Grimes et al, 2002). Since the amorphous ribbon is magnetostrictive, it vibrates longitudinally. A laser shined onto the reflective surface of the ribbon will produce a reflection on an infra-red eye (sensor) if correctly positioned. The output from the sensor can be used to determine the vibrational amplitude and frequency of the ribbon. This method is advantageous in applications where the medium surrounding the ribbon is restricted to air (or a vacuum) and the reflective surface is unobstructed. This method is not

feasible in any other medium that will cause refraction or obstruction of the laser beam.

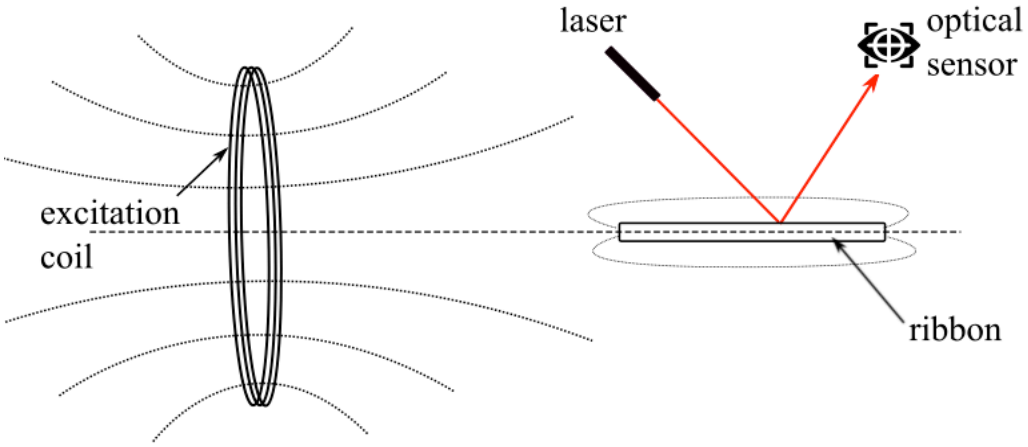

Figure 3: Vibrations in the ribbon is excited with the excitation coil. A laser beam reflected from the ribbon surface is detected with an optical sensor.

2.4.3. Audio detection

Another effective method of detecting the longitudinal vibrations in the amorphous ribbon is by using a microphone. The flux vibrations of the sensor generate an acoustic wave that can be detected using a microphone in air or hydrophone liquid (Grimes, et al, 2002). If the excitation frequency is within the audible range (0 – 20 kHz), or the ribbon is resonating, a microphone can detect the audio signal. At resonance, higher and lower order harmonics appear. If the resonant frequency is outside the audible range, the lower order harmonics are still detectable. This method is restricted to applications where the surrounding medium is air and a frequency within the audible range can be excited.

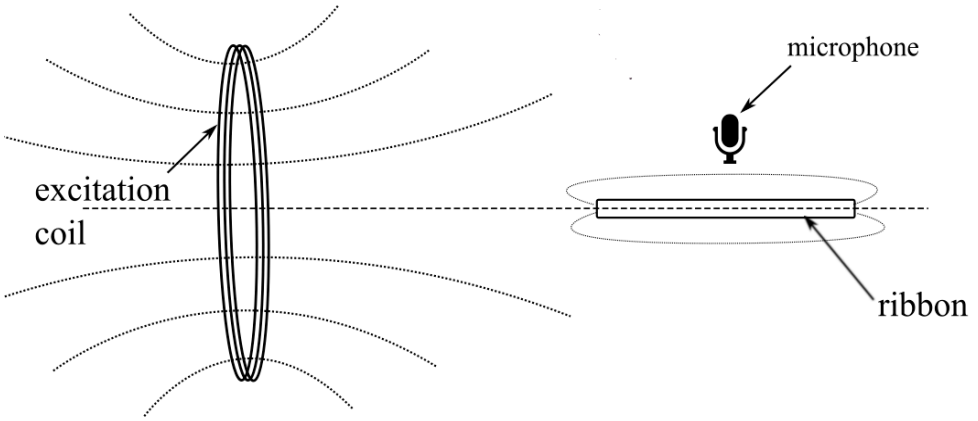

Figure 4: A microphone is positioned proximal to the ribbon and detects the audible vibrations of the ribbon at resonance.

2.5. Water Cut Measurement Technologies

Measuring water cut is crucial for the optimization of processes in the oil industry as the amount of water present in the oil greatly influence the cost of production (Hatimoor, 2013). Inline detection of water fraction in oil can be done by sensing the differences in viscosity, effective electric permittivity (Jakoby et al, 2004), or IR/microwave/gamma-ray absorption characteristics of oil/water mixtures (Warren et al, 2003). Various commercial solutions exist, each with different implementations and performance as shown in Table 1.

Table 1: Comparison of commercial water cut meters.

Reference	Manufacturer	Range	Uncertainty	Sensitivity
Flo·Point, 2018	Flo·Point	0% -100%	±1%	0.5%
Weatherford, 2018	Weatherford	0% -100%	±2%*	0.01%
Roxar, 2018	Roxar	1% - 15%	±5%	0.005%
		1% - 50%	±5%	0.005%
		0% -100%	±1%	0.05%
KAM, 2018	KAM	0% - 20%	±0.2%	0.01%
		0% - 30%	±0.3%	0.01%
		0% - 40%	±0.4%	0.01%
		0% -100%	±1%	0.01%

*With GVF of 20%

2.5.1. Capacitance/RF Measurement (Sub-Microwave frequency)

Electrical sensors based on capacitive measurements or radio frequency resonators measurements (s-parameters) are two different approaches that can be used to analyse the water-in-oil content of emulsions, although both measure impedance (Conchouso et al, 2016). The use of capacitance-based measurement technology has been well established in the oil and gas industry for almost five decades. The technology exploits the difference in dielectric properties between oil (~2) and water (~75) (Hatimoor, 2013). The effective capacitance of the dual-phase mixture is measured by transmitting a radio frequency voltage across the sensing elements. Prior knowledge of the capacitance of both oil and water is required. The effective capacitance increases with increasing water cut and vice versa (Hatimoor, 2013). A commercially available WC sensor, like the sensor produced by Delta-C (DC-1510 Series), is based upon the capacitance measurement of the oil/water mixture, which can cover a limited WC range. Hammer (1989) characterised a non-intrusive helical shaped surface plate electrode system with ±1.5 % water fraction for 0% - 15% water content and ±1% for 0% - 80% with a repeatability of 1%. At high WCs the water becomes the continuous phase and the mixture becomes conductive, at which point a conductive measurement method is required (Demori et al, 2015; Al-Taweel et al, 2000). Key advantages of capacitive instruments are its simple design and insensitivity to water conductivity up to inversion. In addition, capacitive instruments are among the lowest cost options, while performing very well in most common applications. Noted disadvantages of capacitive instruments are, however, their difficulty in handling changing process factors and their limitations in measurement range (Hatimoor, 2013). While these sensors are useful for applications with remarkably stable process conditions and low water cut, a limitation is the dependency on periodic recalibration to maintain accuracy (Emerson Process Management, 2016). Furthermore, capacitive sensing is categorised by the excitation frequency of measurements. The low excitation frequency (in the kHz range) measurement method is known to suffer from short circuit effects between the capacitor electrodes in the presence of a conductive

medium (i.e., in the case of high WCs after inversion); thereby, making this method not applicable for WC measurement beyond 70% WC (Karimi, 2016).

2.5.2. Spectroscopic/Infrared absorption

Spectroscopic measurement is performed by emitting infrared light across a narrow slot filled with oil/water mixture. The receptors measure absorption, reflection and scatter of the infrared beam and derive the watercut from the results (Basrawi, 1999). Spectroscopic measurement instruments have the advantage of being one of the few technologies that can measure across the full watercut range. The error is found to decrease with increasing watercut, unlike capacitive instruments. Furthermore, this measurement technology is unaffected by changes in density, salinity and entrained gas (Hatimoor, 2013). Major disadvantages with spectroscopic-based measurement devices are that they lose resolution and accuracy at the lower WC ranges due to low light penetration through the watercut medium. Also, because these devices are equipped with very narrow (few mm) slots where infrared light is transmitted, raises the question whether it is representative of the total flow, especially for thick oil applications (Hatimoor, 2013). Lastly, abrasive particles in oil causes wear and scratches on the optical lenses, requiring constant sensor replacements.

2.5.3. Microwave resonance

Different water cut sensors based on microwave resonance technology are commercially available. These sensors typically have a measurement range of 500 ppm to 100 % water and a sensitivity of 50 ppm (Emerson Process Management, 2016). This is accomplished by measuring the permittivity of the oil/water mixture and comparing it to the fundamental permittivity of water and oil that are typically 70 and 2, respectively. The permittivity of a liquid is largely a function of the molecular structure. The oxygen atom of the water molecule has an affinity for the electrons of the hydrogen atoms which results in the electron density on the oxygen atom being greater. This results in the water molecule having a positive and a negatively charged side. Because of this, the water molecules continuously align

with the alternating magnetic field, which slows the propagation of the microwaves significantly. Hydrocarbon molecules, however, do not respond to the changing magnetic field in the same way and therefore have an insignificant effect on the propagation of the microwaves. Karimi (2017) characterised a low cost, completely non-intrusive and full range microwave water-cut sensor based upon a pipe conformable flat T-resonator. Operating within the 90 MHz – 190 MHz band, a resolution of 0.07% at low WC and 0.5% at high WC was achieved. However, because of the non-uniformity of the E-fields generated by the flat resonator (Figure 5a), it was found that the sensor response is not only dependent on the WC but also the orientation of the resonator relative to the oil/water mixture inside the pipe. Karimi (2018) reduced the sensitivity to orientation with the implementation of a pipe conformable helical shaped design. As seen in Figure 5b, the helical design improves the E-field distribution inside the pipe, resulting in 6 times reduced sensitivity to orientation. In conclusive flow loop tests, an accuracy of 1% - 2% was established across the full water cut range. This work has only recently been researched and is not commercially available.

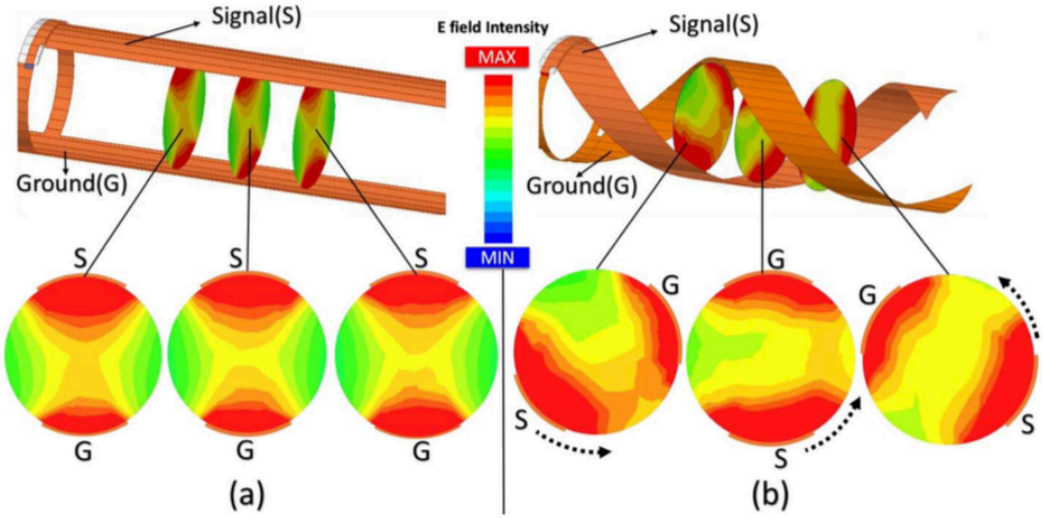

Figure 5: E-field distribution at three different equally spaced cross-sections of the pipe. (a) Flat design. (b) Helical design. (Karimi, 2018)

2.5.4. THz Time-Domain Spectroscopy

Terahertz (THz) spectroscopy is a developing spectral technique bridging the gap between microwave and infrared spectroscopy and is becoming a hot research topic (Song et al, 2016). It has been shown that molecular torsions or vibrations, as well as intramolecular or intermolecular hydrogen bonding in part intrinsically correspond to THz frequencies (Song et al, 2017; Zhan et al, 2015). Differences in molecular configuration and the polarity of oil, water, and gas allows THz time-domain spectroscopy (THz-TDS) to distinguish between the mediums. A pulsed laser is used in the terahertz pulse generation process. With non-linear crystals as a source, high-intensity ultra-short pulses are used to produce THz radiation from the crystal. A single terahertz pulse can contain frequencies from 0.05 to 4 THz. Using an air plasma, the contained frequency components may be as high as 40 THz. After the THz pulse is generated, the pulse is directed by optical techniques through an oil/water sample and then measured. Because of the different absorption properties of oil, water, and gas in the THz range, their respective distributions in crude oil can be determined qualitatively and quantitatively (Song, 2016). This method has been used to measure the water content of crude oil with low water content ranging from 0.01% to 25.00% (Jin et al, 2013). However, this method is less suited for high-water-content-oils due to the strong absorption of the THz pulse in water.

2.5.5. X-Ray transmission

Another typical method for measuring phase fraction is to transmit gamma rays through the product mixture to obtain and then analyse their energy attenuation (Warren et al, 2003). As radioactive materials are required to produce gamma rays, gaining regulatory permits for this sensor type as well as the handling and later disposal of the radioactive materials is problematic. The use of X-rays for phase fraction measurement presents similar complications including health risks (Luggar et al, 1999).

2.5.6. Speed of Sound (SoS)

A WC sensor developed by Saudi Aramco (Xiao, 2015) is based upon the difference in densities of oil and water which affects the acoustic speeds of sound travelling through it. This method is not radioactive and possesses the added advantages of being nonintrusive to allow full bore access and works for the full 0% - 100% WC range. The water cut can only be calculated from the SoS measurements once the density and adiabatic compressibility of the mixture constituents are determined by lab measurement. The error in water volume fraction between the model and the flow loop reference measurement was within 5% in absolute difference, exceeding the accuracy required for production and reservoir management uses (Xiao, 2015; Meng et al, 2006).

2.6. Theoretical Viscosity Prediction

A vast amount of published literature exists on the rheology of solids-in-liquid suspensions, namely Einstein (1977, 1911), Krieger (1972), Jeffery and Acrivos (1976), Batchelor (1977), Russel (1980), van der Werff (1989), Rodriquez (1992), Larson (1999). However, emulsions consisting of two immiscible liquids have received less attention. Pal (2001) states that the understanding of the rheological behaviour of emulsions is important in many industrial applications. Furthermore, for the proper handling, storage and pipeline transfer of emulsions, knowledge of the rheological properties of the emulsion is required. This is crucial for the design, selection and operation of the equipment involved. The viscosity of an emulsion depends on the initial viscosity of the bulk phase (continuous phase), η_c and the volume fraction of the drops φ. Starting at 0WC with oil as the continuous phase, the viscosity increases with an increase in WC. This is true up until around 80%, where inversion occurs. When an inversion occurs the oil becomes the dispersed phase and the water the continuous phase, causing a rapid decrease in effective viscosity (Figure 6).

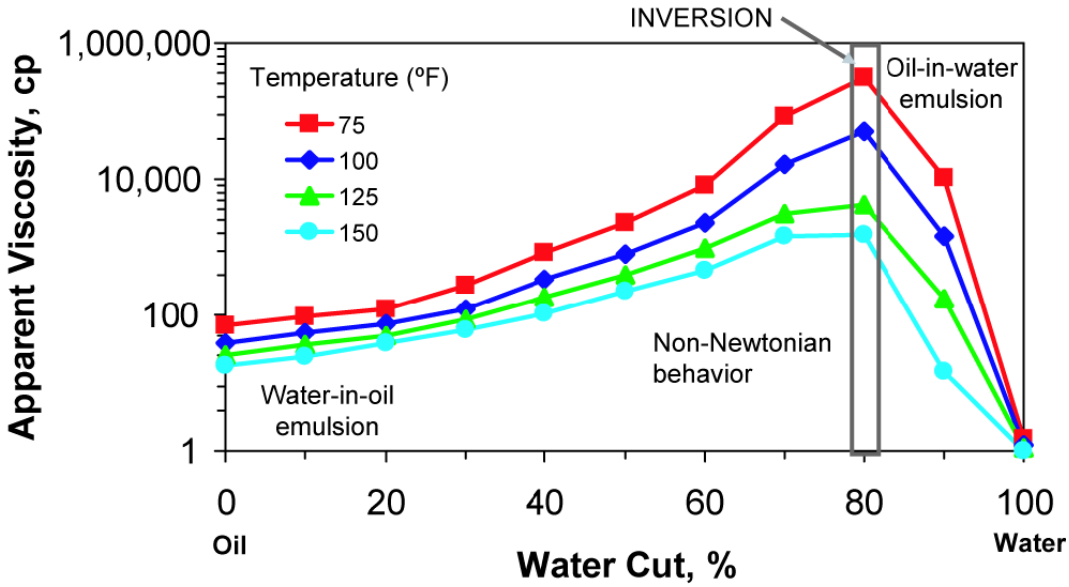

Figure 6: Viscosities of very tight emulsions at a shear rate of 0.1 (1/s). (PetroWiki, 2018)

In cases where the emulsion droplets are nearly spherical and under creeping flow conditions (particle Reynolds number → 0), the relative viscosity (η_r) of emulsions of non-colloidal droplets can be written as (Pal, 1987)

$$\eta_r = f(K, \varphi). \tag{2.1}$$

Where η_r is defined as the ratio of emulsion viscosity to continuous-phase viscosity (η_c), and K is the ratio of dispersed-phase viscosity (η_d) to continuous-phase viscosity. For dilute emulsions where the interaction between droplets is absent, The Einstein model is one of the earliest models and is standard for solid particles as the suspended medium. This is given by the Einstein equation

$$\eta = \eta_0(1 + 2.5\varphi). \tag{2.2}$$

For emulsions, this is problematic when k, which is the ratio of the viscosity of the drops to that of the bulk phase, η_{drop}/η_0 is a very high value. For lower values of k where the dispersed phase is assumed to be very small spherical droplets, the Taylor equation is used:

$$\eta = \eta_0(1 + \varphi(5k + 2)/(2(k + 1))). \tag{2.3}$$

Another popular formula is the Dougherty-Krieger formula:

$$\eta = \eta_0(1 - \varphi/\varphi_c)^{-2.5\varphi_c}. \tag{2.4}$$

It incorporates a "close packing" fraction φ_c at which the viscosity becomes infinite. This technique is less suited for emulsions than solutions with solids. At $\varphi = 0.64$ the viscosity rises exceptionally, thereby limiting the range of this formula. Another approach, better suited for emulsions, is the Yaron & Gal-Or model:

$$\eta = \eta_0(1 + 5.5\varphi A/B) \tag{2.5}$$

Where

$$A = \left[4\lambda^7 + 10 - \left(\frac{84}{11}\right)\lambda^2 + \left(\frac{4}{k}\right)(1 - \lambda^7)\right] \tag{2.6}$$

$$B = \left(1 + 5.5\varphi A/\left(10(1 - \lambda^{10}) - 25\lambda^3(1 - \lambda^4) + \left(\frac{10}{k}\right)(1 - \lambda^3)\right)(1 - \lambda^7)\right) \tag{2.7}$$

$$\lambda = \varphi^{0.333} \tag{2.8}$$

Lastly, another choice based on extensive evaluation of real emulsion viscosities with broad ranges of k is from Pal [2001]:

$$\eta = \eta_0\eta_r \tag{2.9}$$

where η_r is given by:

$$\eta_r[(2\eta_r + 5k)/(2 + 5k)]^{1.5} = (1 - \varphi/\varphi_m)^{-2.5\varphi_m} \tag{2.10}$$

and $\varphi_m = 0.637$.

2.7. Literature Conclusion

Reflecting on the literature presented in this section, various conclusions are made regarding the starting point for this study. Magnetoelastic sensors have been used for various sensing applications. As previously described, a magnetic response can be excited from an amorphous ribbon with a time-varying magnetic field. The flux changes around the ribbon are detected either with a secondary coil, a microphone or optical sensor. In the case of a secondary coil, a voltage-time signal recorded.

The voltage signal is largest where the excitation frequency matches the mechanical resonant frequency of the ribbon. Furthermore, the mechanical resonant frequency is dependent on the effective damping on the ribbon induced by the surrounding medium, which enables the characterisation of the sensor response relative to the viscosity/density product of the surrounding medium.

Various commercially available sensors have been presented along with their performance, advantages and known disadvantages. Commercial sensors listed in Table 1 achieve full range WC detection with an uncertainty of 1% in most cases. These sensors are, however, very expensive. A magnetoelastic resonance sensor capable of water content characterisation may fill a market gap for cost-effective WC sensors.

Lastly, various viscosity prediction models were presented. All presented models will be used to derive a theoretical viscosity value. This, along with the theoretical density value is implemented into Equation 1.1 to determine a theoretical frequency shift. Although the results of this will not be used to characterise the sensor, it will be used to validate the sensor sensitivity to water content ranging from 0%WC to 100%WC.

3. Sensor Characterization and Concept Validation

This section includes the methodology for the validation of the concept. This includes a description of all the components and techniques that were used in this process. The experimental results from all tests conducted are included and discussed.

3.1. Overview

The proposed sensor consists of an amorphous ribbon and a biasing ribbon enclosed in a polyethylene housing. The housing contains an internal volume wherein the liquid medium is injected and brought into contact with the amorphous ribbon. The biasing ribbon is mounted in close proximity to the amorphous ribbon as to sufficiently bias the amorphous ribbon, allowing the excitation of a response signal. An acousto-magnetic (AM) anti-theft tag is used as the sensor as it consists of the same materials. A signal is excited by means of an excitation coil that creates an excitation field H_{EX}. The excitation field consists of a time-varying component and in cases where the bias ribbon is not used, also a DC component. The sensor response (flux changes around amorphous ribbon dependent on the composition of the liquid inside the sensor housing) is detected with a secondary coil (pickup coil) by means of magnetic induction. Two methods of determining the resonant frequency of the sensor are explored. An impedance analyser is used to measure the impedance of the pickup coil with the sensor located inside the coil. The impedance is measured across a specific frequency band. At resonance, the permeability of the amorphous ribbon is at the maximum, resulting in the maximum inductance of the pickup coil. The peak impedance described by $Z = R + j\omega L$ is measured at the corresponding resonant frequency. Another method measures the voltage signal induced in the pickup coil and performs a Fast Fourier Transform (FFT). This gives the maximum signal strength at a corresponding resonant frequency. Both methods are used in the design, realization and evaluation of the sensor technology.

3.2. Acousto-Magnetic Tag

This section includes the description, design and composition of the anti-theft tags (Sensormatic Ultrastrip® ZLAPS2) that were used in this study. These tags are readily available and used by multiple retail stores to safeguard against the theft of ehigh-priced products. Acousto-magnetic pillars are installed at the shop entrance that detects when a magnetised tag passes through the door by "listening" for a return signal excited in the tag. The security pillars emit a signal pulse. When magnetised, the amorphous ribbon inside the tag resonates when excited by the signal pulse. Sensors in the security pillars detect the resonant frequency and set off the alarm.

This particular tag was chosen for this study because:

- It contains an amorphous ribbon with a predefined resonant frequency and dimensions.
- It contains a biasing strip, which removes the need for large dc biasing fields.
- It consists of a polyethylene housing, making it easy to inject a medium into while allowing full contact with the resonating ribbon.

3.2.1. Dimensions and Layout

The AM tag consists of a polystyrene/polyethylene housing that contains a semi-hard magnetic biasing strip and a magnetoelastic resonator strip. The contents of the housing are sealed with a polyethylene/polyester laminate. Figure 7 shows the major dimensions of the tag.

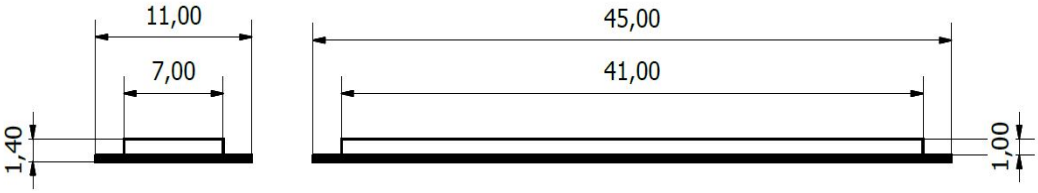

Figure 7: The major dimensions of the acousto-magnetic tag.

A sectional view of the tag can be seen in Figure 8. The housing that encapsulates the metallic strips consists of a polystyrene/polyethylene polymer with a thickness

of 300 µm. The magnetic ribbon (resonator) is made from a 28 µm thick amorphous alloy ribbon. The semi-hard magnetic biasing ribbon made from an iron-nickel (FeNi) alloy (Sensormatic, 2018). The biasing strip is laminated into a 120 µm low density polyethylene/polyester sheet that seals the contents of the tag.

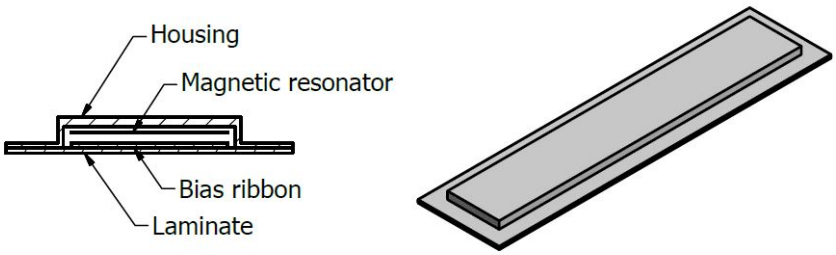

Figure 8: (a) Sectional view of the acousto-magnetic tag, (b) a three-dimensional view of the acousto-magnetic tag.

3.2.2. Magnetic Characteristics

Knowledge of the magnetic characteristics of the amorphous alloy is required for the design and theoretical modelling of the sensor. Tests were performed using a Vibrating Sample Magnetometer (VSM) (3900 Series MicroMag™, PMC) to determine the relevant magnetic properties of the amorphous alloy and the semi-hard magnetic biasing strip. Figure 9 shows the convention of the axes that will be used during the rest of this discussion.

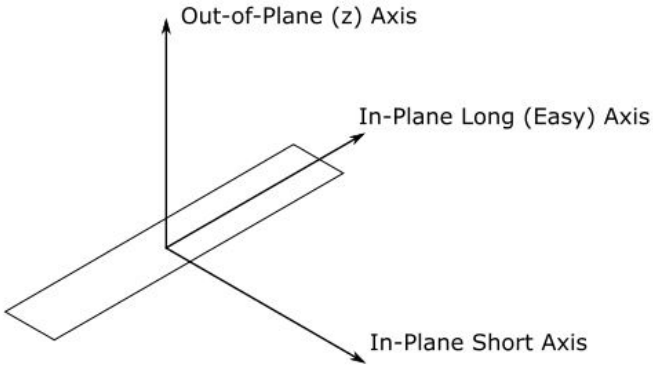

Figure 9: Illustration showing the convention for magnetic axes as they will be referred to in this paper.

From the results of the VSM measurements, accurate representations of the magnetization curves (typically called B-H curves) were created. This was done for the amorphous alloy in the easy axis, short axis and the out-of-plane z-axis. The semi-hard magnetic biasing strip was characterised in the magnetizing axis (Long axis). Figure 10 the amorphous alloy magnetization curve with the applied field in Oersted (Oe) on the x-axis and the measured magnetization in *emu* (Electro Magnetic Unit) on the y-axis.

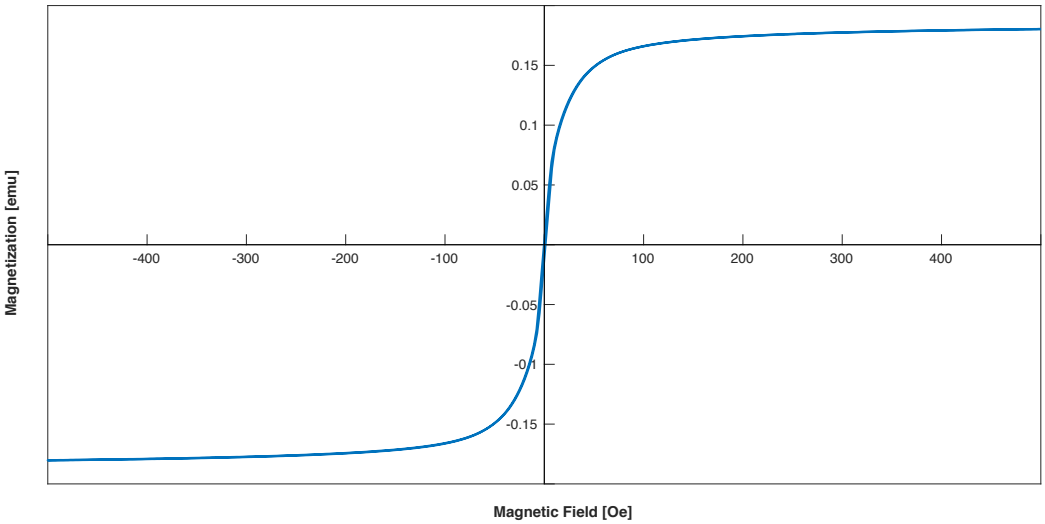

Figure 10: Magnetization curve for amorphous alloy ribbon along the easy axis.

The saturation along the easy axis is the largest compared to that of the in-plane short axis and out-of-plane axis at 151 memu and 15 memu, respectively (Find B-H curves attached in Appendix B). Furthermore, reaching the saturation points require a far greater coercive field of at least ten times that required along the easy axis. Magnetization in all three axes shows no hysteresis, which is to be expected since this alloy is magnetoelastic. The ribbon is characterised by very soft magnetic properties with a coercive field of 56.5 A/m, a remanence of 7 memu (50 kA/m), which in combination with a saturation magnetization of 180 memu (1.29 MA/m) results in a saturation-to-remanence ratio of 26. Compared to the B-H curve for the soft-magnetic biasing strip, shown in Figure 11, hysteresis is visible with a residual field (Mr) of 215 memu (307 kA/m).

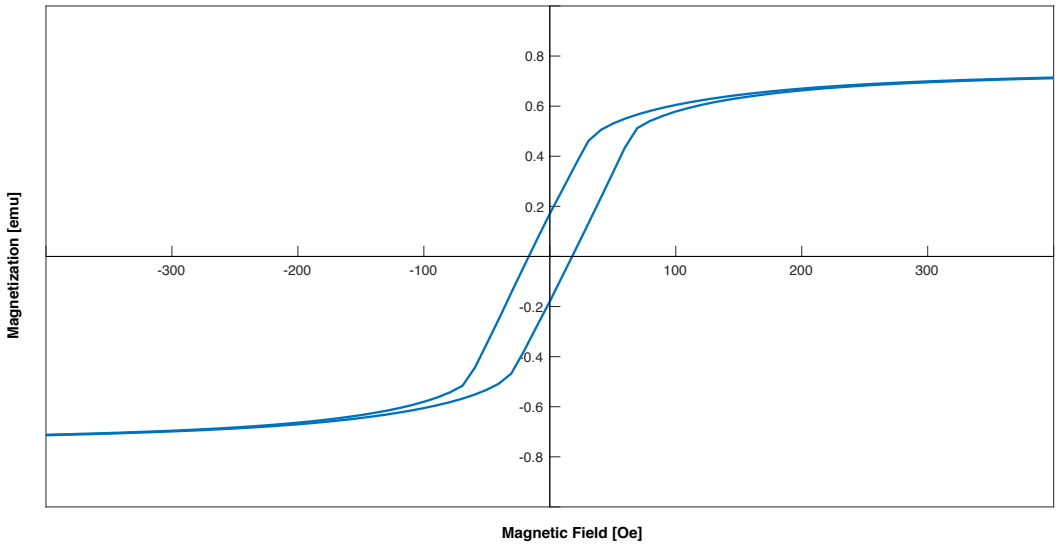

Figure 11: Magnetization curve of the semi-hard magnetic biasing ribbon.

The measurement is normalized to the sample size used in the VSM (4mm x 1mm x 140µm). The true value can be calculated by dividing with the sample volume:

$$M'_R = \frac{M_R}{l \times w \times d} = \frac{0.215(1000)}{(0.005612)} = 38.31 \frac{\text{kA}}{\text{m}} or\ 487.9\ \text{Oe} \qquad (3.1)$$

This indicates the magnetic field present in the biasing ribbon. From the B-H curve of the amorphous alloy, shown in Figure 10, a biasing field of approximately 10 Oe (800 A/m) is required to reach the knee region where the magnetostrictive response is the strongest. This is the required dc bias of the excitation field to obtain comparable measurement results without the use of a biasing magnet. This is recreated later in Section 3.2.3 with the use of a Helmholtz coil. The use of a biasing magnetic means that the applied excitation signal need not possess a DC bias and reduces the power required for excitation. Although the use of a biasing strip introduces significant variation in sensor performance due to variation in magnetization, the reduction in power consumption greatly reduces the design complexity. Furthermore, the convenient packaging of the Acousto-Magnetic tag provides a testing platform that can be used without having to redesign a new package.

3.2.3. Resonator alloy DC bias

Based on results from the VSM measurement for the amorphous alloy, presented in Figure 10, the required DC bias to allow excitation is 800 A/m. A Helmholtz coil (Schwarzbeck Mess-Elektronik, HHS 5201-98) is used to create a homogeneous magnetic field around the ribbon. A time-varying signal with $V_{AC\ peak-peak} = 100$ mV at 58 kHz is generated using a signal generator (Agilent Waveform Generator, 33220A). The signal passes through an amplifier (NF Bipolar Amplifier, HAS 4012) with a gain of 50. The amplified signal is fed to the Helmholtz coil pair where a homogeneous field is created around the ribbon. The ribbon is enclosed in a 350-turn secondary coil and connected to an oscilloscope. The placement of the secondary coil is shown below in Figure 12.

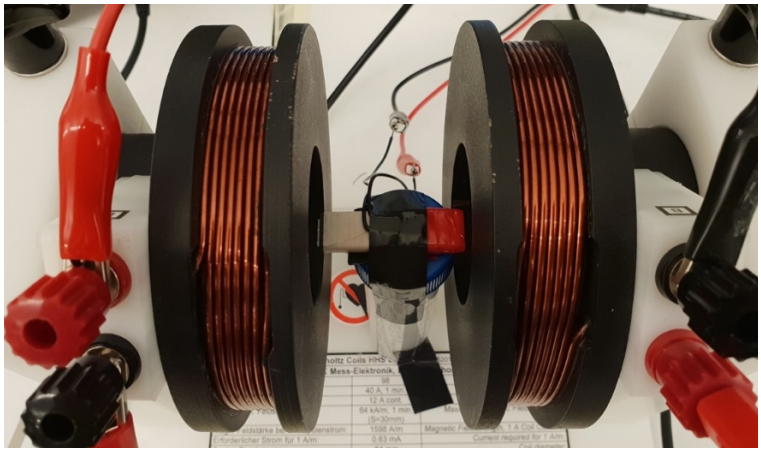

Figure 12: A Helmholtz coil creating a homogenuos magnetic field which magnetises the amorphous ribbon. The resonant peak is largest where the ribbon is optimally biased.

The excitation field H_{EX} contains a DC and AC component, namely H_{DC} and H_{AC}. Whilst the AC component is kept constant at 58 kHz, the DC component is increased from 0.0 mV – 20 mV. The current through the coil is used to calculate the resulting magnetic field strength using the Helmholtz coil formula:

$$B = \left(\frac{4}{5}\right)^{\frac{3}{2}} \frac{\mu_0 nI}{R}. \tag{3.2}$$

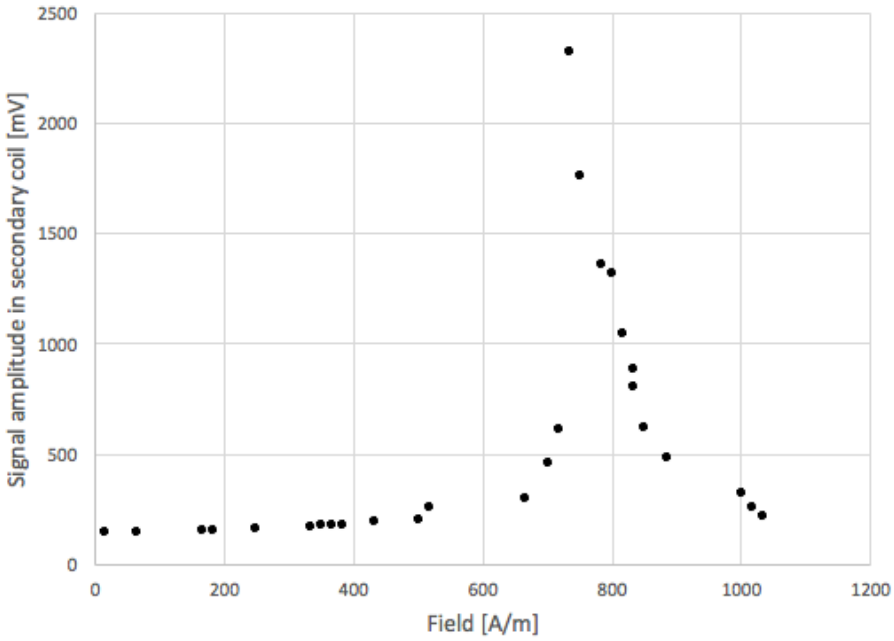

Figure 13: Measured ribbon response to bias field.

The maximum amplitude is measured around 730 A/m as shown in Figure 13. This is close to the hypothesized value of 800 A/m. This test was conducted with the ribbon in air.

3.3. Sensor Susceptibility Considerations

This sensitivity of the sensor is primarily due to the vibrational amplitude being small and the corresponding resonant frequency being high. This translates into a small maximum system damping that results in an immeasurable response. This is favorable in applications where the detection of small variable changes in well isolated systems is required. In a system where there are various sources of noise that may inhibit the characteristic behavior of the sensor, however, this sensitivity may introduce complications. To ensure the system is sufficiently isolated from all sources of noise, these sources must be correctly quantified and considered in the

design. In this section, all sources of noise are described and their influence within the sensor environment predicted.

3.3.1. Temperature

Temperature variations within the sensor environment is considered a source of measurement uncertainty that must be accounted for. The Curie temperature (temperature at which magnetic properties are changed or lost) for this material is around 225 °C. Drilling temperature in High-Pressure and Temperature (HPHT) wells can reach up to 200 °C (DEA, 2018). A change in temperature of the amorphous material will affect Young's modulus of the material. This influences the sensor response, as shown in Figure 14.

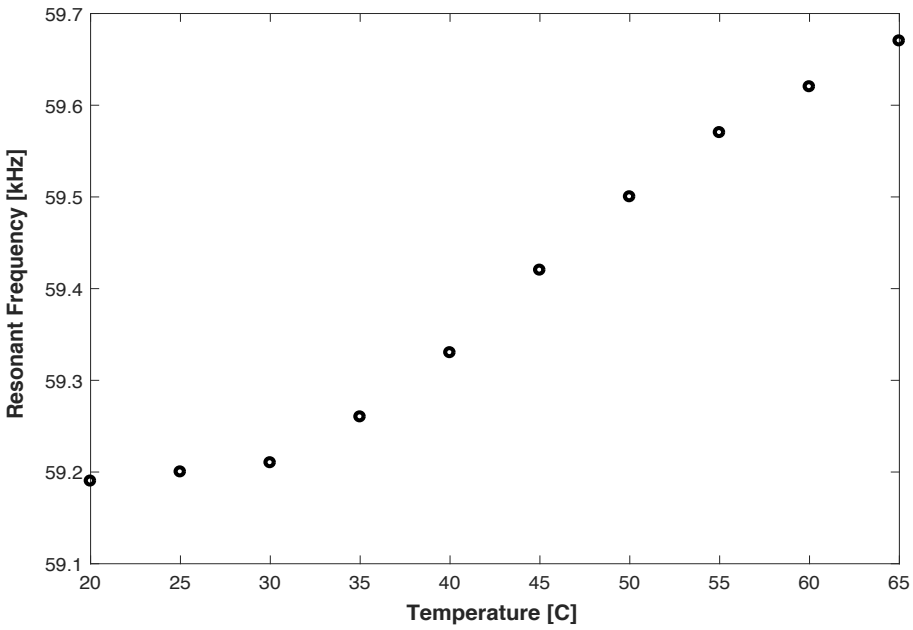

Figure 14: Resonant frequencies of amorphous ribbon measured at different temperatures with a constant magnetic field at 320 A/m.

Furthermore, the influence of temperature variations has a significant effect on the viscosity and density of liquids surrounding the sensor. Various mathematical models exist that predict the temperature-dependence of shear viscosity of a liquid. For a practical example, cooking oil viscosity is reduced when it is heated. Due to

this phenomenon, the temperature of all liquids tested in this project will be controlled.

3.3.2. Pressure

Drilling pressure in High-Pressure and Temperature (HPHT) wells can reach up to 1000 bar (DEA, 2018). Magnetoelastic sensors have been used to measure pressure changes through an out of plane configuration (Grimes, 1999). When the sensor was orientated such that no out of plane vibrations were generated, only longitudinal vibrations, the sensor demonstrated no pressure sensitivity. This has been experimentally validated with a pressure vessel (Digiquartz Portable Standard, M765). The sensor is placed inside a 350-turn coil and together placed inside the pressure vessel. The pressure is increased from 100 kPa – 17 000 kPa in increments of 700 kPa and the resonant frequency measured with an Impedance Analyser (Agilent 4294A). The resonant frequency is initially measured at 58.84 kHz and remains unchanged up to 17 MPa. This pressure corresponds to pressures found at 11.5 km below sea-level in saltwater. The effects of pressure variations will therefore not be considered in the design phase.

3.3.3. Uniform distribution across surface area

The vibration of the resonator during exposure to a magnetic field is primarily dependent on the damping force exerted by the surrounding medium on the resonator surface area. The uniform distribution of the medium around the resonator is required to ensure an accurate correlation between vibration and medium characteristics. The small volume present within the AM tag may present difficulties in ensuring this because of liquid surface tension at a small scale. Figure 15 below shows various distributions of the liquid medium inside the sensor. Uniform liquid distribution across the resonator surface area is assumed.

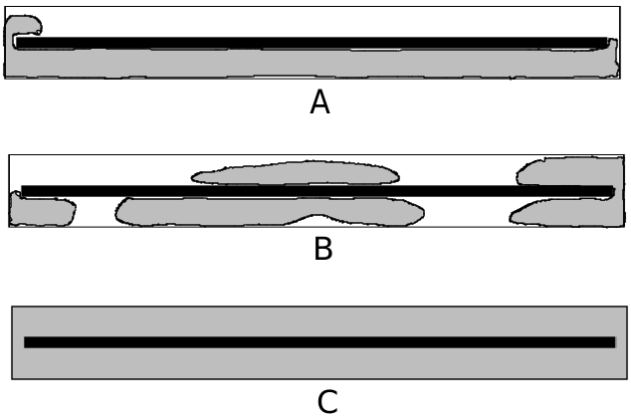

Figure 15: Sensor body showing the medium distribution (A) under the resonator, (B) unevenly spattered throughout the sensor volume and (C) uniformly distributed across the resonator surface area.

3.3.4. Decay of material magnetic properties

The decay of the magnetic properties of the amorphous alloy has been observed due to corrosion of the metal. This decay result in reduced sensor vibration and shift in mechanical resonant frequency. This is considered a source of signal variation in cases where measurements are made and compared to previous measurements with the same resonator. Here, corrosion of the amorphous alloy and its magnetic characteristics is a major concern and must be addressed.

3.3.5. External magnetic noise

Various sources that emit electromagnetic waves exist in the real world. These sources may induce measurement noise if the wave frequencies are within the same bandwidth as the measured signal. Three major sources of potential noise are discussed. The excitation coil itself possesses a resonant frequency. If this resonant frequency is within the same bandwidth as the signal measured from the resonator, it could possibly add or subtract from the measured amplitude at that specific frequency. The excitation coil must undergo testing to ensure that there will be no signal interference. The second source of possible noise is the earth's magnetic field, a static field measured at around 30 A/m. Since a large signal response at high frequencies is expected, no design considerations will be made to remove this

interference. Lastly, the third source of electromagnetic interference is that which is emitted by the mains at 50 Hz. Since the operating frequency band is in the kilohertz range, this will not influence the sensor measurements.

3.3.6. Amplifier Variables

When measuring the flux changes around the resonator, it is imperative that the power from the amplifier driving the excitation field remains the same. The behavior of some electrical components like transistors and inductors are dependent on the frequency and temperature at which they operated at. Design consideration must be made to ensure sufficient cooling and operation within the design specifications of the electrical components.

3.3.7. Inconsistencies in sampling

Digital sampling will be used to characterise the resonator response. To ensure that the signal is correctly sampled, and aliasing does not occur, the Nyquist theorem must be satisfied.

3.4. Relevant signal landmarks

For this project, the only relevant signal landmark that will be recorded is the amplitude and frequency of the resonant peak (Shown in Figure 16). A shift in frequency and amplitude will be correlated with a change in liquid medium viscosity and density product, and subsequently the WC ratio.

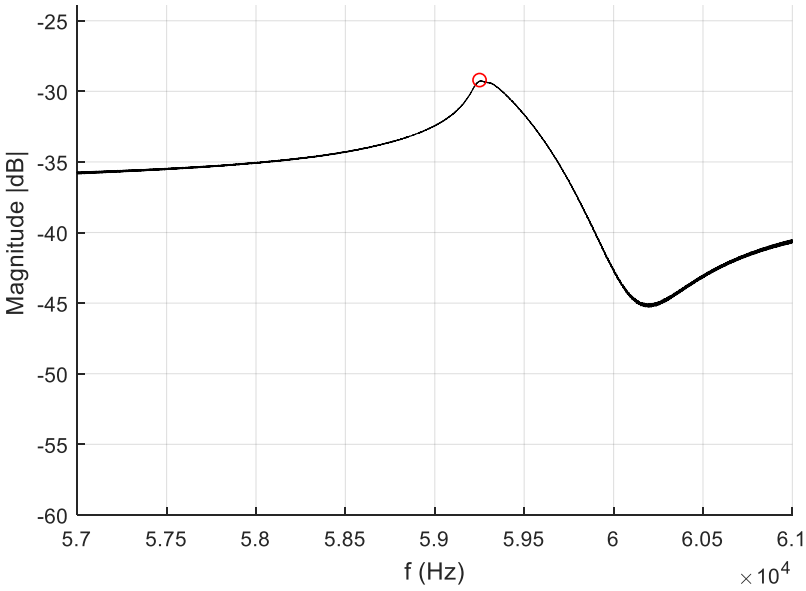

Figure 16: Characteristic ribbon signal showing the resonance peak.

3.5. Viscoelastic Response

Tests were conducted to validate the proof of concept, namely, that the resonant frequency and amplitude of the resonator will decrease when subjected to a viscous medium with a higher viscosity.

3.5.1. Experimental Procedure

The viscosity of glycerin and water mixtures is well documented (Dorsey, 1940). Glycerin/water mixtures were created ranging from 0% - 100% volumetric Glyc/Wt. with 10% increments. Pure glycerin was combined with distilled water at 20 ºC. Because of signal variability in the sensors induced by a difference in magnetization in the biasing ribbon, a single sensor was used to measure the frequency response to the glycerin/water mixtures. Figure 17 below shows the step-wise procedure followed during the measurement process. Steps 2 – 4 were repeated sequentially for every mixture.

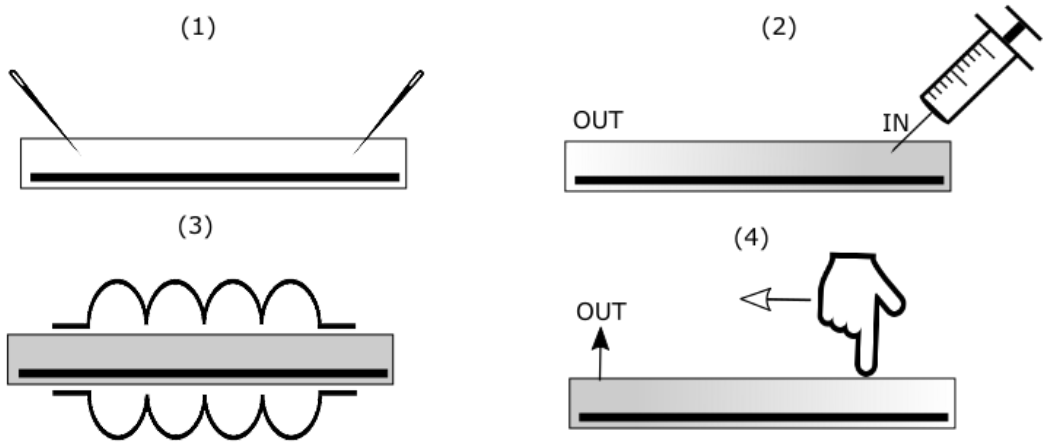

Figure 17: The stepwise procedure for measuring the resonant frequency and impedance response of the sensor. (1) Two holes are pierced through the polyethylene laminate. (2) The internal volume is filled with the viscous medium via injection with a needle and syringe. The resonator is completely submerged in the medium. (3) The sensor is placed inside the pickup coil and a measurement taken. (4) Pressure is applied to the laminate and forces the fluid inside the sensor out through a drainage hole.

A Helmholtz coil is used to excite a response from the sensor. A signal generator produces a time-varying signal with 100 mV peak-peak swing. No dc bias was added to the signal. The signal is amplified by an amplifier (NF Bipolar Amplifier, HAS 4012) with a gain of 50.

3.5.2. Results and discussion

The viscosity and density of the glycerin/water mixtures were used in Equation 1.1 to determine the theoretical frequency shifts. The theoretical values, along with the experimental values are shown in Figure 18 and Figure 20.

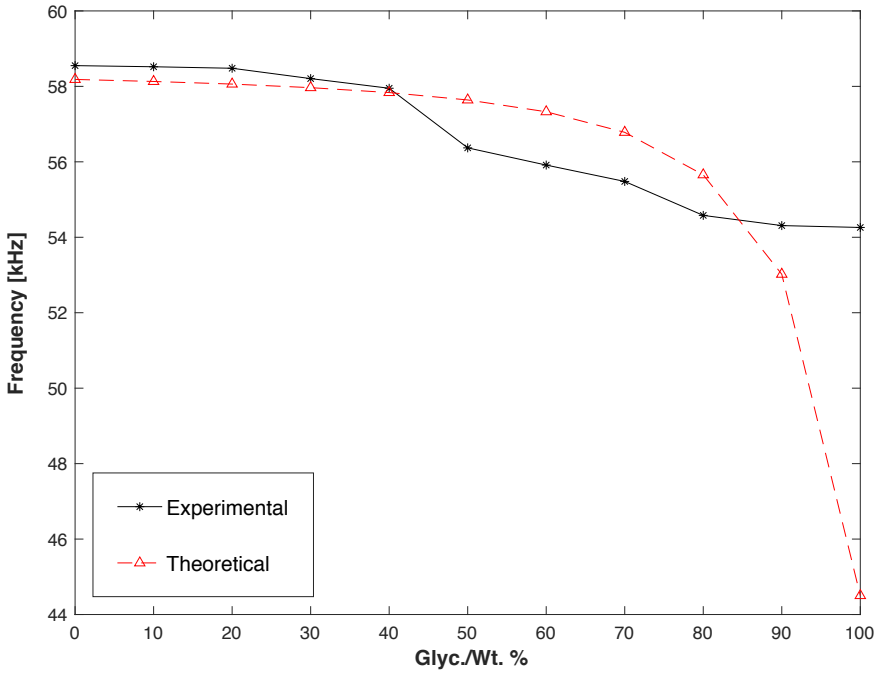

Figure 18: Experimental and theoretical resonant frequencies measured for various Glycerin/Water ratio solutions.

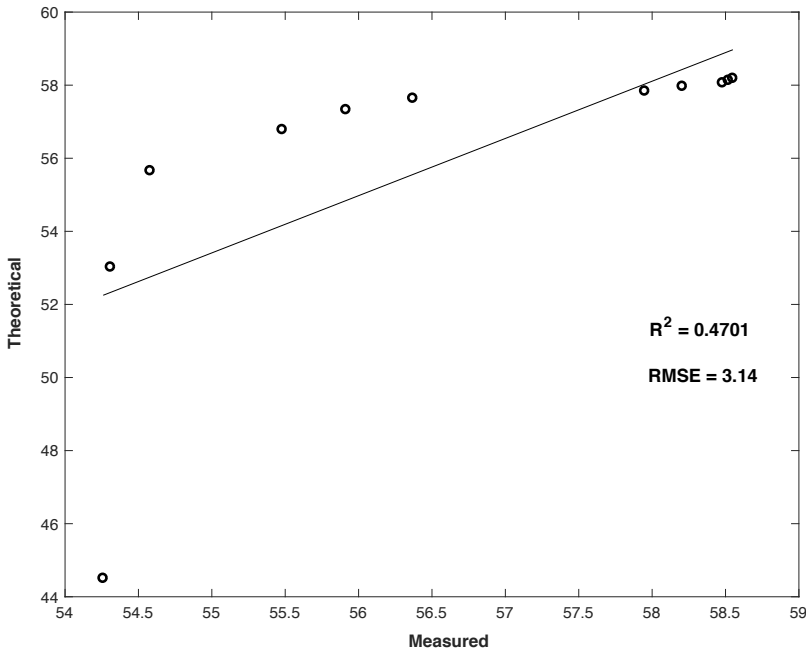

Figure 19: Correlation between theoretical and measured data.

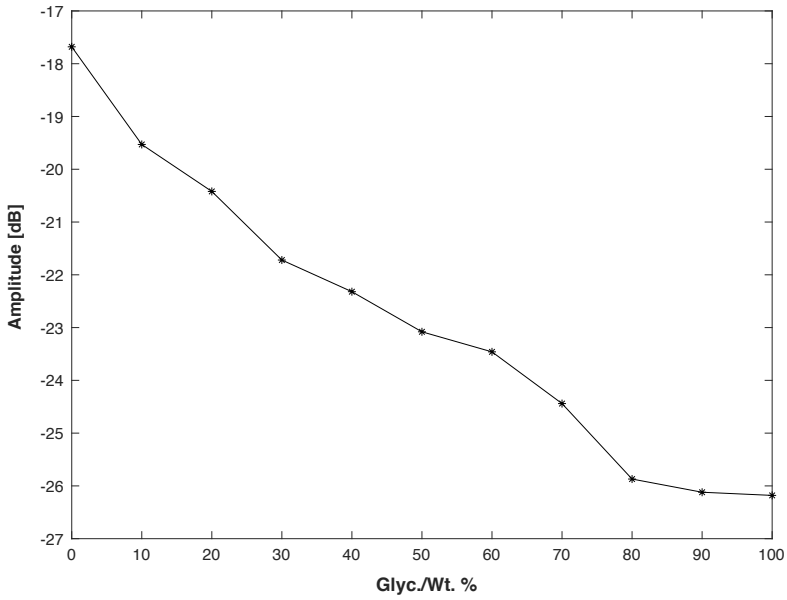

Figure 20: Measured amplitude at the resonant peak.

These results prove that there is a measurable frequency and amplitude shift for resonator immersion in a liquid medium with a dynamic viscosity ranging from 1.005 [g/cm·s] to 1410 [g/cm·s]. A frequency shift of 3.8 kHz was observed from 0% Glyc/Wt. at around 58.5 kHz to 100% Glyc/Wt. at around 54.7 kHz. However, the linear regression model in Figure 19 only accounts for 47 % of the variability around the mean. The theoretical model overshoots the influence of the medium on the resonance of the ribbon by almost 10 kHz at 100% glycerin. Furthermore, a reduction in vibrational amplitudes of 8 dB was measured. These results show the sensor is capable and possesses sufficient sensitivity to be used as a viscosity sensor, although better models that describe the sensor behavior must be developed.

Further experiments were conducted to determine inter- and intra-sensor repeatability. Intra-sensor repeatability was achieved with changes in measured signal frequency being only 19 Hz. Inter-sensor tests revealed significant variations in signal amplitudes and behavior, with an average variation of 300 Hz. The results from these tests are shown in Appendix B. This means that although these sensors are mass produced, sensor-specific characteristics prevent repetitive tests using the same sensor. The largest source of variation in the sensor responses is the difference

in magnetization of the soft-magnetic biasing ribbon. Measurements using a VSM and five samples from different sensors confirmed that all sensors are magnetized differently. This makes sense, because in the retail industry where these sensors are used they must be easily de-magnetised so that they can be deactivated after the customer makes a purchase. Using a biasing magnet does introduce significant sensor variability, but considerably reduces the amount of power required to excite a measurable signal response from the sensor.

3.6. Water Cut Sensor

After confirming that a resonant frequency and amplitude shift is measured with an alteration in medium viscosity and density using glycerin and water, the second set of experiments attempted to confirm this using a non-homogeneous emulsion of oil and water. Predicting the effective viscosity of a non-homogeneous emulsion, however, is subject to a large research field. The followed approach is described and the relevant results presented and discussed. This is a novel application for magnetoelastic sensor technology.

3.6.1. Experimental Procedure

An Impedance Analyser (Agilent 4294A) was used to characterise the permeability of the vibrating ribbons at resonance as it is directly proportional to the vibrational amplitude of the resonator. The conductive copper coil was connected to the impedance analyser using a 4TP 1M adaptor. The data points were recorded and exported to Excel. The experimental setup is shown in Figure 21.

Since oil and water are non-homogeneous, meaning that they do not mix naturally, particular attention was given to the preparation of the oil-water emulsions. Two different strategies were studied for making the oil-water emulsions. In the first one, the required amount of oil and water were mixed along with 10% surfactant (Tween 20). The mixture was then dispersed by utilizing an Eppendorf shaker at 1500 rpm for 3 hours. When studied under the microscope, large islands of the disperse phase were observed indicating a lesser degree of emulsification (See Figure 22). As

expected, this mixture was unstable and separated into oil and water when left standing for a few minutes. In the second approach, the oil, water and Tween 20 mixture were subjected to agitation at 20 kHz using a probe tip sonicator (Sonics® Vibra-Cell VCX 500) for 3 hours. The dispersed phase in the resultant emulsion was reduced to fine dimensions as shown in Figure 23, resulting in a long-lasting stable emulsion. The emulsion was still stable and showed no signs of separation 5 months after creation. The sensor showed sensitivity to both emulsion mixing strategies. Due to time and hardware constraints, the first method was used to create the oil-water emulsions. This is sufficient as it represents a more natural method of mixing that can be expected in downhole conditions. Emulsions were created and measurements were taken within two minutes of creation to eliminate the effect of separation.

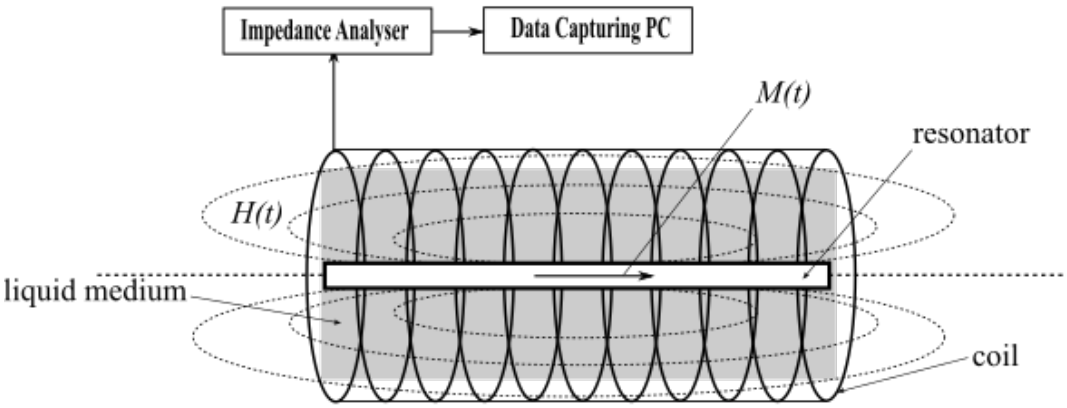

Figure 21: Schematic showing the experimental setup used to measure the resonant frequency of the resonating sensor (resonator).

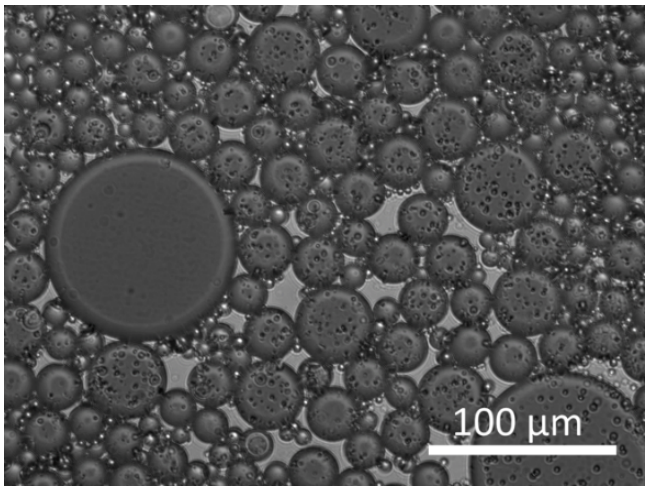

Figure 22: Images of dispersed mixture using Eppendorf Shaker at 1500 rpm.

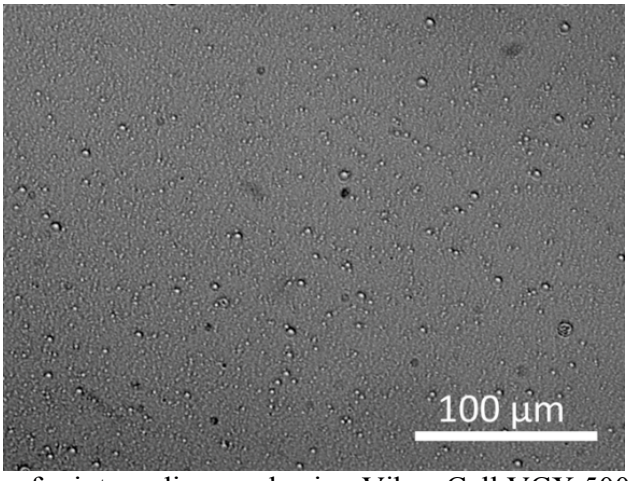

Figure 23: Image of mixture dispersed using Vibra-Cell VCX 500 sonicator.

3.6.2. Theoretical Model Prediction

The effective viscosity of the WC emulsions was estimated using different emulsion viscosity models. It is difficult to accurately predict for an oil/water emulsion, and various theories exist, namely Einstein (Mooney, 1951), Taylor (1932), Pal (1989), Yaron & Gal-Or (1972) and the Dougherty-Krieger model (1972). Due to droplet crowding, emulsions indicate non-Newtonian behavior, which is why their viscosity is higher than the viscosity of oil and water. Einstein (Mooney, 1951) developed a model for prediction of emulsion viscosity that indicates a positive linear relationship between the relative viscosity of emulsion and volume fraction of dispersed phase. Taylor (1932) extended the work of Einstein and considered the

effect of both the continuous and dispersed phase. This model is applicable for emulsions with a low dispersed droplet concentration. Another correlation was proposed by Dougherty and Krieger (1972) that applies to emulsions with a high dispersed phase droplet concentration. A combination of these prediction models is used to validate the experimental data.

3.6.3. Results and discussion

The impedance measured in the interrogation coil is affected by the magnetic susceptibility of the core materials. This includes the magnetic ribbons and the water/oil emulsion. The impedance of the interrogation coil is given as $Z = R + jX_L$ where the reactance $X_L = \omega L$ and the inductance L of the coil can be written as:

$$L = \frac{N^2 \mu(f,\eta) A}{l} \tag{3.3}$$

At this point, the permeability of the core material is influenced by the water/oil liquid volume inside the sensor and the permeability of the sensor itself, as a function of time. The change in core material permeability induced by changing the liquid from pure water to pure crude is significantly smaller than the fluctuations measured in the sensor material and is therefore ignored. For the amorphous alloy used in the sensor, the permeability can be written as a function of frequency and surrounding medium viscosity through magnetostriction. Magnetoelastic vibrations in a magnetoelastic sensor occur when the applied magnetic field is time varying in nature, causing the field-generated strain to vary with time thus producing a longitudinal elastic wave (Mungle, 2008). These vibrations, in turn, generate a secondary magnetic field that can be detected. The measured shift in frequency/amplitude of the sensor material is caused by a change in surrounding material. The resonant frequency of the resonator is determined by the effective damping force induced by the viscosity of the surrounding medium. Resonators in mediums of varying viscosity each possess a significantly different characteristic

frequency response. The impedance of the coil and in-medium resonator was measured for air, water and oil as shown in Figure 24.

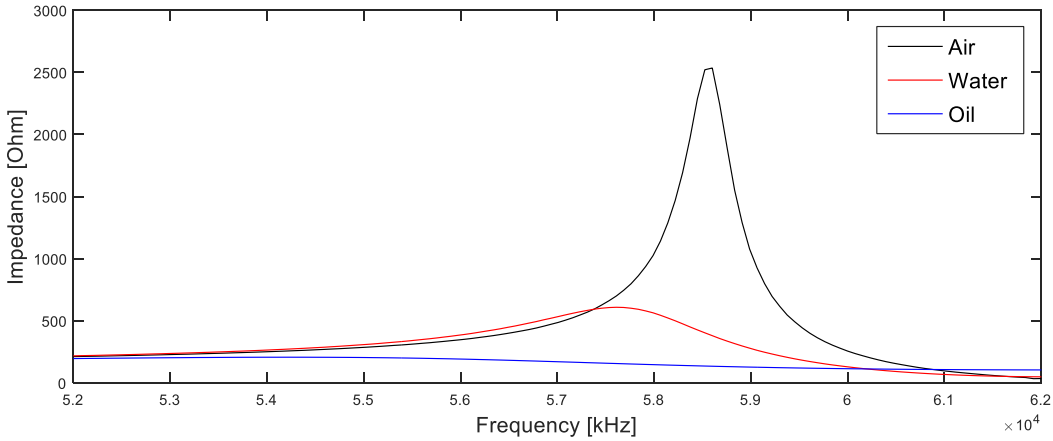

Figure 24: Impedance - frequency curves for the resonator measured in air, water and oil respectively. The peaks are found at 58.6 kHz, 57.6 kHz and 54.2 kHz respectively.

Results show a reduction in resonant frequency and vibration amplitude from exposure in air to water of 0.99 kHz and 1.93 kΩ respectively. Further reductions with exposure in oil were measured at 3.37 kHz and 0.4 kΩ from the measured peaks in water. Measurements were made with an oscillation level of 10mV, which translates to a power consumption of 10nW in air. When immersed in the water/oil emulsion this value ranges from 50 nW to 125 nW.

Further experiments were performed by immersing the resonator in different WC emulsions and measuring the resonant frequency and impedance shift. Different resonators were used with every WC emulsion, thereby ensuring that there are no liquids present of the surface of the resonator before immersing it in the WC emulsion. Each resonator was characterised in air, whereafter the frequency and impedance shifts were normalized to the frequency shift caused by 100% water. The results are presented below in Figure 25 and Figure 26.

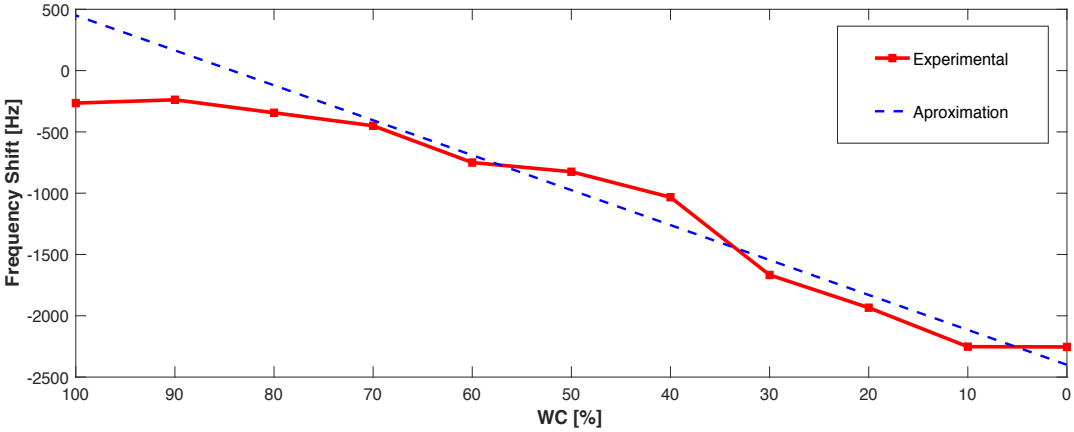

Figure 25: The experimental frequency shift measured with the sensor immersed in different water cut (WC) emulsions.

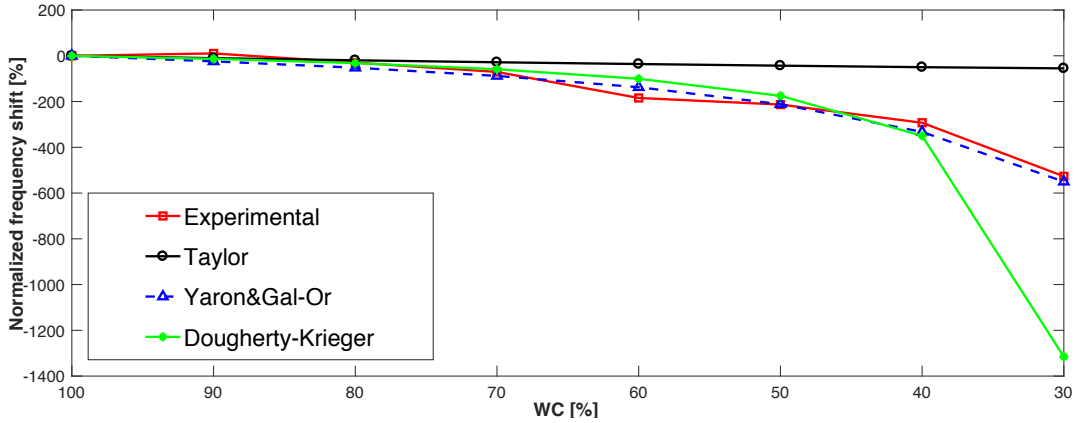

Figure 26: Experimental measurements compared with theoretical predictions of the Taylor, Yaron & Galo-Or and Dougherty-Krieger models from 100% - 30% WC. The frequency shift is normalized to the shift from unloaded to loaded sensor at 100 % WC.

The results presented in Figure 25 show an increase in frequency shift (relative to an undamped sensor) with a decrease in emulsion WC. This is supported by the theoretical predictions made using Equation 1.1 and the considered viscosity models (results shown in Figure 26). Here, however, the frequency shifts are plotted as far as 30% W/C. This is due to phase inversion that occurs at high volume fractions of the dispersed phase. At this point, all practical models lose their validity. At lower volume fractions the dispersed particles are assumed to be near spherical, and the viscosity can be determined as a function of temperature and

volume fraction. At higher volume fractions, however, this can no longer be assumed as the hydrodynamic interaction between the droplets becomes significant and the effective viscosity drastically increases. The experimental results fall between the prediction models that were considered. This indicates the sensor possesses a sensitivity to a reduction or increase of the density/viscosity product. The sensitivity is approximated with a linear function within the 80% – 10% WC range. This range is chosen due to unexpected values measured at 90 %WC. Using the standard linear equation, the sensor response is approximated as:

$$\Delta f = 28.5\emptyset - 2400 \tag{7}$$

Substituting (7) into (1), the viscosity density product can be written as:

$$\sqrt{\eta\rho_l} = \frac{2\pi\rho_s d(28.5\emptyset - 2400)}{\sqrt{\pi f_o}} \tag{8}$$

As shown in Figure 27, this linear model accounts for 90.5 % of the variability from the mean. Regarding the derivation of emulsion viscosity, a method has been described by Herrmann et al. (1999) that separates the density/viscosity product. This is achieved with dual liquid-loaded sensors with different surface roughness. Furthermore, any measured frequency shift smaller than the measured shift for 100%WC is indicative of air/gas surrounding the sensor.

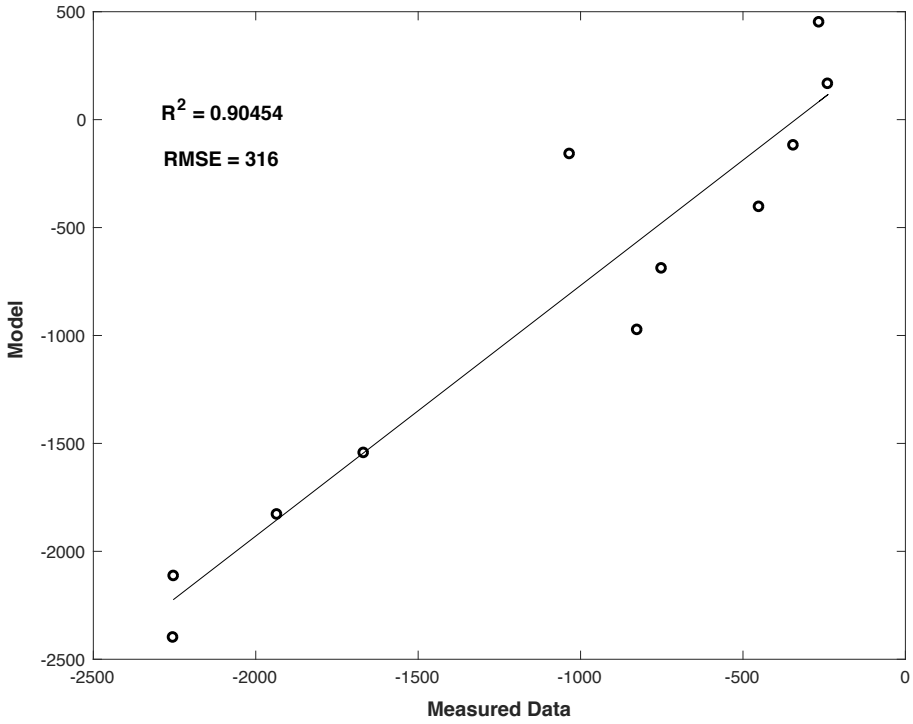

Figure 27: Correlation between fitted model and measured data.

4. Portable Read-Out Device

This chapter describes the physical and electronic design of the Portable Read-out Device (PRD) developed to excite and detect a sensor response in-field. This includes the required hardware, control and power circuits and the software implemented on a microcontroller.

4.1. Microcontroller Selection

Various microcontrollers were considered for the design phase in this project. Key considerations include the clock speed, analog-to-digital converter speed, resolution, Bluetooth connectivity, accessory compatibility, user interface and availability. An assessment is performed based on these factors as shown below in Table 2.

Table 2: Qualitative analysis of various microcontrollers.

Board	Clock	ADC Resolution	Cost (R)	Bluetooth	Memory	IO Pins	Voltage
Adafruit Feather RF53	64 MHz	12-bit	325	Onboard	512 KB	39	3.3 V
Arduino Due	84 MHz	12-bit	448	External	512 KB	56	5 V
Beagle Bone Black	1 GHz	12-bit	715	Onboard	512 MB	92	5 V
Arduino Uno	16 MHz	10-bit	124	External	32 KB	20	5 V
Raspberry Pi 3	1.2 GHz	NA	890	Onboard	1 GB	42	5 V

The PRD is realized through the use of a microcontroller. The ADC (Analog-Digital Converter) is used to sample the measured signal at above $2fe$. A higher ADC speed and resolution translates to higher measurement accuracy. The PRD will interface with a smartphone via Bluetooth connection, requiring the microcontroller to have onboard or external Bluetooth capability. The sampled data will be

transmitted to the smartphone in real time, obviating the need for high memory capacity. Lastly, the use of a low power microcontroller in the PRD will result in longer battery life and use.

The Arduino Due possesses 12-bit ADC resolution and an 84 MHz master clock speed. It allows configuration of the multi-channel ADC which enables fast ADC conversion rates up to 1MHz. The Arduino is a microcontroller motherboard that allows one program to run at any given time, as opposed to the Raspberry Pi which is a general-purpose computer that can run multiple programs simultaneously. This is not suited for the PRD as it adds increased complexity which takes from the robustness of the system. Furthermore, the Due allows integration with an external Bluetooth module and requires 5V power supplied by an input pin. This allows a portable battery powered power supply. Lastly, the Arduino Developer Environment is widely used and support is available. For these reasons, the Arduino Due was chosen.

4.2. Electronic Design

Figure 28 below shows the electrical connection diagram for the Portable Read-Out Device.

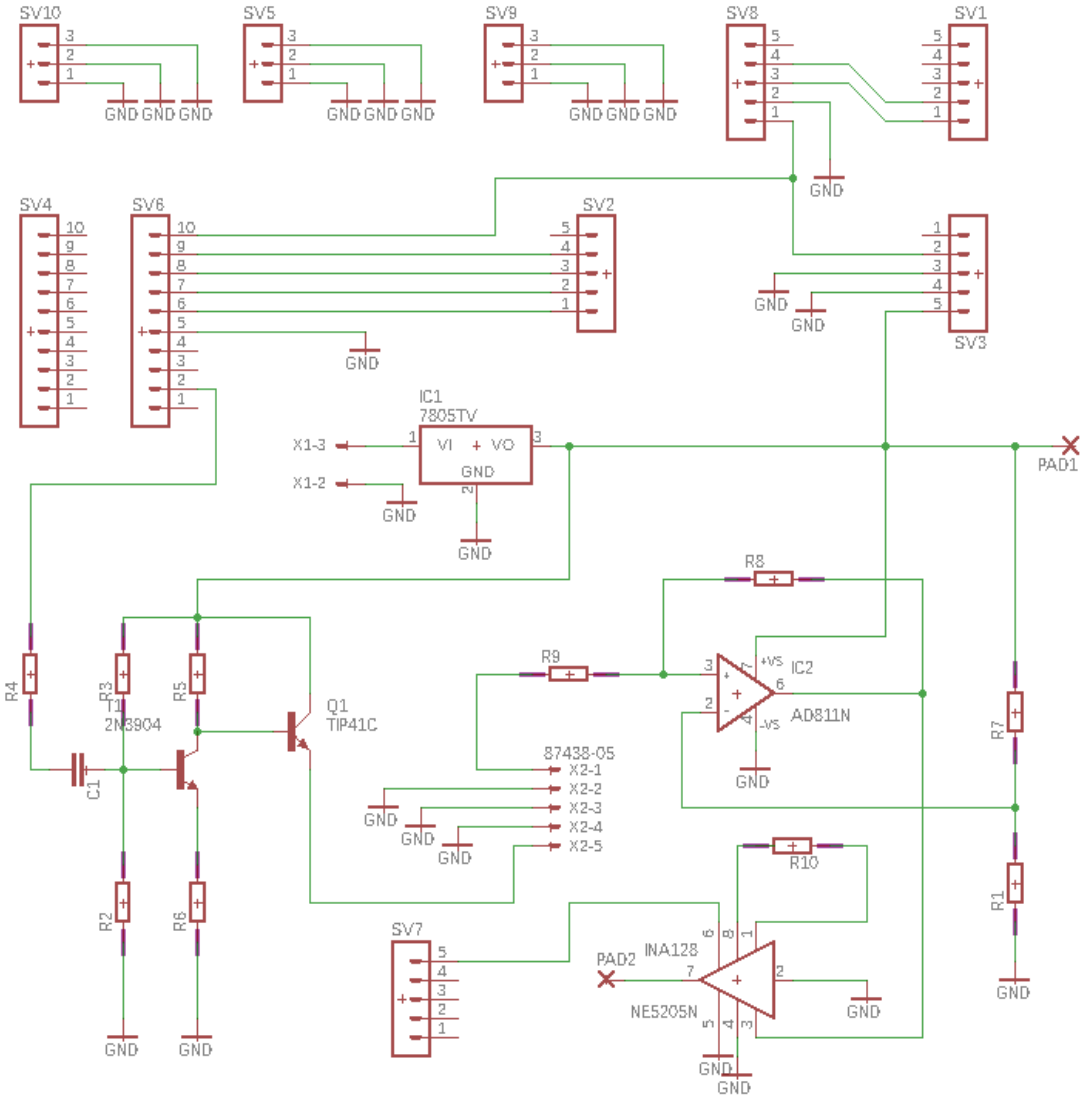

Figure 28: Circuit diagram of electrical components for allowing control, excitation and sampling of data.

4.2.1. Amplifier Design

To excite a response from the resonator, a biasing field of 730 A/m must be created as previously calculated in Section 3.2. With a biasing magnet, the required bias

field is significantly smaller. However, the amplifier circuit is designed so that it can be used for a sensor with or without a biasing ribbon. This is implemented by a single variable resistor that changes the signal bias. With the proposed coil designs the required current in the primary coil can be calculated using:

$$I(t) = \frac{B(t)L}{\mu N}. \tag{4.1}$$

Here L represents the length of the primary induction coil that will generate the magnetic field responsible for excitation, B the required magnetic field strength in Tesla, N the number of windings present in the coil and μ the effective permeability of the coil. Using $L = 45$ mm, $N = 60$ and $\mu = 4\pi \times 10^{-7}$H/m (the permeability of air), a required magnetic field with bias 730 A/m and AC swing of 10 A/m translates to a required alternating current of 7.5 mA with a 550 mA DC offset. An AD9850B SDD Signal Synthesizer is used to generate a sine signal of varying frequency with an amplitude of 0.5V with a 0.5V offset. This module cannot provide sufficient current to generate the required electrical current through the primary coil. A two-stage non-inverting current amplifier as shown in Figure 29 was designed to accomplish this.

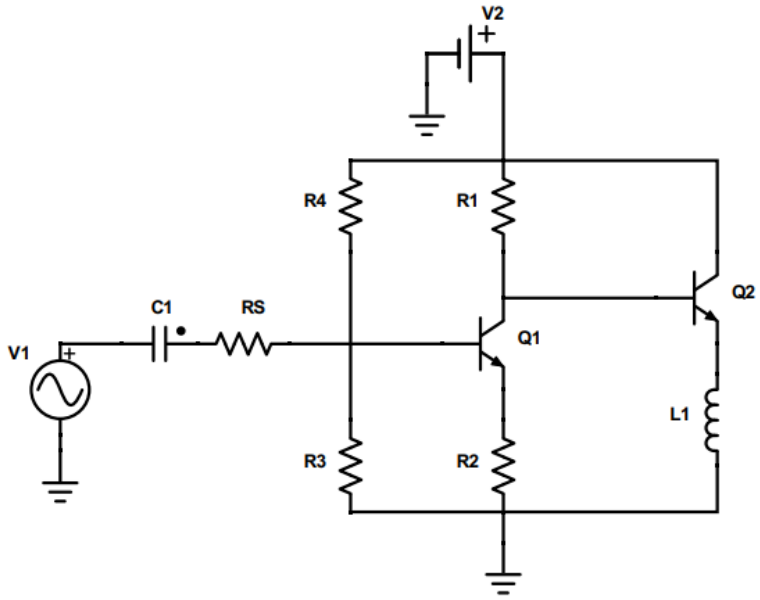

Figure 29: Circuit diagram of the two-stage non-inverting current amplifier used to generate sufficient electrical current in the primary coil for excitation.

A 2N3904 NPN Silicon Transistor, Q1 in Figure 29, is used for the first stage of the amplifier. The first stage of the amplifier adds the required bias to the signal before the current is amplified by the second stage. For the chosen values $R_S = 100\ \Omega$, $R_1 = 3.4\ \text{k}\Omega$, $R_2 = 560\ \Omega$, $R_3 = 620\ \Omega$, $R_1 = 2.1\ \text{k}\Omega$ we can calculate the output voltage after the first stage by first calculating the current through R_3:

$$I_{R3} = \frac{5}{R_3 + R_4} = 1.9\ \text{mA}. \tag{4.2}$$

Then the voltage over R_3, namely $V_{R3} = R_3 \times I_{R3}$, is equal to 1.18 V. Analysing the current path through transistor Q1, with $V_{CE} = 0.7$ V, the current through R_2 is:

$$I_{R2} = \frac{1.18 - 0.7}{R_2} = 0.86\ \text{mA}. \tag{4.3}$$

Since the current through R_1 is assumed to be the same as through R_2:

$$V_{R1} = R_1 \times I_{R2} = 3400 \times 0.00086 = 2.92\ \text{V}. \tag{4.4}$$

The output voltage after the first stage is calculated as $2.08\,V$. Q2 is selected as a TIP41C NPN Bipolar Amplifier from ON Semiconductors. The TIP41C is rated for 6 A collector current with 65 W power dissipation due to an added heatsink. It is well suited for continuous use with dc current. Analysing the current loop for Q2 with $V_{CE} = 0.7$ V, the current through inductor L1, with $L_1 = 42$ µH and $\omega =$ 58 kHz, can be calculated as:

$$I_{L1} = \frac{2.08-0.7}{\omega \times L_1} = 560 \text{ mA} \tag{4.5}$$

This proves the designed amplifier is capable of supplying enough DC current to bias the amorphous ribbon and excite a signal.

4.2.2. Pre-Amplifier Design

A pre-amplifier circuit was designed to scale the response from the secondary coil before it is sampled on the analog port (ADC0) on the Arduino Due. A maximum signal amplitude of 220 mV_{pp} around 0 V_{DC} is measured from the pickup coil. Sampling the signal with the Arduino requires a voltage between 0 – 5V, scaled to 0 - 4096 using 12-bit resolution. To achieve this, a two-stage amplifier is applied consisting of an op-amp and a differential amplifier as shown in Figure 30. An AD8031 Operational Amplifier was chosen for the first stage of the amplification process. This op-amp is relatively inexpensive and readily available. The op-amp is integrated as a non-inverting differential amplifier. This means that the difference between the positive and negative input ports are multiplied by a constant gain, determined by the resistor ratio. A voltage divider keeps the negative input pin at a 2.5 V reference voltage.

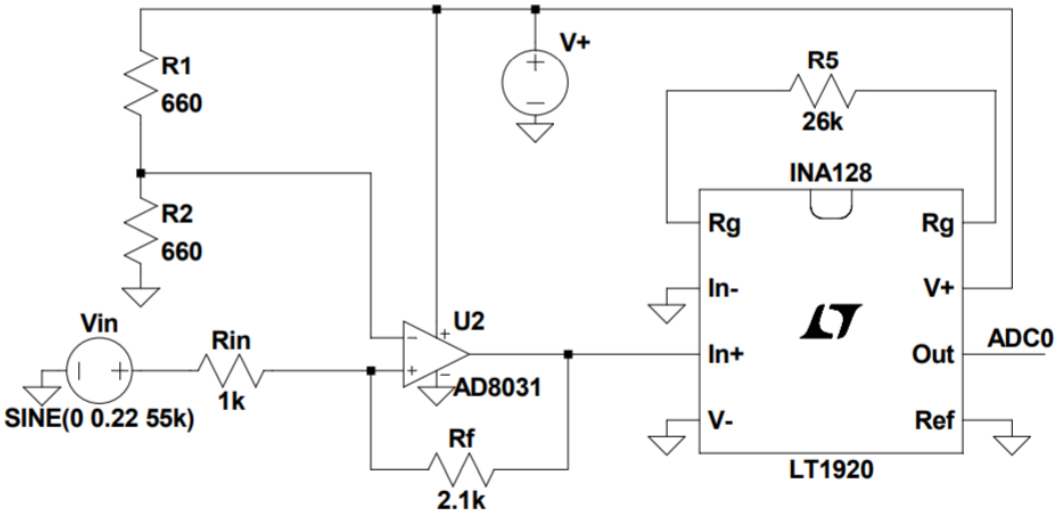

Figure 30: Two-stage pre-amplifier circuit responsible for signal conditioning before analoq sampling.

Figure 31 below shows the signal measured as it is amplified by the pre-amplifier in two steps. With the reference voltage set by the first stage, the signal passes to the INA128 Differential Amplifier. This amplifier was chosen because of its high slew rate of 4 V/µs and maximum gain of 10 at frequencies around 60 kHz up to 100 kHz. The amplification is defined by the gain equation:

$$G = 1 + \frac{50k\Omega}{R_G}. \tag{4.6}$$

Here $R_G = 26$ kΩ resulting in $G = 2.92$. The ADC0 port on the microcontroller is capable of measuring between 0 and 5V. This gain is sufficient to ensure that the value does not go above 5 V in spite of possible signal amplitude variability induced by different ribbon magnetizations.

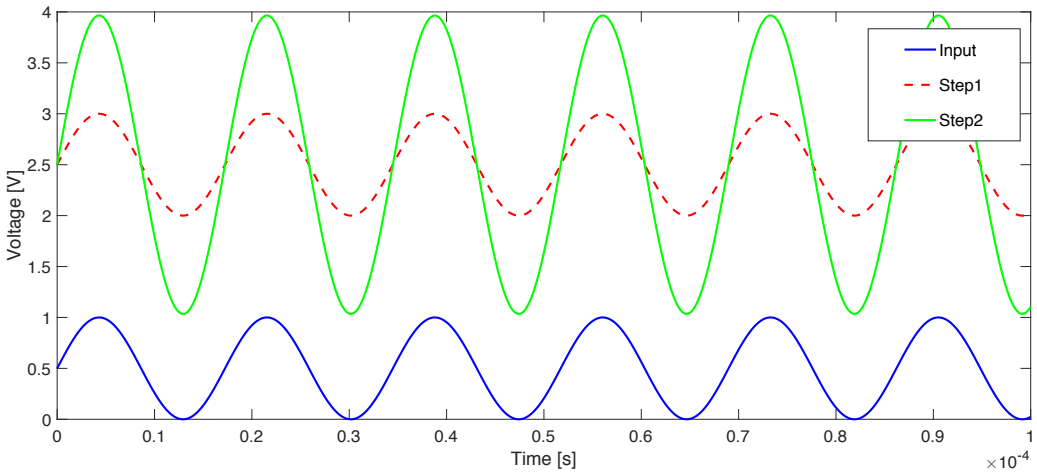

Figure 31: Stepwise representation of signal amplification of the pre-amplifier before sampling. Step 1 is the implementation of the differential amplifier, and Step 2 the implementation of the Instrumentation Amplifier.

4.2.3. Power Circuit Design

Components included in the design of the power supply circuit is the Arduino microcontroller, the signal synthesizer, the Bluetooth module and the pickup-signal pre-amplifier, which requires a supply voltage of 5 V. A voltage regulator capable of supplying a steady 5V output was chosen, namely, the L7805CV Voltage Regulator from Microelectronics. The regulator is rated for a maximum current of 1.5 A. Experimental results show a maximum current draw of 650 mA.

4.2.4. PCB Design

A PCB was designed for the PRD. This allows for a more compact device, thereby ensuring portability. The PCB layout considers the placement of the power supply circuit, the signal amplifier and the pickup-signal pre-amplifier. The PCB was designed using Eagle (Autodesk Eagle, 9.01) and manufactured using a ProtoMat S-Series PCB milling machine (LPFK, ProtoMat S63). **Error! Reference source not found.** shows the detailed PCB layout incorporated in the PRD. The board is milled from a single-sided silicon wafer in stages. 0.02 mm copper tracks are used with a thickness of 35 µm.

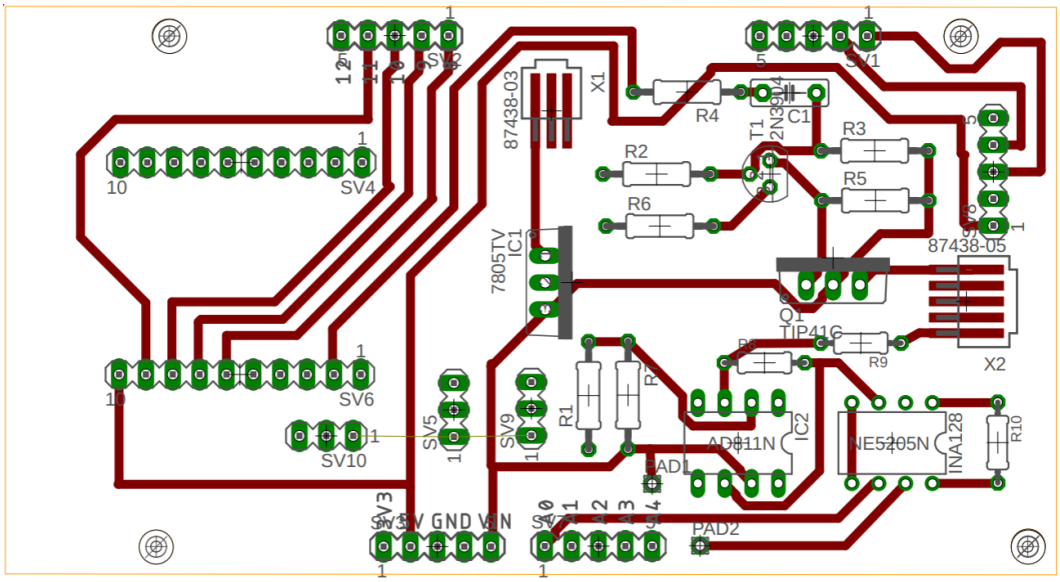

Figure 32: PCB design incorporated in the PRD which houses all the electrical components.

4.3. Hardware Design

This section includes the detailed designs for the excitation and detection coils and the housing used for PRD. All designs were done on Autodesk Inventor® and manufactured by the method of 3D-Printing.

4.3.1. Coil Design

For the detection of the sensor response, it is important that the secondary (pickup) coil is co-axially aligned and local to the sensor. Figure 33 shows the orientation of the primary and secondary coils. Both coils were 3D printed with black Acrylonitrile Butadiene Styrene (ABS). The secondary coil, which is the smaller of the two, fits inside the primary coil. The sensor, in turn, is placed inside the secondary coil. A copper winding exists around the primary and secondary coils of 60 and 350 turns, respectively.

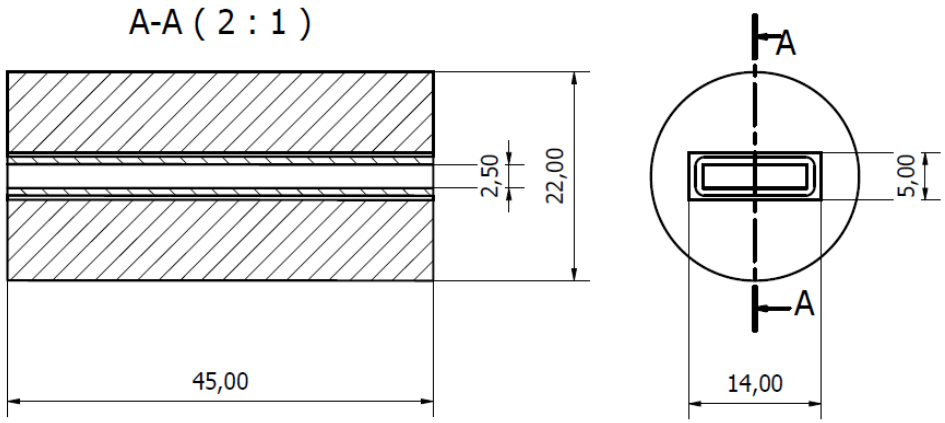

Figure 33: Diagrams showing the co-axial alignment of the primary and the secondary coil.

4.3.2. Housing Design

The housing serves as an enclosure that protects the microcontroller and electrical circuitry inside. It was designed using Autodesk Inventor and manufactured using 3D printing and consists of a body and a lid, which are fastened together using screws. The housing possesses an opening through which the sensors are inserted into the pickup coil. No further openings or vents are included as the heatsink on the TIP41C transistor accounts for the required heat dissipation. The housing is shown in Figure 34 with detailed design drawings found in Appendix C.

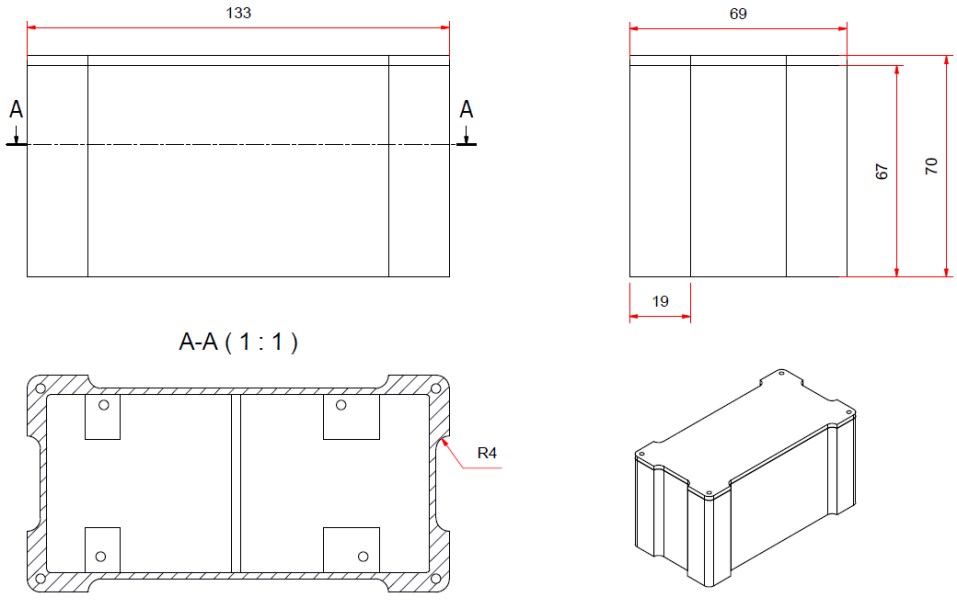

Figure 34: Projected and section view of housing body and lid. Internal mounting points are shown in the section view.

4.4. Software Design

This section includes the design of all control software used in the project. This includes the control code for the Arduino microcontroller in C, and the Java code written in Android Studio for the Android smartphone that controls the device and visualises the sampled data.

4.4.1. AD9850 Communications and Sequencing

The AD9850 is an affordable, 12-bit signal generator capable of generating a square of sine wave signal between 1 Hz and 1 MHz at 1V. The logic responsible for exciting and sampling the sensor signal from the pick-up coil is described here. The sampling method uses a three-phase fractional cascade search to find the maximum amplitude at a specific excitation frequency. The excitation frequency at the maximum amplitude is the resonant frequency of the sensor.

1. The AD9850 is initialized and reset through a sequence of commands sent through digital I/O ports 8-11. First, to initialize the chip a function *AD9850_init()* is called that sets digital I/O pins to LOW. Subsequently, a function *AD9850_reset()* is called that performs a sequence of actions that resets the chip:
    - CLOCK and LOAD = LOW
    - Pulse RESET high for 5 µs.
    - Pulse CLOCK high for 5 µs.
    - Set DATA = LOW
    - Pulse LOAD high for 5 µs.
2. The ADC (Analog-Digital Converter) on the ATSAM3X8E microchip on Arduino Due has a maximum sampling speed of 1 MS/s at 12-bit resolution. The *AnalogRead()* function implemented in the Arduino IDE contains a series of actions and conversions that take 125 ns to complete. This includes a prescaler of 16 and a standard 13 cycle/conversion on the ADC chip. With a ATSAM3X8E core clock of 84 MHz, this limits the maximum sampling speed of the ADC0 port to 403 kHz (84 MHz / (16*13)). The maximum

frequency expected in the current design is 60 kHz. Although the ADC is fast enough to prevent aliasing (Nyquist), a higher sampling rate is advantageous since it is more likely to catch the peak amplitude, as described in Figure 35.

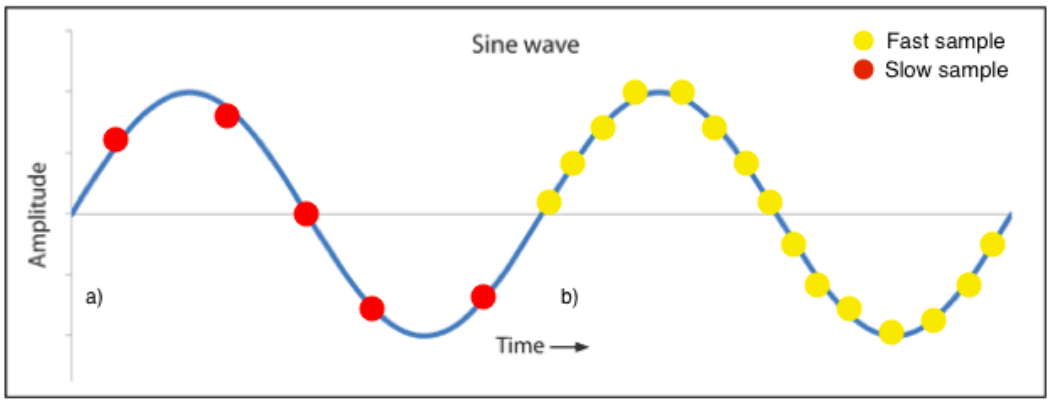

Figure 35: The distribution of samples across a sine wave signal with frequency F. a) sampled at 5F. b) sampled faster at 15F. Sampling at 5F is not sufficient to ensure that the maximum point will be sampled. The larger the resolution of the digital sampling system, the better. Sampling at 15F significantly increases the likelihood of the maximum point being sampled.

This ADC speed can be increased by switching from of Single Conversion Mode to Freerun Mode. In Freerun Mode, the conversion is only done once (25 clock cycles). Thereafter, the ADC starts the new conversion when the previous is finished. This has been implemented through 15 commands:

- pmc_enables_periph_clk(ID_ADC):
  This command enables the distribution of the clock to the ADC.
- adc_init(ADC, SystemCoreClock, adc_freq_max, adc_startup_fast)
  Initialize the ADC converter and set to maximum speed.
- adc_disables_interrupt(ADC, 0xFFFFFFFF);
  Disable all ADC interrupts.
- adc_sets_resolution(ADC, ADC_12_BITS);

Set resolution to 12-bit (Maximum resolution). This scales the 0 - 5V analog input to 0 – 4096.

- adc_configures_power_save(ADC, 0, 0);
  This disables the sleep mode.
- adc_configures_timing(ADC, 0, ADC_SETTLING_TIME_3, 1);
  Sets the timing to default values.
- adc_sets_bias_current(ADC, 1);
  Sets the bias current to maximum for maximum performance.
- adc_stops_sequencer(ADC);
  The sequencer will not be used.
- adc_disables_tag(ADC);
  Tags are used by the sequencer, which will not be used.
- adc_disables_ts(ADC);
  Disable the temperature sensor.
- adc_disables_channel_differential_input(ADC, ADC_channel_7);
  This disables the differential input from channel seven, namely ADC0.
- adc_configures_trigger(ADC, ADC_TRIG_SW, 1);
  Triggering from software and run in Freerun Mode.
- adc_disables_all_channels(ADC);
  This disabled all the AC channels.
- adc_enables_channel(ADC, ADC_CHANNEL_7);
  This enables just one channel for conversion. Normally, the ADC clock is divided among all active channels.
- adc_starts(ADC);
  Start the ADC converter.

3. The Bluetooth module is initialized through serial ports TX1 and RX1. The module possesses its own connection protocol. The only interaction from the control code is through the Serial.Read() and Serial.Write() functions through the serial port.

4. Once all components are initialized, the control code is executed. This consists of three sampling stages. The first stage is shown below in Figure 36.

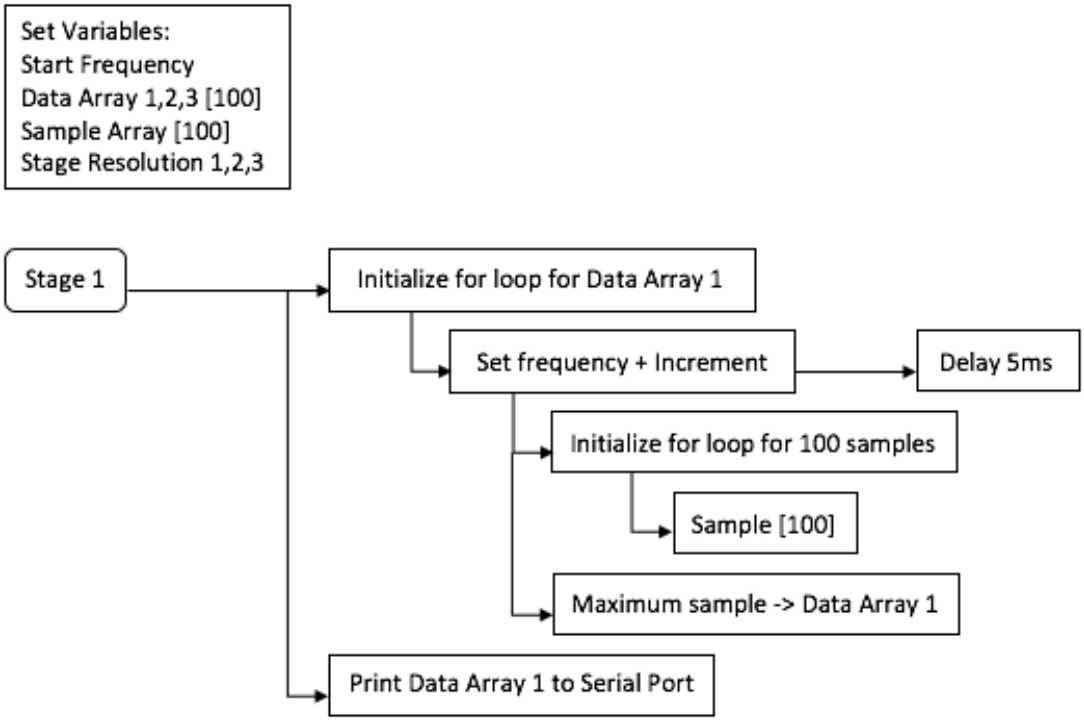

Figure 36: 1st Stage of sampling with a 50 Hz resolution.

First, all the data arrays are initialized along with the start frequency and the stage resolutions. Once initialized, the system sets the excitation frequency and 5 ms delay is given. This is to ensure that the AD9850 switches to the new frequency. One hundred samples are made at 666 kHz, whereafter the maximum value is determined with a maximum seeking function. This maximum represents the maximum sampled value for a given excitation frequency. Once the frequency sweep concludes, the data is sent to the serial port where it is printed on the display device (smartphone). The data array from stage one is then sent to stage two, as shown below in Figure 37.

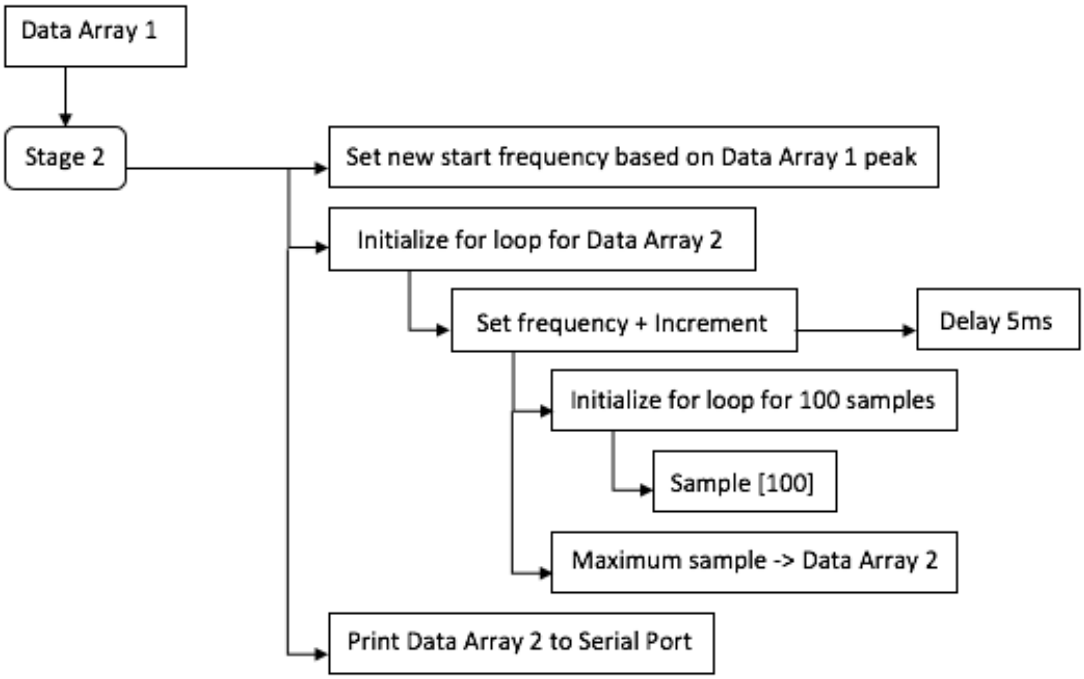

Figure 37: 2nd Stage of sampling with a 5 Hz resolution.

The data array from stage one is passed to a maximum seeking function that returns the index of the peak value. The index value is used to determine the position of the previous peak and, subsequently the start excitation frequency for the second sampling stage. The same process as described for stage one occurs, instead with a resolution of 5 Hz. Lastly, the data array for stage two is passed to the third and final stage of sampling, as shown in Figure 38.

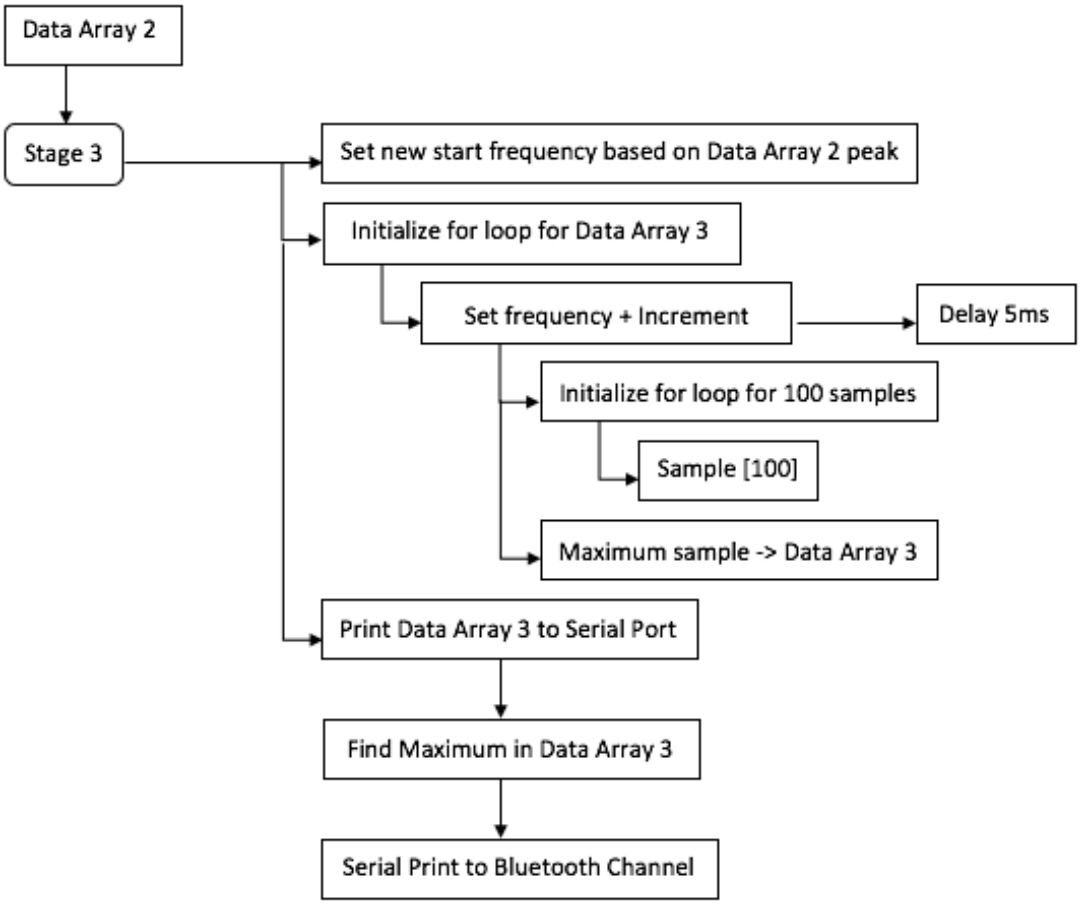

Figure 38: 3rd Stage of sampling with a 1 Hz resolution.

Once the final stage of sampling concludes with a resolution of 1 Hz, the data array is passed to a maximum seeking function. The index value of the peak is used to calculate the resonant frequency of the amorphous ribbon inside the sensor. This data is passed to the serial port and transmitted to the smartphone via Bluetooth. The application receives the data on the serial buffer, which is further described in Section 4.4.2.

4.4.2. Application Development

An application was developed using the Android Studio platform that is responsible for sending commands to the microcontroller and visualising the sampled data. The software is written in JavaScript. The implementation of an application of a smartphone contributes to the portability of the PRD. The control code is presented

in Figure 39 as a flow diagram. Screenshots from the application runtime are given in Appendix E.

1. When the application is launched it establishes whether Bluetooth is enabled. If not, it prompts user permission to enable. Once Bluetooth is enabled, a list of paired devices is displayed. The user selects the Bluetooth device to connect to. Once a connection is established, the application transitions to the menu where three buttons are displayed, namely ON. OFF and OUTPUT.
2. If the ON button is pressed, the application initiates the sampling process of the PRD via serial command. The sampled data is saved in three arrays for each of the search phases. The system sets a flag value, which indicates that data is available for analysis.
3. If the OFF button is pressed, the system interrupts the sampling phase and resets all sampled values to zero.
4. If the OUTPUT button is pressed, the system first determines whether the sampling process has been completed. Once this is confirmed a command is sent to the microcontroller that prints the three data arrays to the Bluetooth serial buffer. The three data arrays with 100 elements each are printed to a data array with a size of 300 elements. This array is passed to the display function by intent.
5. The application transitions to the display function which utilises the GraphView Android library. The received data array is used to populate a data point series consisting of x and y coordinates. Once completed, the graph is appended with the data point series.

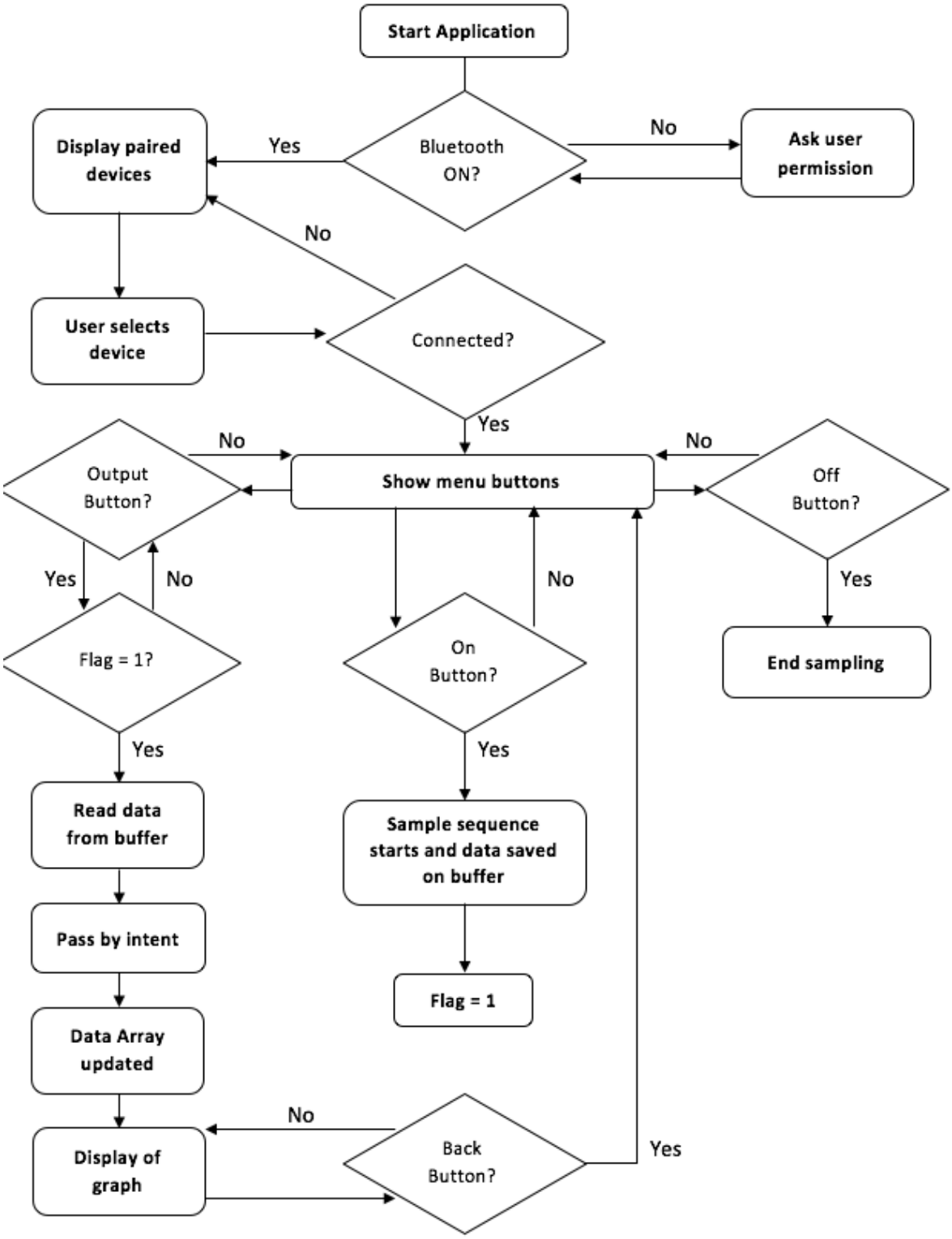

Figure 39: Process flow diagram showing the operation of the control application for the PRD.

4.5. Evaluation

4.5.1. Experiment motivation

It has been proven that the sensor is sensitive to changes in medium viscosity and density. An extensive testing process is required to access the validity of the sampling process implemented with the use of the in-field interrogation module. The digital sampling algorithm samples at $f_s = 666\,kHz$. The maximum and implemented excitation frequency is effectively 62 kHz. Although f_s is fast enough to prevent aliasing as described by Nyquist, it does, however, mean that every wave period is sampled 10 times on average. Also, with a 12-bit resolution, the signal can be digitized with a maximum resolution of 1.22 mV. Further queries exist regarding the lead time required for the circuit and the subcomponents to respond to the microcontroller commands. It is crucial that the sensor must first respond to the excitation frequency before the samples are made. A software delay of 5 ms is implemented between frequency update and analog sampling. The sampling algorithm performance must be characterised to ensure it is capable of making accurate measurements.

4.5.2. Methodology

The Portable Read-Out Device is evaluated by studying the characteristic response curve that it measures. To achieve this, a sensor is placed inside the device and a measurement is taken. Furthermore, to determine the validity of the sampling algorithm implemented in the PRD it will be tested alongside another method of detecting the resonant frequency, namely an Oscilloscope. A Helmholtz coil (Schwarzbeck Mess-Elektronik, HHS 5201-98) setup is used to create an excitation magnetic field. The sensor is placed inside the field and connected to an Oscilloscope and the input pins on the PRD simultaneously. The excitation coil from the PRD is not used to isolate the effect of different excitation fields between the two methods. The maximum signal amplitude and corresponding frequency are recorded for 100 sensors.

4.5.3. Results and Discussion

Initial tests were performed to establish whether the sampling software is able to excite and detect a valid sensor response. As previously described (Section 4.4.1), the search algorithm sweeps the frequency spectrum in three stages, whilst recording the amplitude response. During the first stage, the resolution is set to 50 Hz as the algorithm passes from 56 kHz to 61 kHz. The maximum amplitude is determined across the frequency band and the corresponding frequency is determined. This frequency is passed to the next stage and used to determine the new starting frequency. The resolution is decreased to 5 Hz as the algorithm sweeps the frequency band again. The maximum amplitude and corresponding frequency are recorded and again passed to the third and last search phase, with a resolution of 1 Hz. 100 Maxims are recorded and displayed for each search phase. The result can be seen in Figure 40 where stage one is displayed from 0-100, stage two from 100-200 and stage three from 200-300. The algorithm passes the maximum amplitude and corresponding frequency on to the next search phase, where the resolution is increased. A 50 Hz resolution (Figure 40 Top-Left) clearly shows the sensor behavior across the excitation frequency band. With an increased resolution of 5 Hz (Figure 40 Top-Right), a characteristic curve is still observed with a clear maximum. However, with an increase to 1 Hz resolution (Figure 40 Bottom) the 12-bit sampling loses resolution with observed variations of 1-2 analog units. 12-bit sampling on a 5V port means there is a resolution of

$$R = \frac{Voltage}{2^{12}} = \frac{5}{4096} = 1.22 \text{ mV}. \tag{4.7}$$

Although this does not allow a smooth curve as for 50 Hz and 5 Hz, the maximum is still measurable within a 10 Hz band. This is the accuracy of the system. To show this is sufficient and that the sampling algorithm is capable of measuring the resonant frequency, a second test was performed. At this point, a magnetic sensor is excited by a Helmholtz coil, and the resonant frequency determined with an Oscilloscope (Method A) and with the sampling algorithm (Method B). A constant H_{DC} field of 750 A/m was generated with H_{AC} also constant at 100 A/m.

Measurements were recorded within a 10 Hz resolution. For all 100 sensors that were tested, both methods measured the same values with a correlation of 100%, as seen in Figure 41.

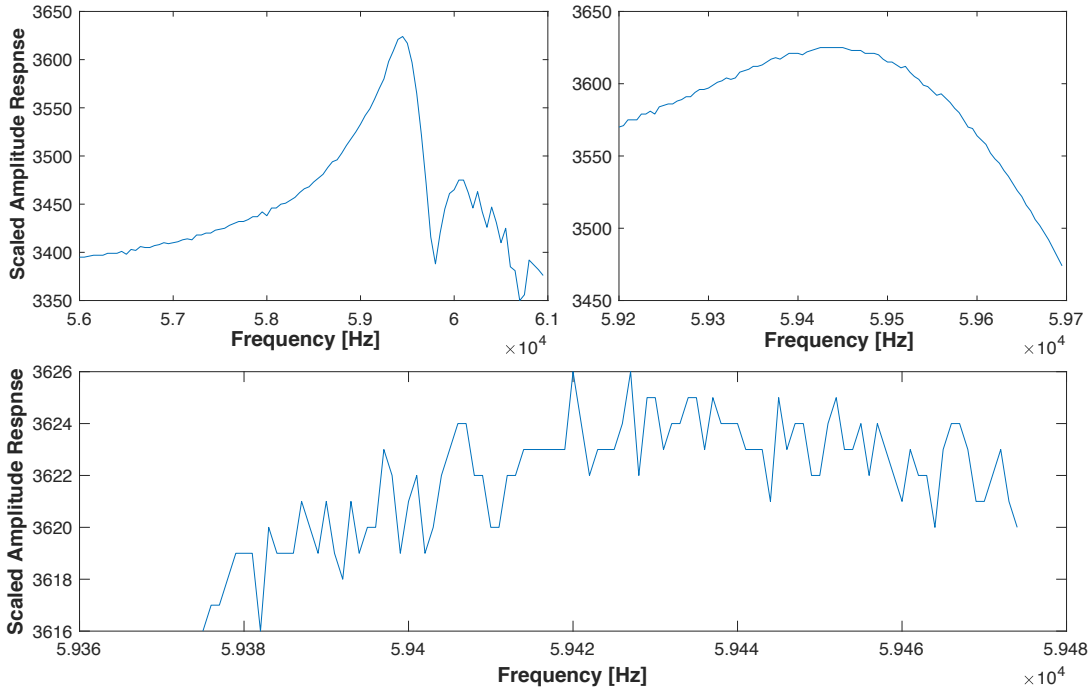

Figure 40: Three-stage search algorithm measuring sensor amplitude response with resolutions (Top-Left) 50 Hz, (Top-Right) 5 Hz and (Bottom) 1Hz.

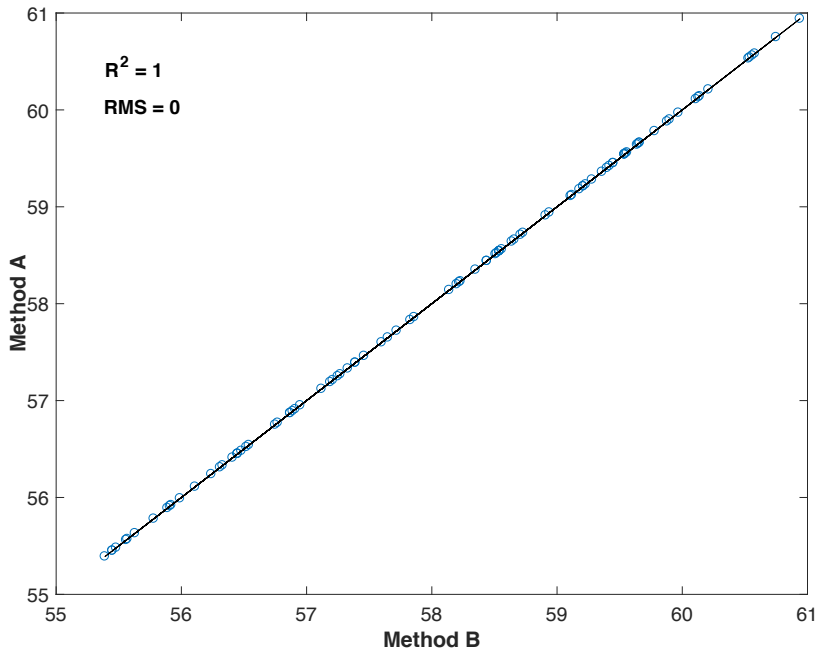

Figure 41: Correlation between Oscilloscope (Method A) and sampling algorithm (Method B) measurement of resonant frequency for 100 sensors.

5. System Improvements

This chapter addresses specific aspects within the current sensor design and presents a solution to each.

5.1. Non-corrosive Layer Addition

5.1.1. Background

For the sensor to be a viable solution for WC sensing it needs to be capable of operating in harsh conditions. This included operating in brine solutions found when drilling with a salinity up to 260,000 ppm (Al-Shalabi, 2016). The magnetic characteristics and performance of the sensor were investigated under various corrosive conditions over the period of twenty days. The magnetic properties of a 4 mm x 2 mm amorphous ribbon were characterised using a Vibrating Sample Magnetometer (VSM). The ribbon was secured to the sample holder using silicon grease and the sample holder was vibrated with an amplitude of 1 mm and a frequency of 83 Hz while sweeping the applied magnetic field from -15 kOe to 15 kOe. As seen in Figure 43, over a period of twenty days, the saturation magnetisation of the sensing ribbon decreased by 67%, when the ribbon was immersed in water, due to corrosion. On the other hand the value of resonant frequency has remained relatively unchanged (Figure 44), which is expected, since it is related to the mechanical properties of the ribbon and not the magnetic ones. However, the reduction in magnetisation leads to a reduction in the sensor signal amplitude, making it harder to detect. The effects of corrosion are visible in Figure 42.

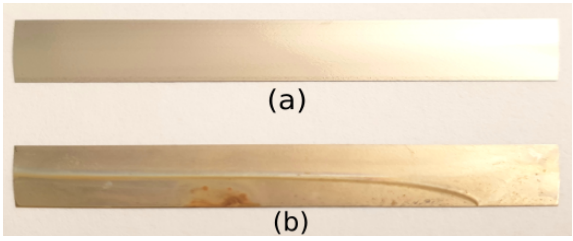

Figure 42: Two ribbons showing (a) a new ribbon without exposure to water and (b) a ribbon exposed to water for 2 days showing signs of corrosion (oxidation).

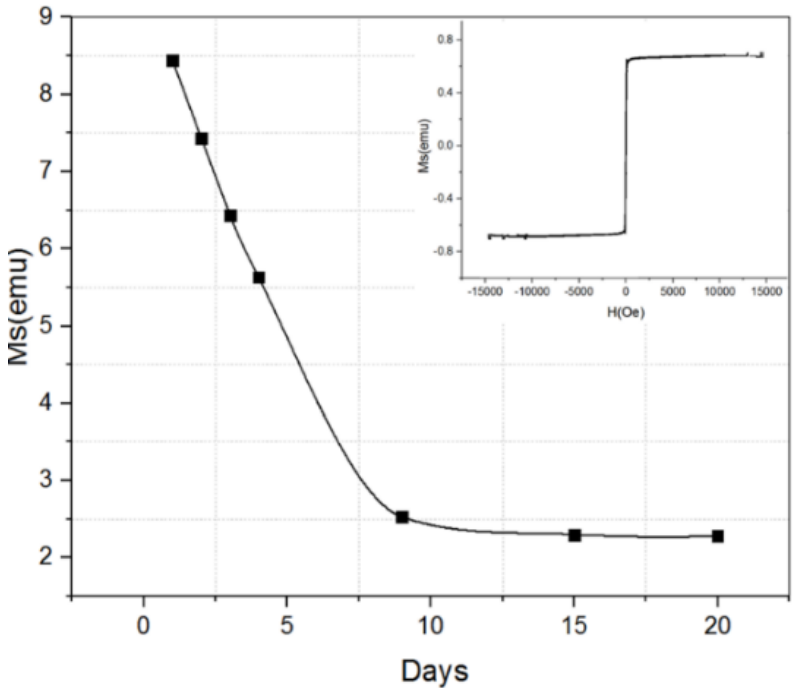

Figure 43: Magnetisation curves of amorphous ribbon before and after corrosion.

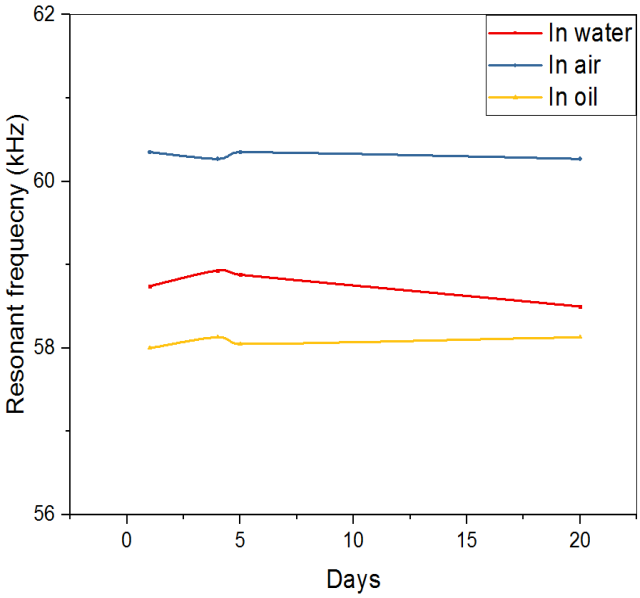

Figure 44: Resonant frequency of amorphous ribbon without coating.

In order to find a solution for this, different coatings were applied to the sensors, i.e. Teflon (Teflon ® AF, DuPont), Parylene C (PDS 2010, Parylene Deposition System). Teflon has been found to provide the best performance, acting as an anti-corrosion layer and offering chemical resistance and low moisture absorption (Brinker, 1991). The Teflon was applied to the sensor ribbons by dip coating, which

is a simple, low-cost and waste-free coating process. By immersing the ribbons into Teflon solution and withdrawing them at a constant speed, a two-sided Teflon coating of ~2.5 µm thickness has been deposited on the sensor surface as shown in Figure 46. Figure 45 shows the ribbon without the Teflon coating.

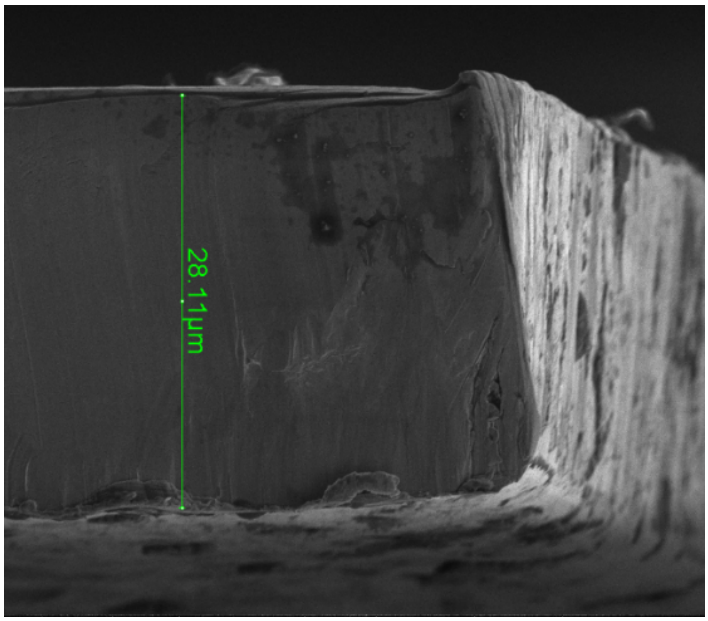

Figure 45: Scanning electron microscope images showing the amorphous ribbon cross-section without the non-corrosive Teflon layer.

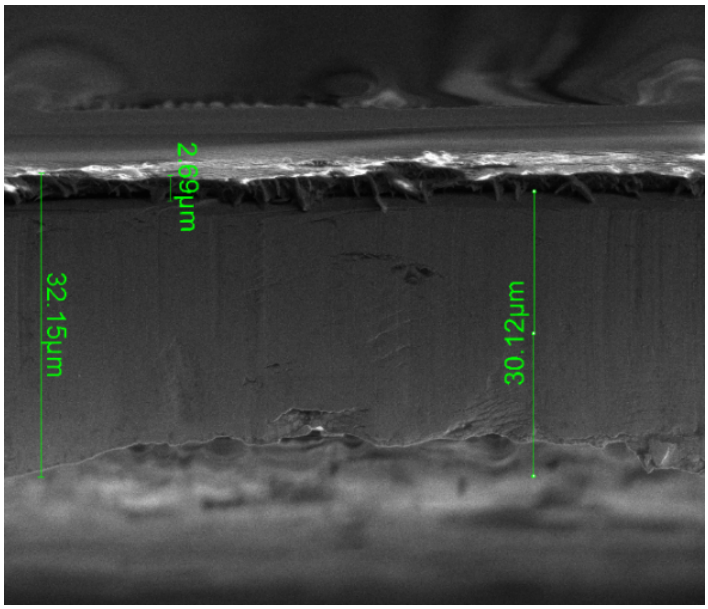

Figure 46: Scanning electron microscope images showing the amorphous ribbon the cross-section with the Teflon layer.

5.1.2. Results and Discussion

With this coating, the saturation magnetisation of the sensors remained stable for twenty days in air, water and oil (Figure 47) enabling reliable sensor deployment. An initial reduction of the resonant frequency of 3% (Figure 48) following the application of a non-corrosive coating was observed, which can be explained by the additional mass loading. A magnetoelastic sensor with a mass m_0 with initial resonance frequency f_0, when subjected to a mass loading of Δm, demonstrates a decrease in resonance frequency of (Landau, 1986):

$$\Delta f = -f_0 \frac{\Delta m}{2m_0}. \tag{5.1}$$

The weight of the added coating can be calculated using the coating density of 1780 kg/m^3 and by assuming a uniform thickness of 2.5 µm. The frequency shift from equation 5.1 is 2.13%, which is in close agreement with the experimentally found value of 3%. The results for tests using Parylene C can be found in Appendix D.

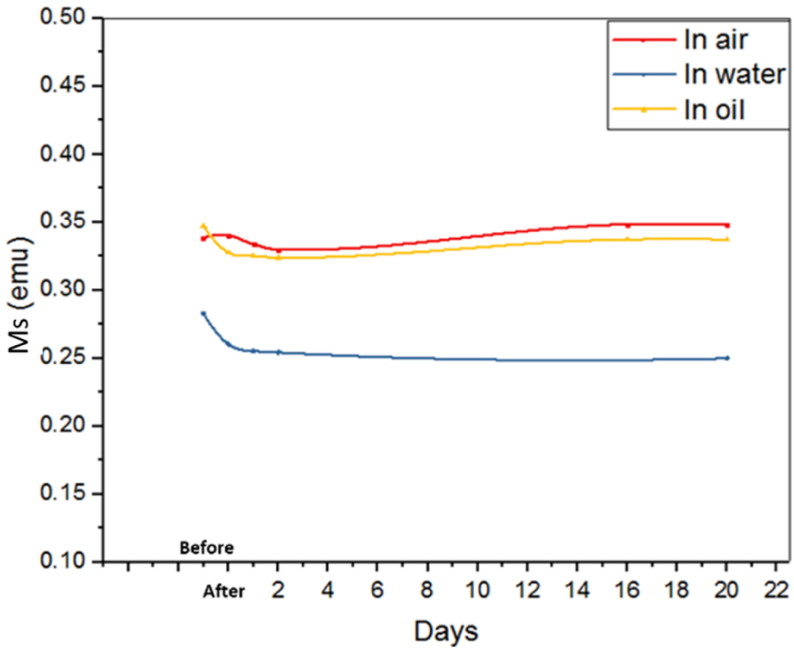

Figure 47: Saturation magnetisation of magnetic ribbon before and after coating with Teflon and during 20 days in air, water and oil.

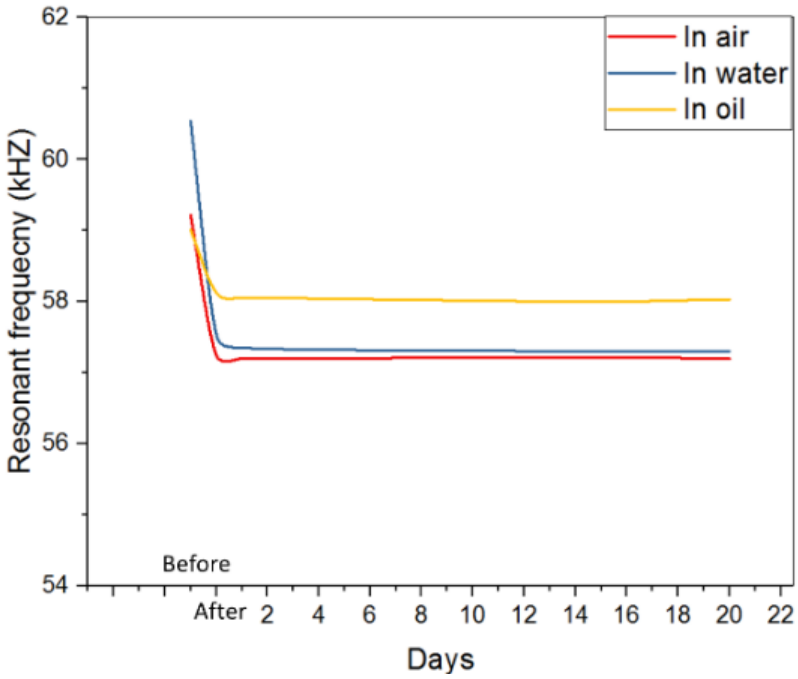

Figure 48: Resonant frequency of magnetic ribbon before and after coating with Teflon and during 20 days in air, water and oil.

5.2. Modified Housing Design

5.2.1. Background

The AM tag currently used in the PRD allows for the quantification of static oil/water emulsions inside the 640 mm^3 sensor body. The liquid is injected into the housing and measured. This allows for 'spot' sampling, but it does not allow the quantification of WC in dynamic applications where the oil/water mixture is flowing inside a pipe. Commercially available WC sensors determine the WC of oil/water mixtures inline as it flows inside transportation pipes. The modified sensor housing must allow liquid flow through the housing whilst allowing contact between the sensor ribbon and the liquid medium. Vibrations caused by the flowing liquid and the effect on the sensor will be investigated.

5.2.2. Design

The housing is designed to fit inside a 25 mm pipe without restricting the flow of fluid. This is crucial in water cut applications since most sensing is done inline. The housing consists of three parts, namely the primary and secondary coils and the diffuser, as shown in Figure 49. All components were 3D printed using a Formlabs Form stereolithographic printer (Formlabs, Form 2). The ribbon-end is attached to the upstream side of the secondary coil, consisting of 350 turns of 0.1 mm enameled copper wire. The primary coil, consisting of 100 turns of 0.6 mm copper wire, is larger than the secondary coil and fits over it. The primary coil incorporates a buffer that consists of a 0.5 mm spacing into which the back end of the ribbon fits. This prevents excessive movement of the ribbon in the flow regime and isolates from the signal damping effect that may result. A diffuser is attached to the secondary coil and allows the uniform dispersion of liquid over the ribbon surface during high flowrate applications.

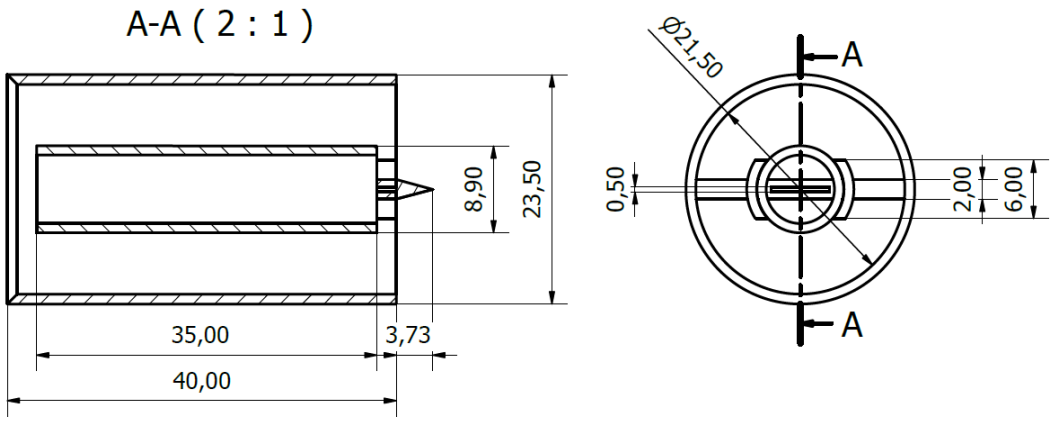

Figure 49: Schematic showing the modified housing design (left) front view and (right) sectional side view.

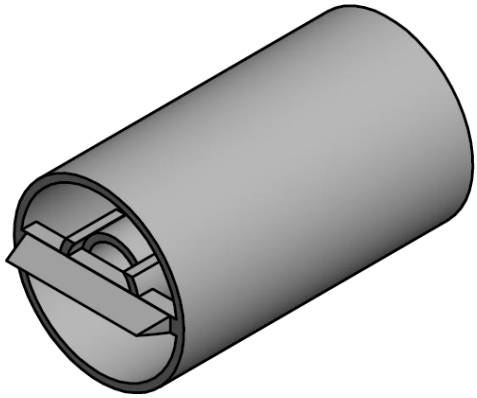

Figure 50: Isometric view of the housing assembly. The diffuser is angled at 15 degrees and the primary coil is chamfered to reduce the flow obstruction.

5.2.3. Test Methodology

The sensor housing is tested in a water flow loop with variable flowrate using a Huber high precision thermos-regulator (Huber, Pilot One) to determine whether the sensor is sensitive to the effects of varying flowrates. The sensor is placed in a transparent tube with a diameter of 28 mm. Distilled water at 20° C is pumped through the flow loop using the Huber thermo-regulator with pump speeds between 1500 RPM – 4500 RPM. The pump speed is converted to flowrate in liters per second using a flowmeter shown in Figure 51 (right).

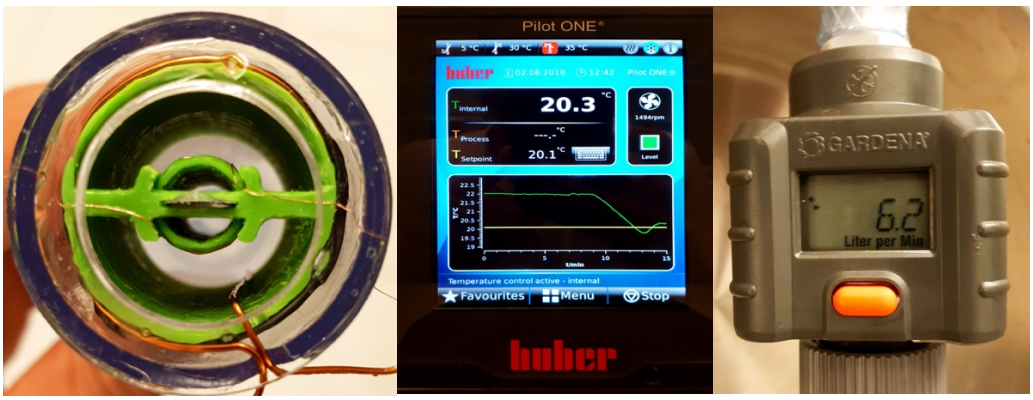

Figure 51: (left) 3D Printed primary and secondary coils are mounted inside the flow loop. The amorphous ribbon is seen inside the secondary coil. (center) The control interface for the flow temperature and flowrate settings. Measurements are started when the temperature reaches the setpoint of 20° C. (right) Gardena flowmeter which is used to measure the volumetric flowrate inside the flow loop.

An alternating signal is generated using a signal generator (Agilent 20 MHz Function Generator, 33220A). The signal is filtered using a low pass filter (Stanford Research Systems Filter, SR560) at 30 kHz with an attenuation rate of 6 dB/octave and gain of 10. The signal is then amplified using a bipolar amplifier (NF, HSA 4012) with a gain of 20. The output of the amplifier is attached to the primary coil which generates the magnetic excitation field. This, in turn, excites a measured sensor response in the secondary coil using a digital storage oscilloscope (Agilent Infiniium, DSO90404A). The measured signal is processed using an FFT which indicates the frequency components present in the signal. The response signal is comprised of the resonance signal and excitation signal. Extracting the resonance signal at the excitation frequency (f_e) is difficult because the excitation signal is very large compared to the resonance component from the ribbon. For this reason, the 1st ($2f_e$) and 2nd ($3f_e$) harmonic components are monitored and used to determine the resonant frequency. The excitation frequency is varied until $2f_e$ and $3f_e$ reaches a maximum, indicating the excitation frequency. Figure 52 below shows the excitation frequency along with the 1st and 2nd harmonic peaks as measured using the oscilloscope.

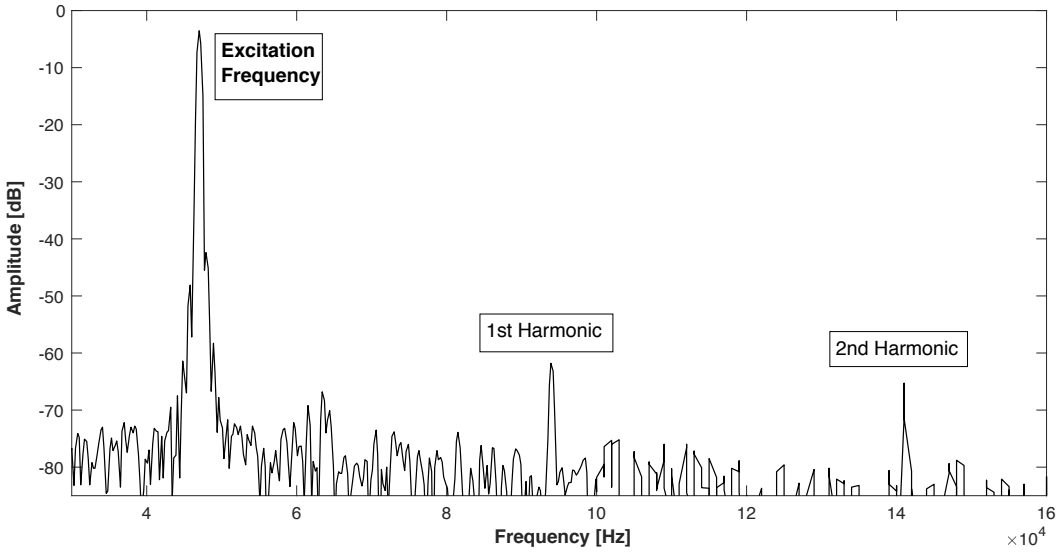

Figure 52: FFT of the response signal showing the excitation frequency $\boldsymbol{f_e}$ and the harmonics at $\boldsymbol{2f_e}$ and $\boldsymbol{3f_e}$.

5.2.4. Results and Discussion

The modified sensor housing is tested for flow sensitivity in a turbulent liquid flow regime. The resonant frequency of the sensor is measured at increasing flowrates, which induces an increasing amount of shear stress on the surface of the ribbon due to surface drag. Experimental results are shown below in Figure 53.

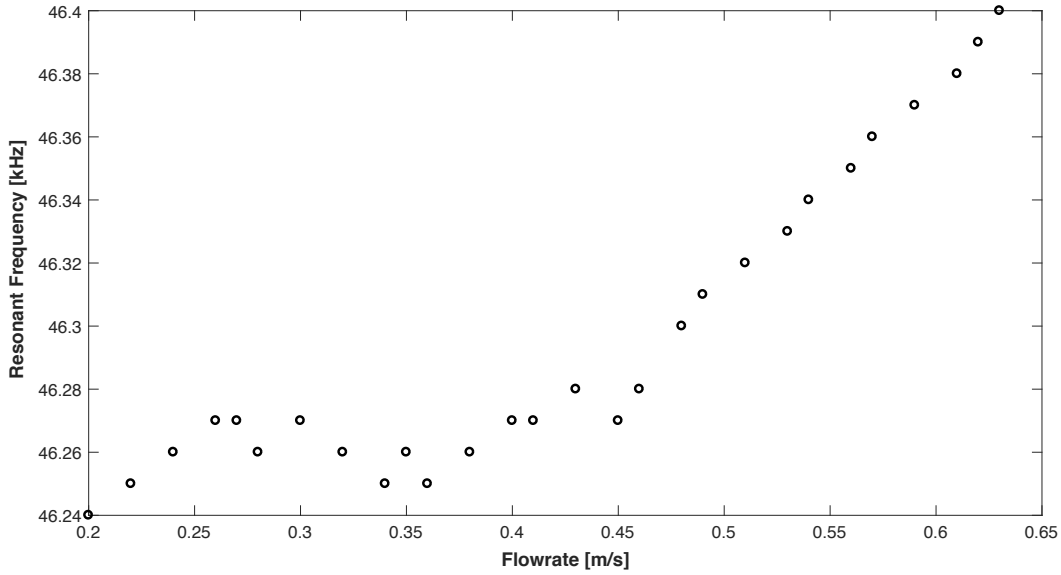

Figure 53: Resonant frequency response measured in flow loop with varying flowrates.

Figure 53 shows stable measurements in resonant frequency from flowrates 0.2 m/s to 0.45 m/s with 10 Hz variations that are attributed to measurement error. The 1st and 2nd resonant peaks are measured at a maximum value within a 50 Hz window due to signal noise. Within the 50 Hz window, the resonant peak can increase or decrease by 0.5 dB, which makes the determination of a "true peak" difficult within this range. To ensure measurements are as accurate as possible, a measurement is made once the peak amplitude decreases due to an increase of excitation frequency. Doing this ensures that the measurements reflect the reality of the ribbon vibration frequency with an accuracy of 10 Hz. Once the flowrate is increased above 0.45 m/s, a linear trend is measured with a sensitivity of 800 Hz/m·s^{-1}. However, given

the context of viscosity measurements made with the sensor, it can be regarded as insensitive to flowrate. Previous work has shown that the sensor can distinguish the three phases, namely oil, water and air with a reduction of 3.37 kHz in resonant frequency from exposure in water to oil. The change in resonant frequency within the expected operational environment is larger than the 150 Hz measured for flowrates from 0.2 m/s to 0.63 m/s by a factor of 225. This proves the modified housing for the sensor allows for in-flow measurements at defined temperatures without interference from the flow regime. It must be noted, however, that the measured linear response would allow for the sensor to be used as a flowrate sensor given a fluid at constant temperature and viscosity.

6. Conclusion

6.1. Summary

This project has presented a novel method for detecting watercut in oil. The sensor response allows distinguishing the three phases air, water and oil either by the signal amplitude or resonant frequency changes of the sensor. Amplitude changes in impedance measurements of 75% (1.93 kΩ) and 99% (2.4 kΩ) have been observed for loaded sensors in water and oil, respectively, compared to unloaded sensors in air. The corresponding resonant frequency changes were 0.46% (0.99 kHz) and 3.88% (4.37 kHz). The sensor enables water fraction quantification for crude oil emulsions with 10% – 90% WC with known temperature, but is characterised by $\Delta f = 28.5\emptyset - 2400$ for 10% - 80% WC due to non-linear behavior at 90% WC. The sensor has been shown to be insensitive to an increase in pressure from 100 kPa to 17 MPa, which is equivalent to conditions found 11.5 km downhole. The addition of a modified in-flow sensor housing has shown the sensor to be insensitive to water flow at flowrates from 0.2 m/s to 0.63 m/s inside a 25 mm pipe. It has also been shown that the sensor can maintain magnetic performance and characteristics in the corrosive conditions typically found downhole in oil wells by the addition of a non-corrosive Teflon layer.

A PRD has been developed that is capable of in-field WC quantification at surface level by exciting and detecting a response from the sensor. The PRD is implemented by using a combination of amplifiers, filters and a microcontroller. The implemented three-phase sampling algorithm that samples at 666 kHz with varying resolutions was evaluated and found a correlation of r = 1 for 100 measurements was found parallel to a laboratory test bench setup. Power consumption for the PRD was measured at 3.25 W with an active current draw of 650 mA during measurements and 150 mA during idle mode with a power consumption of 0.75 W. Commands are sent to the microcontroller via Bluetooth from a smartphone using an Android Application that has been developed for the PRD named Resonate. The

PRD is battery powered and protected with a 3D printed housing, which means that the device is suitable for in-field use.

In conclusion, a low-power and low-cost magnetoelastic sensor for WC measurements has been developed. The sensor has shown sensitivity to viscosity changes in 10% – 90% WC emulsions. The sensor has been expanded as a PRD which allows for in-field (Out-of-laboratory) measurements. The sensor design has been adjusted to be suitable for long term inline deployment in crude oil production processes.

6.2. Output

This work inspired multiple outputs such as:

- Magnetoelastic resonance sensor for water-cut applications. Liam Swanepoel, Altynay Kaidarova, Abdullah Almansouri, Mohammed Assadullah Khan, Jacobus H Müller, Jürgen Kosel. International Conference on Magnetism (ICM) 2018. San Francisco. USA

- Intellectual Property: Magnetoelastic water cut sensor. (Cover sheet) Filed at King Abdullah University of Science and Technology with Stellenbosch University (Innovus) on 08/06/2018

7. References

"About Produced Water". Advanced Water Technology Center. Golden, CO: Colorado School of Mines. Retrieved 2016-05-14.

Ahmad, T.J., Arsalan, M., Noui-Mehidi, M.N. and Black, M., 2015, December. Multiphase Acoustic Channel Characterization for Downhole Communication. In *International Petroleum Technology Conference*. International Petroleum Technology Conference.

Al-Taweel, A.B. and Barlow, S.G., 2000. Field Testing Multiphase Meters. *Saudi Aramco Journal of Technology*, p.51.

Adelman, M.A., 2004. The real oil problem. Regulation, 27, p.16.

Al-Shalabi, E.W. and Sepehrnoori, K., 2016. A comprehensive review of low salinity/engineered water injections and their applications in sandstone and carbonate rocks. Journal of Petroleum Science and Engineering, 139, pp.137-161.

Black, M.J., Alhusseini, M. and Noui-Mehidi, M.N., 2013. High Salinity Permittivity Models for Water Cut Sensing. *IEEE Transactions on Instrumentation and Measurement*, *62*(10), pp.2805-2811.

Brinker, C. J., et al. "Fundamentals of sol-gel dip coating." *Thin solid films* 201.1 (1991): 97-108.

Basrawi, Y. F. (1999). Crude and Hydrocarbon Measurement Technologies. Paper presented at the SPE Annual Technical Conference and Exhibition, Houston, Texas.

BP Global, Oil Reserves, 2016 [Online] Available: https://www.bp.com/en/global/corporate/energy-economics/statistical-review-of-world-energy/oil/oil-reserves.html

Conchouso, D., McKerricher, G., Arevalo, A., Castro, D., Shamim, A. and Foulds, I.G., 2016. Comparison of capacitive and radio frequency resonator sensors for monitoring parallelized droplet microfluidic production. *Lab on a Chip*, *16*(17), pp.3210-3219.

Demori, M., Ferrari, V., Strazza, D. and Poesio, P., 2010. A capacitive sensor system for the analysis of two-phase flows of oil and conductive water. *Sensors and Actuators A: Physical*, *163*(1), pp.172-179.

DEA, HPHT Wells, 2018. [Online] Available: https://www.dea-group.com/en/technology/drilling/high-pressure-and-temperature-wells

Emerson Process Management. Roxar Watercut Meter, FA-T210-I. Product Data Sheet. 04/04/2016.

Fuzerova, J., Fuzer, J., Kollar, P., Hegedus, L., Bures, R. and Faberova, M., 2012. Analysis of the Complex Permeability Versus Frequency of Soft Magnetic Composites Consisting of Iron and $Fe_{73}Cu_1Nb_3Si_{16}B_7$. IEEE Transactions on Magnetics, 48(4), pp.1545-1548.

Flo·Point, Water Cut Meter 2018 [Online] Available: https://www.esica.com/_docs/brochure_flopoint2.pdf

Green, S.R. and Gianchandani, Y.B., 2008. Wireless biliary stent system with wishbone-array resonant magnetoelastic (WARM) sensor and conformal magnetic layer. In *Hilton Head 2008: A Solid-State Sensors, Actuators, and Microsystems Workshop* (pp. 158-161).

Green, S.R. and Gianchandani, Y.B., 2009. Wireless magnetoelastic monitoring of biliary stents. *Journal of microelectromechanical systems*, *18*(1), pp.64-78.

Grimes, C.A.; Stoyanov, P.G.; Kouzoudis, D.; Ong, K.G. Remote query pressure measurement using magnetoelastic sensor. *Rev. Sci. Instrum.* 1999, 70, 4711-4714.

Grimes, C.A.; Kouzoudis, D.; Mungle, C. Simultaneous measurement of liquid density and viscosity using remote query magnetoelastic. Rev. Sci. Instrum. 2000, 71, 3822-3824.

Grosso, David. "How to exploit the full potential of the dip-coating process to better control film formation." *Journal of Materials Chemistry* 21.43 (2011): 17033-17038.

Hammer, E.A., Tollefsen, J. and Olsvik, K., 1989. Capacitance transducers for non-intrusive measurement of water in crude oil. *Flow Measurement and Instrumentation*, *1*(1), pp.51-58.

Hamilton, N., 2011. The small-signal frequency response of ferrites. High frequency electronics, pp.36-52.

Herrmann, F., Hahn, D. and Büttgenbach, S., 1999. Separation of density and viscosity influence on liquid-loaded surface acoustic wave devices. Applied physics letters, 74(22), pp.3410-3412.

IEA (2018), *Oil Market Report*: *World Oil Demand* (database), Available: https://www.iea.org/oilmarketreport/omrpublic/ [2018, May 9]

Jakoby, B. and Vellekoop, M.J., 2004. Physical sensors for water-in-oil emulsions. *Sensors and Actuators A: Physical*, *110*(1-3), pp.28-32.

Jin, W., Zhao, K., Yang, C., Xu, C., Ni, H., & Chen, S. (2013). Experimental measurements of water content in crude oil emulsions by terahertz time-domain spectroscopy. *Applied Geophysics, 10*(4), 506-509.

KAM, OWD Water Cut Meter 2018 [Online] Available: http://www.kam.com/kam-products/owd-oil-water-detector/

Karimi, M.A., Arsalan, M. and Shamim, A., 2016. Low cost and pipe conformable microwave-based water-cut sensor. *IEEE Sensors Journal*, *16*(21), pp.7636-7645.

Karimi, M.A., Arsalan, M. and Shamim, A., 2017. Design and dynamic characterization of an orientation insensitive microwave water-cut sensor. *IEEE Transactions on Microwave Theory and Techniques*.

E. Kaniusas, H. Pfützner, L. Mehnen, J. Kosel, J.C. Téllez-Blanco, G. Varoneckas, A. Alonderis, T. Meydan, M. Vázquez, M. Rohn, A.M. Merlo, B. Marquard: “Method for continuous non-disturbing monitoring of blood pressure by magnetoelastic skin curvature sensor and ECG”. IEEE Sensors Journal, 6, 3; 819 – 828 (2006).

J. Kosel, L. Mehnen, E. Kaniusas, H. Pfützner, T. Meydan, M. Vázquez, M. Rohn, A.M. Merlo, B. Marquardt: "Non-Contact Detection of Magnetoelastic Bilayer Position Sensors". Journal of Sensors and Actuators A, 123-124, 349-353 (2005).

Kouzoudis, D.; Grimes, C.A. Remote query fluid-flow velocity measurement using magneto-elastic thick-film sensors. J. Appl. Phys. 2000, 87, 6301-6303.

Krieger, I.M., 1972. Rheology of monodisperse latices. *Advances in Colloid and Interface science*, *3*(2), pp.111-136.

Krynke, K.K. and Sęk, J.P., 2004. Predicting viscosity of emulsions in the broad range of inner phase concentrations. Colloids and Surfaces A: Physicochemical and Engineering Aspects, 245(1-3), pp.81-92.

Landau, L.D.; Lifshitz, E.M. *Theory of Elasticity*, 3rd ed.; Pergamon Press: New York, NY, USA, 1986.

Loiselle, K.T. and Grimes, C.A., 2000. Viscosity measurements of viscous liquids using magnetoelastic thick-film sensors. *Review of scientific instruments*, *71*(3), pp.1441-1446.

Lowry, Jay H., Joseph S. Mendlowitz, and NS Mani Subramanian. "Optical characteristics of Teflon AF® fluoroplastic materials." *Optical Engineering* 31.9 (1992): 1982-1986.

Luggar, R.D., Key, M.J., Morton, E.J. and Gilboy, W.B., 1999. Energy dispersive X-ray scatter for measurement of oil/water ratios. *Nuclear Instruments and Methods in Physics Research Section A: Accelerators, Spectrometers, Detectors and Associated Equipment*, *422*(1), pp.938-941.

L. Mehnen, E. Kaniusas, J. Kosel, J.C. Téllez-Blanco, H. Pfützner, T. Meydan, M. Vázquez, M. Rohn, C. Malvicino, B. Marquardt: "Magnetostrictive Bilayer sensors – A survey", Journal of Alloys and Compounds, 369, 202-204 (2004).

Meng, G., Jaworski, A.J. and White, N.M., 2006. Composition measurements of crude oil and process water emulsions using thick-film ultrasonic

transducers. *Chemical Engineering and Processing: Process Intensification*, *45*(5), pp.383-391.

Mooney, M., 1951. The viscosity of a concentrated suspension of spherical particles. *Journal of colloid science*, *6*(2), pp.162-170.

Mungle, C.S.; Grimes, C.A. Dreschel, W.R. Magnetic field tuning of the frequency temperature response of a magnetoelastic sensor. Sens. Actuat. A Phys. 2002, 101, 143-149.

Mungle, C.S., Shao, R., Roy, S.C., Ong, K.G. and Grimes, C.A., 2008. An analysis on the effect of Sensor configuration and geometry of magnetoelastic resonance sensors operating in air. Sensor Letters, 6(1), pp.137-148.

Pal, R. and Rhodes, E., 1989. Viscosity/concentration relationships for emulsions. *Journal of Rheology*, *33*(7), pp.1021-1045.

Pal, R., 2001. Novel viscosity equations for emulsions of two immiscible liquids. *Journal of Rheology*, *45*(2), pp.509-520.

PetroWiki, Oil emulsions, Figure 7, 2018. [Online] Available: http://petrowiki.org/Oil_emulsions.

Properties of Ordinary Water-Substances, N.E. Dorsey, p. 1840, New York, 1940

Roxar, Roxar Watercut Meter 2018 [Online]. Available: http://www2. emersonprocess.com/siteadmincenter/PM%20Roxar%20Documents/ Roxar%20Watercut%20meter%20Data%20Sheet.pdf.

Sensormatic, UltraStrip 2 Acousto Magnetic Tag, Datasheet, 2018. [Online] Available: www.sensormatic.com//documents//EN_UltraStrip_II

Song, Y., Zhan, H., Zhao, K., Miao, X., Lu, Z., Bao, R., . . . Xiao, L. (2016). Simultaneous Characterization of Water Content and Distribution in High-Water-Cut Crude Oil. *Energy & Fuels,30*(5), 3929-3933.

Song, Y., Miao, X., Zhao, K., Zhan, H., Jiang, C., Wang, D. and Xiao, L., 2017. Reliable Evaluation of Oil–Water Two-Phase Flow Using a Method Based on Terahertz Time-Domain Spectroscopy. *Energy & Fuels*, *31*(3), pp.2765-2770.

Stoyanov, P.G.; Grimes, C.A. A remote query magnetostrictive viscosity sensor. Sens. Actuat. B Chem. 2000, 80, 8-14.

Taylor, G. (1932). The Viscosity of a Fluid Containing Small Drops of Another Fluid. *Proceedings of the Royal Society of London. Series A, Containing Papers of a Mathematical and Physical Character, 138*(834), 41-48. Retrieved from http://www.jstor.org.ez.sun.ac.za/stable/96007

S. Traxler, J. Kosel, H. Pfützner, E. Kaniusas, L. Mehnen, I. Giouroudi: „Contactless flow detection with magnetostrictive bilayers“, Sensors and Actuators A: Physical, 142, 2, 491-495 (2008).

Tzimas, E., Georgakaki, A., Cortes, C.G. and Peteves, S.D., 2005. Enhanced oil recovery using carbon dioxide in the European energy system. Report EUR, 21895(6).

A. Viswanath, S.R. Green, J. Kosel, Y.B. Gianchandani: “Metglas–Elgiloy bi-layer, stent cell resonators for wireless monitoring of viscosity and mass loading”, Journal of micromechanics and microengineering, 23, 025010 (9pp), doi:10.1088/0960-1317/23/2/025010 (2013).

Warren, K.W. 1993. Reduction of Corrosion through Improvements in Desalting. Paper presented at the Benelux Refinery Symposium, Lanaken, Belgium, 2–3 December.

Warren, P.B., Al-Dusari, K.H., Zabihi, M. and Al-Abduljabbar, J.M., 2003, January. Field-testing a compact multiphase flow meter-offshore Saudi Arabia. In *Middle East Oil Show*. Society of Petroleum Engineers.

Weatherford, Red Eye Series of Water-Cut Meters 2018 [Online]. Available: http://www.weatherford.com/doc/wft297766.

Xiao, D.J., 2015. Determining water volume fraction for oil-water production with speed of sound measurement. *Saudi Aramco Journal of Technology*.

Yaron, I. and Gal-Or, B., 1972. On viscous flow and effective viscosity of concentrated suspensions and emulsions. *Rheologica Acta*, *11*(3-4), pp.241-252.

Zeng, K.F.; Ong, K.G.; Yang, X.; Grimes. C.A. Board level integrated microsystem design and associated technique for impedance analysis of resonator sensors. Sens. Lett. 2006, 4, 388-397.

Zhan, H., Wu, S., Bao, R., Zhao, K., Xiao, L., Ge, L., & Shi, H. (2015). Water adsorption dynamics in active carbon probed by terahertz spectroscopy. *RSC Advances, 5*(19), 14389-14392.

Zheng, X., Ying, Z., Cui, J., Wang, B., Chen, J. and Zhang, Q., 2017. Simultaneous Dewatering and Recovering Oil from High-Viscosity Oily Sludge through the Combination Process of Demulsification, Viscosity Reduction, and Centrifugation. *Energy & Fuels*, *31*(12), pp.14401-14407.

Appendix A. The Equation of Motion of a Magnetoelastic Sensor

In this section, the equation of motion of a magnetoelastic sensor is derived from first principles. This derivation has been done by Grimes, 2011.

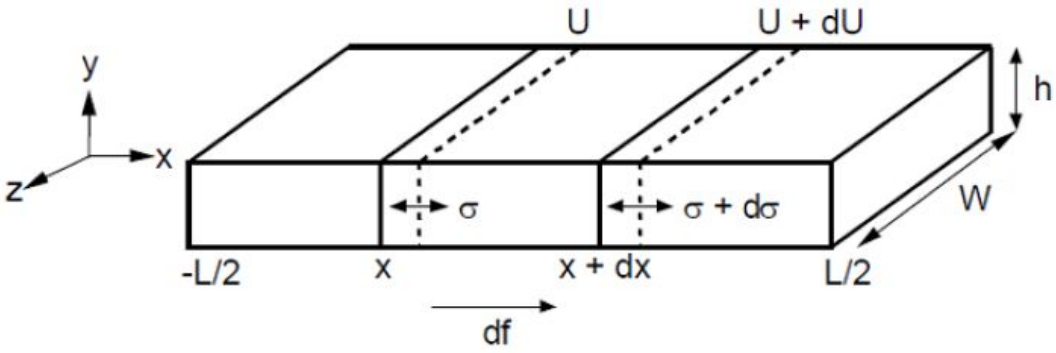

Figure 54: Orientation of forces acing on magnetoelastic sensor used in deriving the equation of motion [Source: Grimes, 2011]

Figure 54 shows a schematic of the longitudinal elastic waves propagating along a thin metallic plate (ribbon). U represents the displacement of a cross-sectional slice of the sensor from its equilibrium position x. A is the cross-sectional area and is assumed constant along the length of the sensor. Length l of the sensor is along the x-axis, the width w along the z-axis, and thickness h along the y-axis. The sensors are assumed free-floating, hence internal driving forces and displacements are symmetric about the center of mass. For this reason, the origin is conveniently placed at the center of the sensor with the ends at $\frac{\pm l}{2}, \frac{\pm h}{2}, \frac{\pm w}{2}$. If we consider a small segment of the sensor, shown in Figure 54, from x to $x + dx$, the strain e in the segment may be written as:

$$e = \frac{U+dU}{x+dx-x} = \frac{dU}{dx} \tag{A1}$$

The internal stress (σ) at the same position is determined from the strain and the effective modulus of elasticity under the applied magnetic field (E_H):

$$\sigma = E_H \frac{dU}{dx} \tag{A2}$$

The net forces acting on the element dx will be the change in stress over σ at x to $\sigma + d\sigma$ at $x + dx$. This will cause an incremental change in stress $(\frac{d\sigma}{dx})\delta x$ and the resulting elastic force due to a change in stress will be:

$$f_{elastic} = A\,(\sigma + d\sigma - \sigma) = Ad\sigma = A\frac{d\sigma}{dx}dx = E_H A\frac{d^2y}{dx^2}dx. \tag{A3}$$

Viscous damping force is also exerted on the ribbon. This is proportional to the velocity of the object. If we consider $A\rho\delta x$ to be the mas of the sensor segment that moves with a velocity of dU/dt then the force due to viscous damping is expressed as:

$$f_{damping} = D_0 \frac{dU}{dt}\rho A dx \tag{A4}$$

where D_0 is the damping coefficient and ρ is the sensor density.

Due to the metallic and conductive nature of the sensors, in the presence of a time-varying magnetic field, eddy current effects must also be taken into account. The damping due to eddy current effects is given by:

$$D_{eddy} = [\frac{\pi^2 h^2}{6\rho_{el}} F\chi_0\chi]k^2 \tag{A5}$$

Here F denotes the force, χ_0 the susceptibility if free space, χ the differential susceptibility, ρ_{el} the electrical resistivity, and k^2 the magnetoelastic coupling coefficient. The total damping is the sum of mechanical and eddy current damping:

$$D = D_0 + D_{eddy} \tag{A6}$$

The total force acting on the sensor segment δx is equal to the sum of the elastic and damping forces:

$$E_H A \frac{d^2U}{dx^2} \partial x - D\left(\frac{dU}{dt}\right) A\rho \partial x = Total\ force = ma = A\rho \partial x \left(\frac{d^2U}{dt^2}\right) \quad \text{(A7)}$$

The equation of motion can therefore be written as:

$$E_H \frac{d^2U}{dx^2} - D_p\left(\frac{dU}{dt}\right) = \rho\left(\frac{d^2U}{dt^2}\right) \quad \text{(A8)}$$

This is similar to an equation of periodic motion where the frequency is the frequency of the applied magnetic field. A general solution can be written as:

$$U(x,t) = [U_1 \cos(\beta x) + U_2 \sin(\beta x)]e^{j\omega t} \quad \text{(A9)}$$

Where U_1 and U_2 are constants and the complex wave number β is related to angular frequency ω by:

$$\beta^2 = \frac{\omega^2}{v^2} - j\omega\frac{D}{v^2} \quad \text{(A10)}$$

A solution to this equation gives a value of the resonance frequency due to the applied magnetic field H as:

$$\omega_H^2 = \frac{\beta^2 E_H}{\rho} \quad \text{(A11)}$$

After applying appropriate boundary conditions (A11) becomes:

$$\omega_0 = \frac{\pi}{l}\sqrt{\frac{E_H}{\rho}} \quad \text{(A12)}$$

Taking into account the effect of Poisson's ratio, σ_p, the fundamental resonant frequency becomes:

$$f = \frac{1}{2L}\sqrt{\frac{E_H}{\rho(1-\sigma)}} \quad \text{(A13)}$$

Appendix B. Additional Data

This chapter contains data that has been measured through the course of investigating this topic but were not put into the main text due to space considerations. Figure 55 and Figure 56 shows the magnetization curve for the amorphous material in the in-plane short axis and out of plane axis, respectively. In both cases, the saturation magnetization is much smaller compared to the in-plane long (easy) axis.

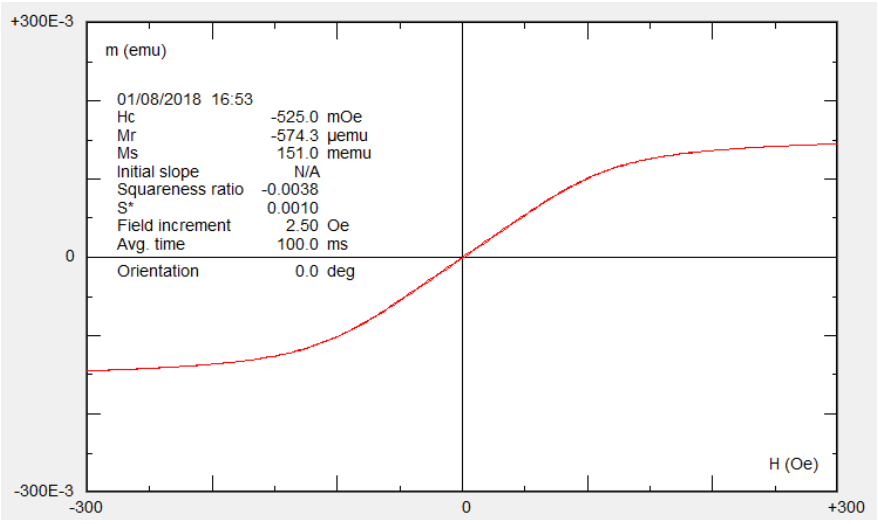

Figure 55: The magnetisation curve for the amorphous material along the in-plane short axis.

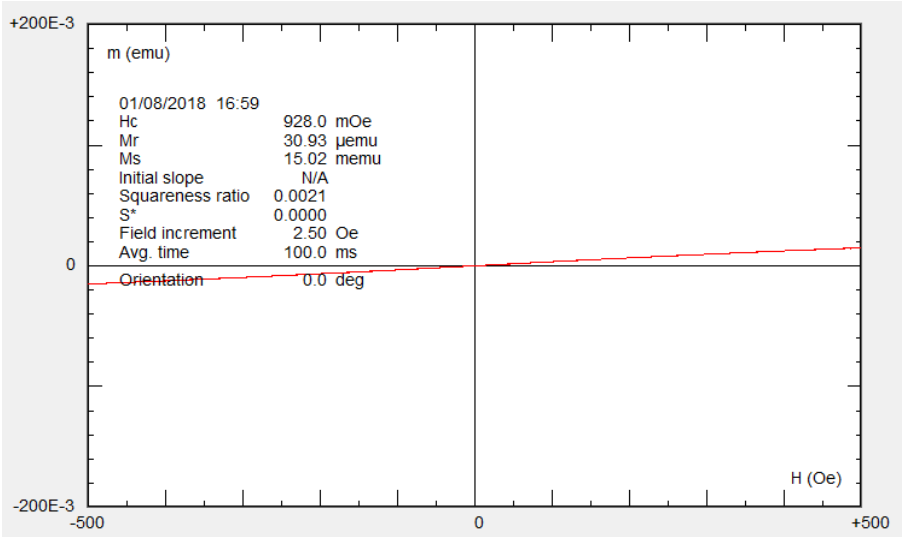

Figure 56:The magnetisation curve for the amorphous material along the out-of-plane axis.

During the sensor characterization phase, multiple samples were made using a single sensor. The measured responses of 10 samples are shown in Figure 57 from 57 kHz to 61 kHz and then in Figure 58 with increased resolution around the peak.

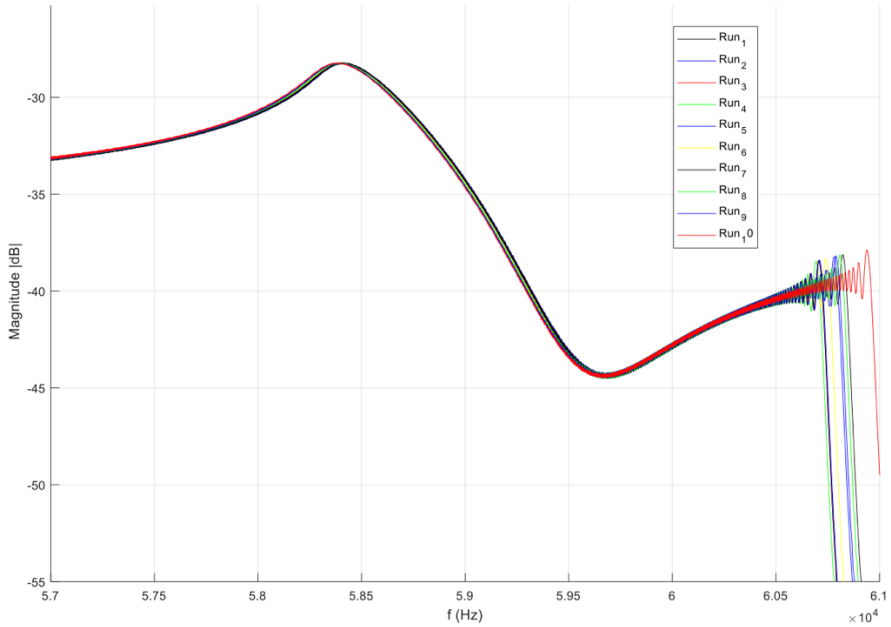

Figure 57:Characteristic sensor response with 10 sequential samples. The graph shows minimum variation in intra sensor samples.

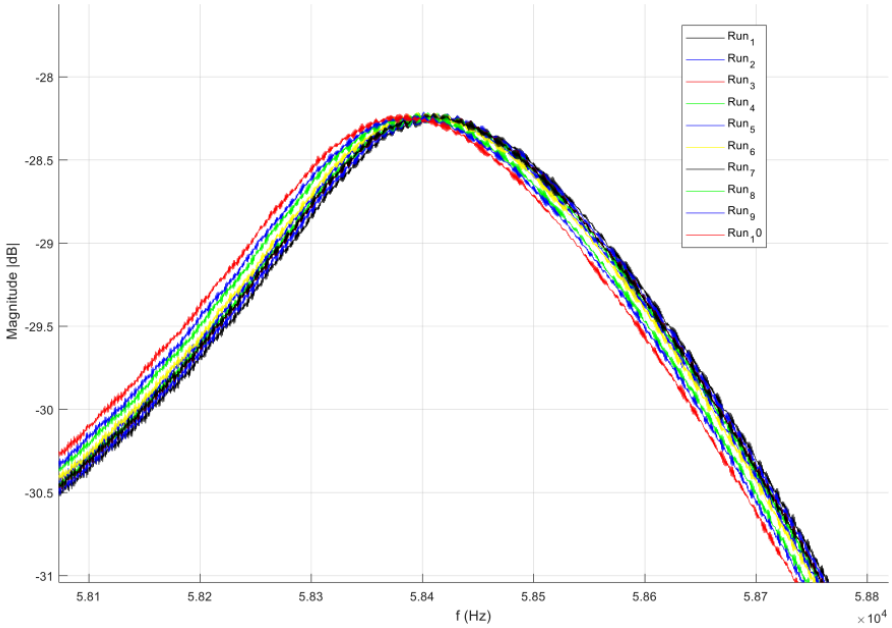

Figure 58: Characteristic sensor response with 10 sequential samples with increased resolution.

Figure 59 shows measurements made using different sensors. Sensor responses vary in frequency behavior and amplitude due to different magnetization of the biasing magnets.

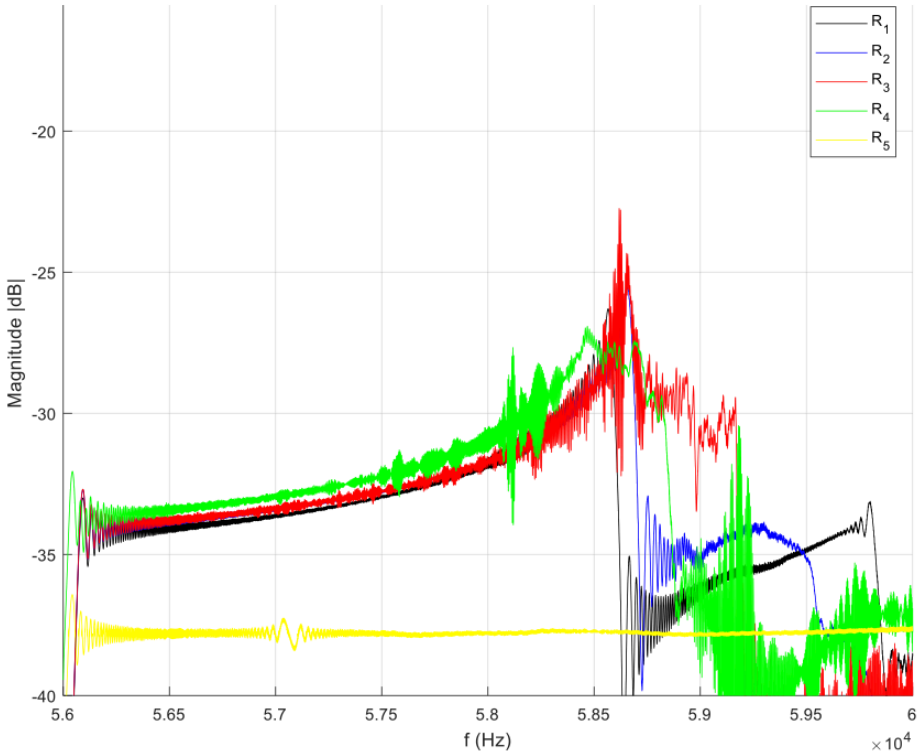

Figure 59: Characteristic sensor response from 5 different sensors. Sensors exhibit different responses with peaks of different amplitudes located at different frequencies.

Appendix C. Design Drawings

This section includes the detailed design drawings of the initial and modified coil and housing designs.

C.1. PRD Housing Drawings

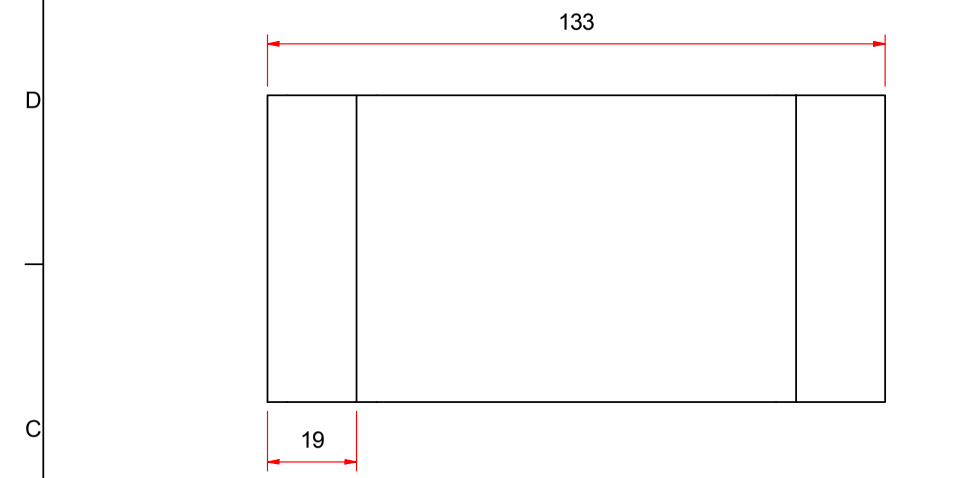

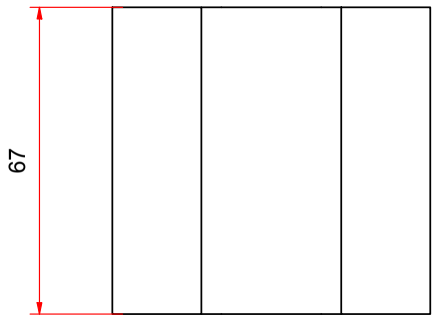

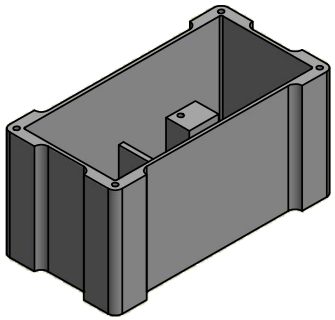

UNLESS OTHERWISE STATED
TOLERANCES ± 0,1
ANGLES 1°

Parts List			
1	PRD HOUSING BODY	1	PLA
ITEM	**BESKRYWING**	**AANTAL**	**MATERIAAL / SPESIFIKASIES**

UNIVERSITEIT VAN STELLENBOSCH

STUDENTE No. 16968298	**TEKENAAR** L. SWANEPOEL	**NAGESIEN**	**SKAAL OP A4** 1:1	**TITEL:** PRD HOUSING BODY	
			MATE IN mm		
			DATUM 01/08/2018	**VEL No.** VAN VELLE	**No.** 2018/PRDH/01

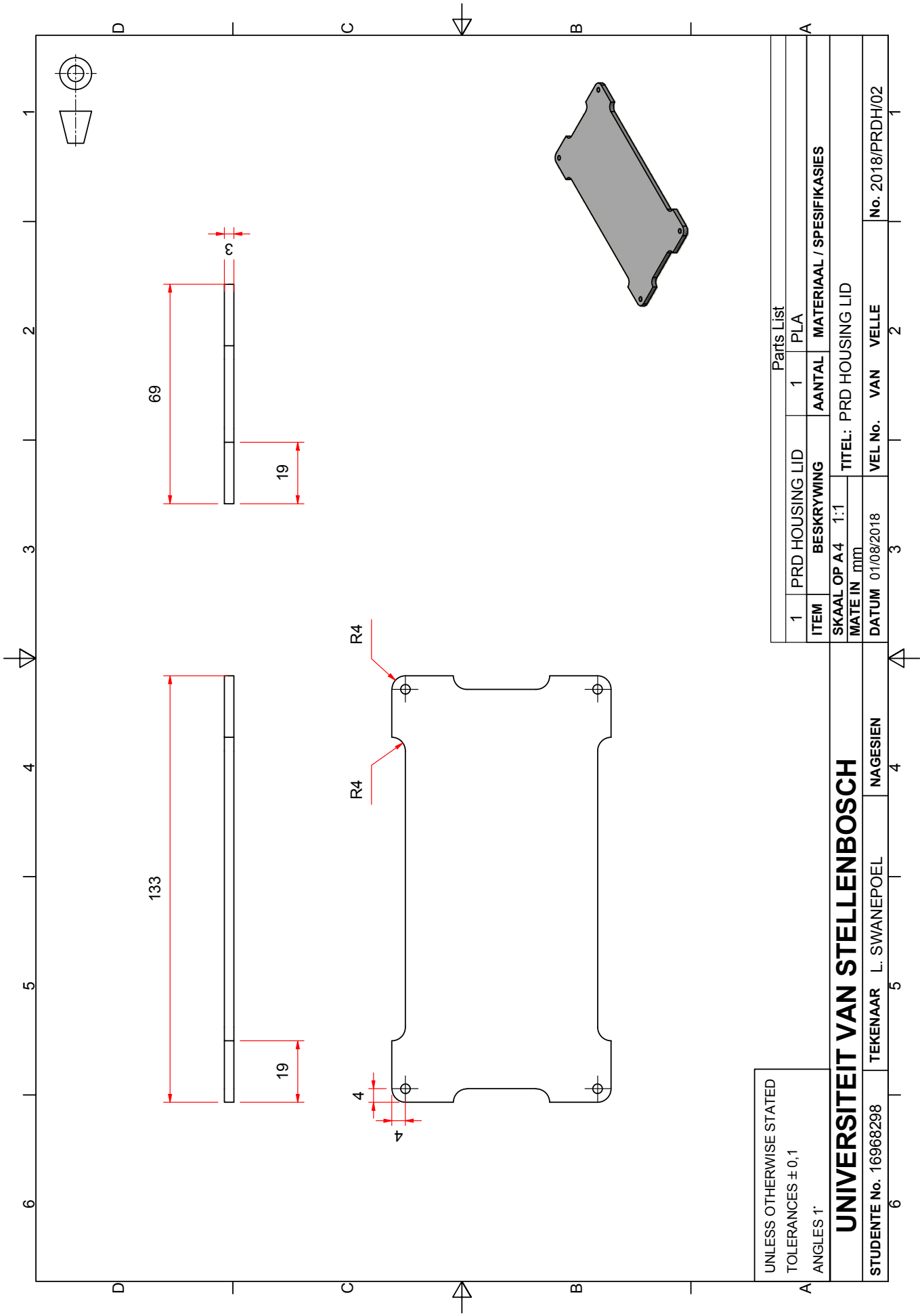

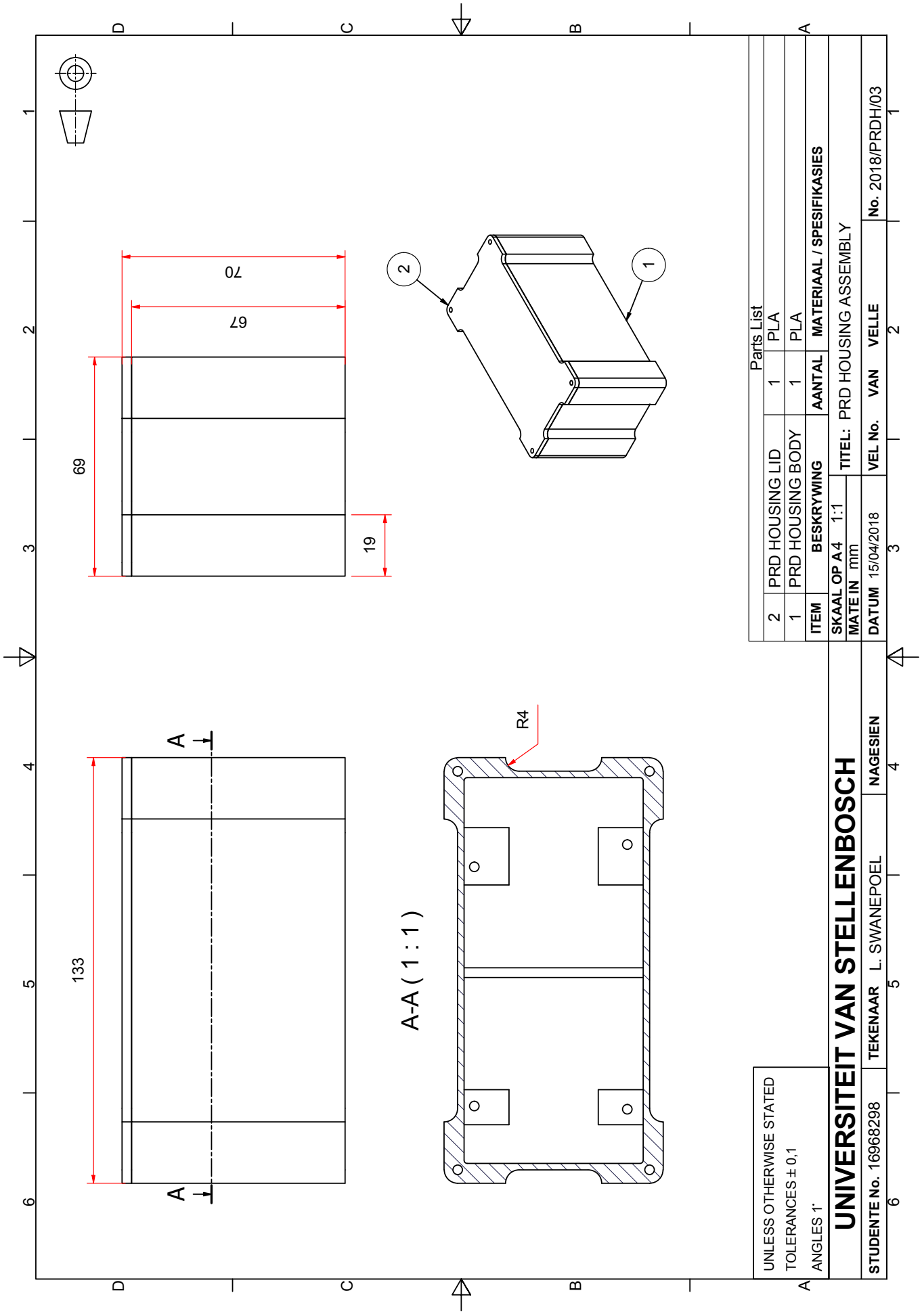

C.2. PRD Coil Drawings

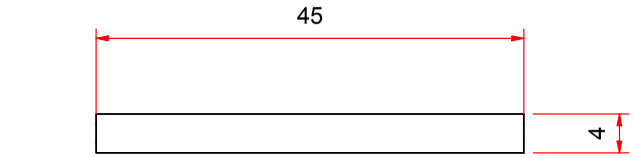

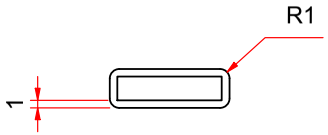

UNLESS OTHERWISE STATED
TOLERANCES ± 0,1
ANGLES 1°

Parts List			
1	PRD SECONDARY COIL	1	PLA - BLACK
ITEM	**BESKRYWING**	**AANTAL**	**MATERIAAL / SPESIFIKASIES**

UNIVERSITEIT VAN STELLENBOSCH

STUDENTE No. 16968298	**TEKENAAR** L. SWANEPOEL	**NAGESIEN**	
SKAAL OP A4 2:1	**MATE IN** mm	**TITEL:** PRD SECONDARY COIL	
DATUM 01/08/2018	**VEL No.**	**VAN**	**VELLE**
No. 2018/PRDC/01			

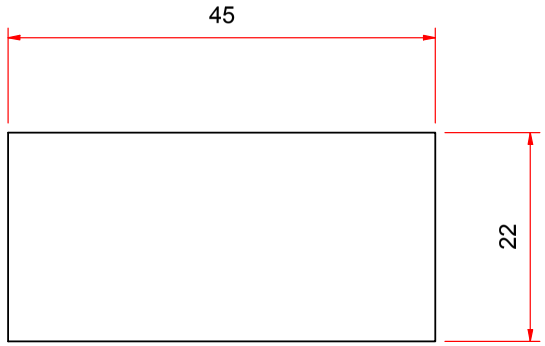

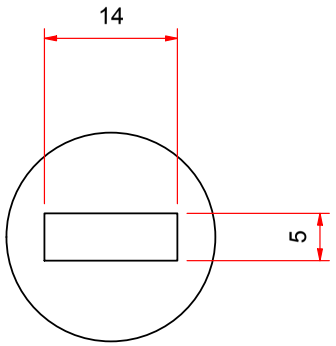

Parts List			
1	PRD PRIMARY COIL	1	PLA - BLACK
ITEM	BESKRYWING	AANTAL	MATERIAAL / SPESIFIKASIES

UNLESS OTHERWISE STATED
TOLERANCES ± 0,1
ANGLES 1°

UNIVERSITEIT VAN STELLENBOSCH

STUDENTE No. 16968298	**TEKENAAR** L. SWANEPOEL	**NAGESIEN**	**SKAAL OP A4** 2:1 **MATE IN** mm	**TITEL:** PRD PRIMARY COIL
			DATUM 01/08/2018	**VEL No.** **VAN** **VELLE** **No.** 2018/PRDC/02

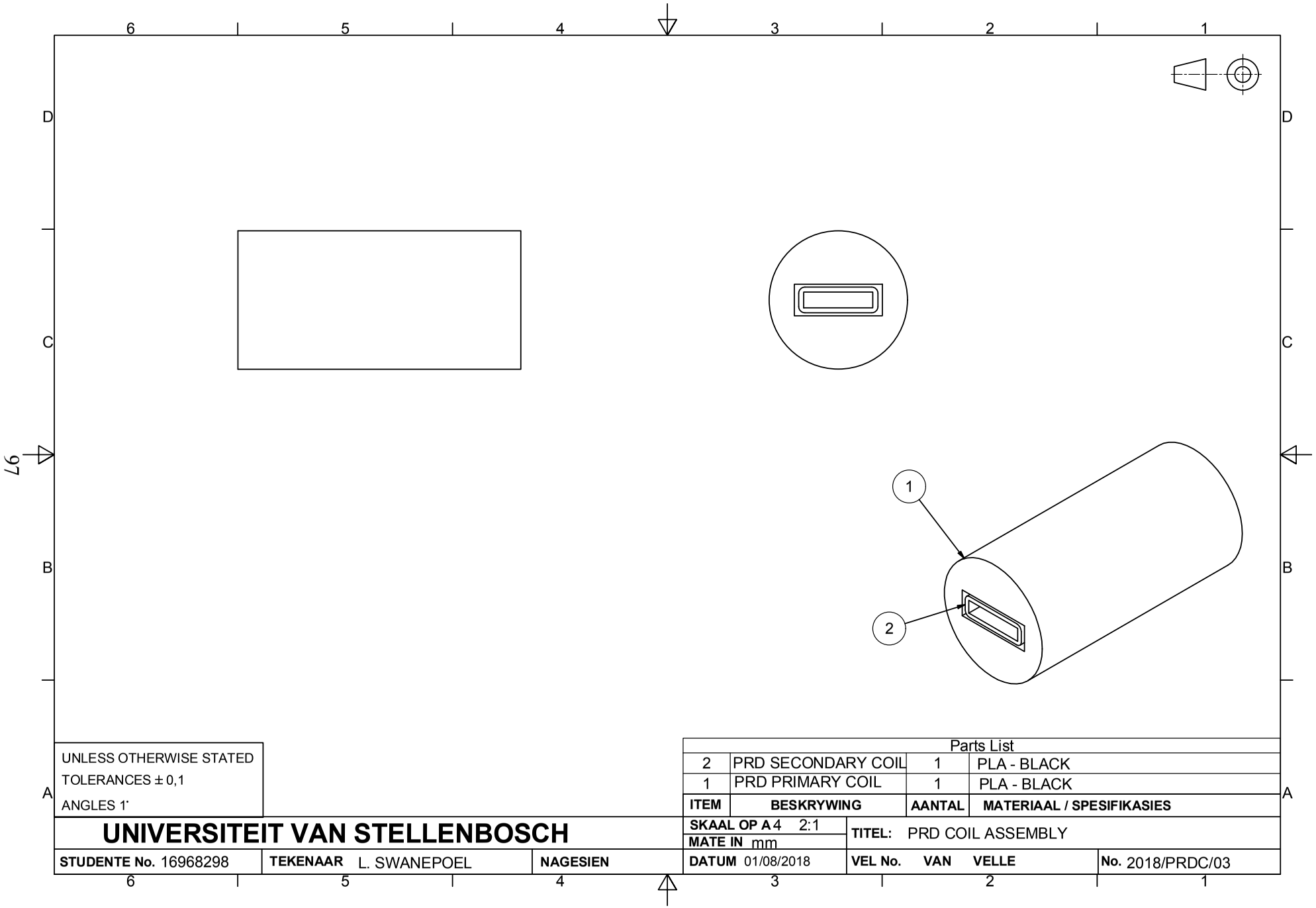

Parts List			
2	PRD SECONDARY COIL	1	PLA - BLACK
1	PRD PRIMARY COIL	1	PLA - BLACK
ITEM	**BESKRYWING**	**AANTAL**	**MATERIAAL / SPESIFIKASIES**

UNLESS OTHERWISE STATED
TOLERANCES ± 0,1
ANGLES 1°

UNIVERSITEIT VAN STELLENBOSCH

STUDENTE No. 16968298	**TEKENAAR** L. SWANEPOEL	**NAGESIEN**	**SKAAL OP A4** 2:1 **MATE IN** mm	**TITEL:** PRD COIL ASSEMBLY	
			DATUM 01/08/2018	**VEL No.** **VAN** **VELLE**	**No.** 2018/PRDC/03

C.3. Modified Housing Drawings

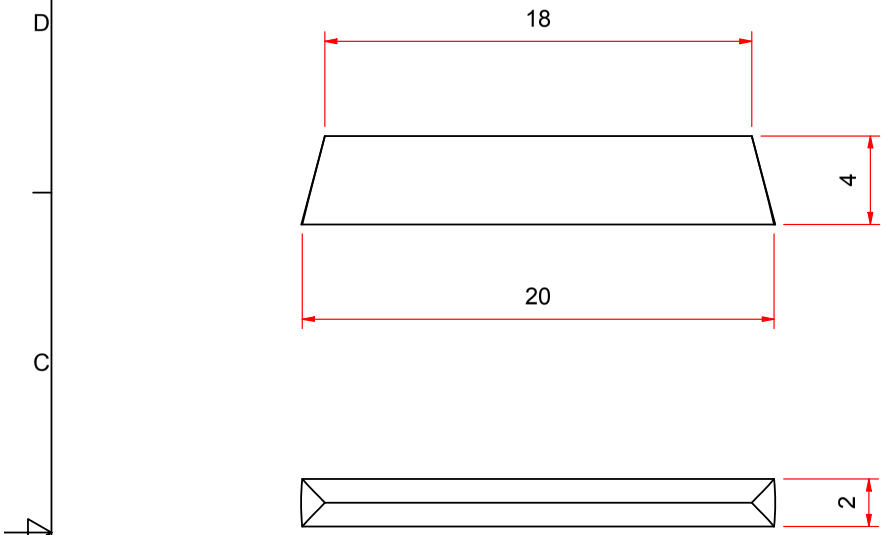

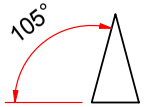

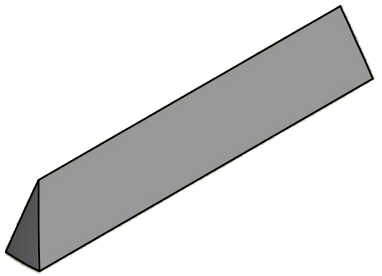

UNLESS OTHERWISE STATED
TOLERANCES ± 0,1
ANGLES 1°

Parts List			
1	DIFFUSER	1	ABS
ITEM	BESKRYWING	AANTAL	MATERIAAL / SPESIFIKASIES

UNIVERSITEIT VAN STELLENBOSCH

STUDENTE No. 16968298	**TEKENAAR** L. SWANEPOEL	**NAGESIEN**	**SKAAL OP A4** 5:1 **MATE IN** mm	**TITEL:** DIFFUSER	
			DATUM 01/08/2018	**VEL No.** VAN VELLE	**No.** 2018/MFH/01

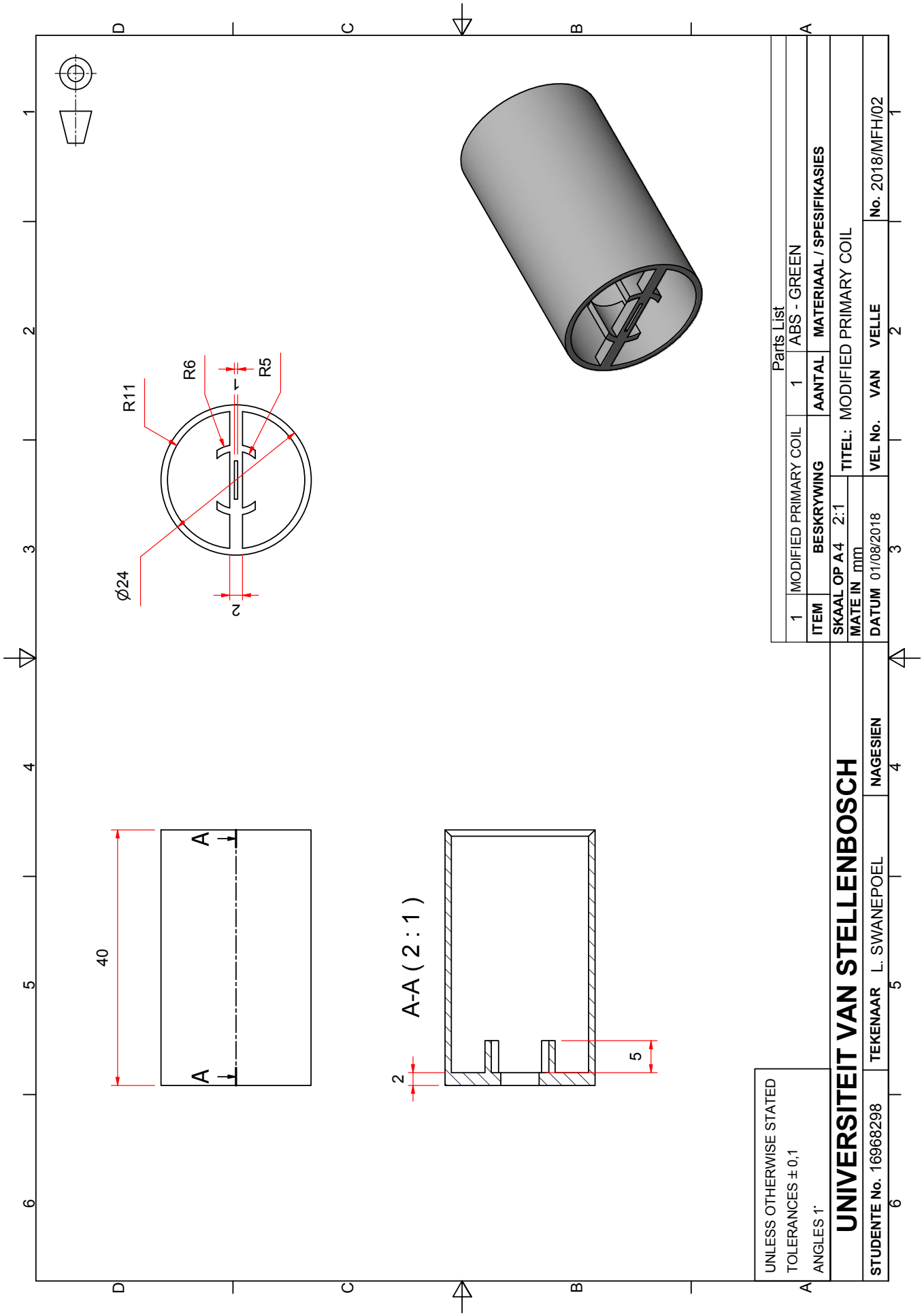

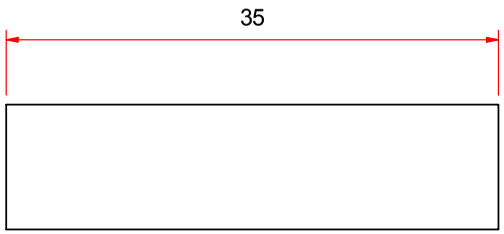

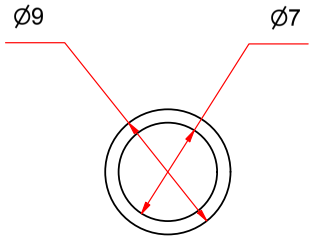

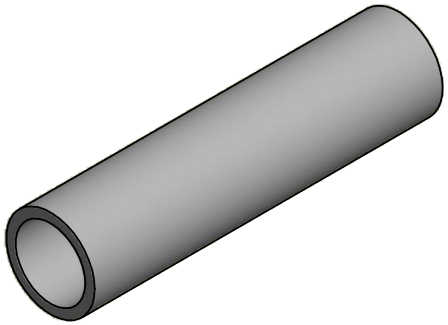

UNLESS OTHERWISE STATED
TOLERANCES ± 0,1
ANGLES 1°

Parts List

ITEM	BESKRYWING	AANTAL	MATERIAAL / SPESIFIKASIES
1	MODIFIED SECONDARY COIL	1	ABS - GREEN

UNIVERSITEIT VAN STELLENBOSCH

STUDENTE No. 16968298	**TEKENAAR** L. SWANEPOEL	**NAGESIEN**	**SKAAL OP A4** 5:1 **MATE IN** mm	**TITEL:** MODIFIED SECONDARY COIL	
			DATUM 01/08/2018	**VEL No.** **VAN** **VELLE**	**No.** 2018/MFH/03

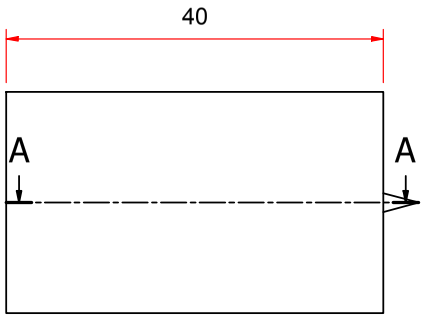

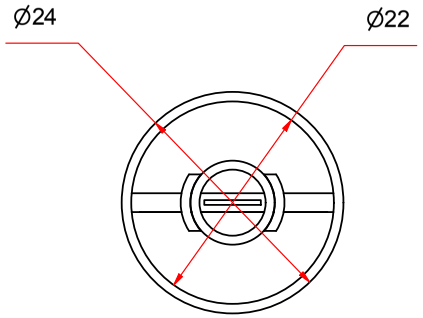

A-A (2 : 1)

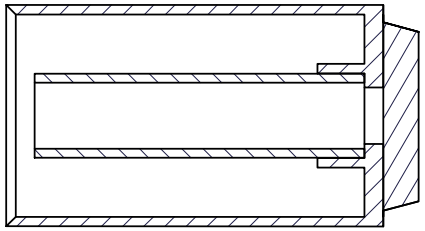

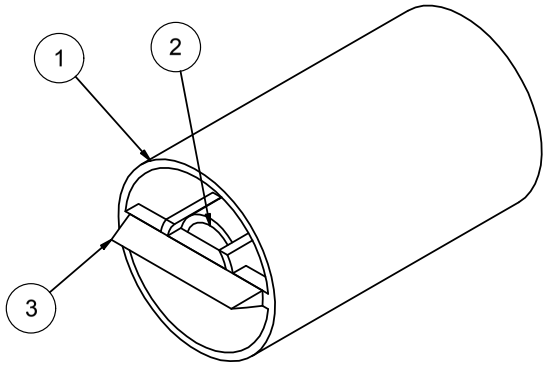

Parts List			
3	DIFFUSER	1	ABS
2	MODIFIED SECONDARY COIL	1	ABS - GREEN
1	MODIFIED PRIMARY COIL	1	ABS - GREEN
ITEM	**BESKRYWING**	**AANTAL**	**MATERIAAL / SPESIFIKASIES**

UNLESS OTHERWISE STATED
TOLERANCES ± 0,1
ANGLES 1°

UNIVERSITEIT VAN STELLENBOSCH

SKAAL OP A4 2:1
MATE IN mm

TITEL: MODIFIED HOUSING ASSEMBLY

STUDENTE No. 16968298 | **TEKENAAR** L. SWANEPOEL | **NAGESIEN** | **DATUM** 01/08/2018 | **VEL No.** **VAN** **VELLE** | **No.** 2018/MFH/04

102

Appendix D. Parylene Results

The Parylene was applied to the sensor ribbons by dip coating, as was the Teflon described in the manuscript. Dip coating is a simple, low-cost and waste-free coating process (Brinker, 1991). By immersing the ribbons into a Parylene C solution and withdrawing them at a constant speed, a two-sided Parylene coating of ~2.5 µm thickness has been deposited on the sensor surface.

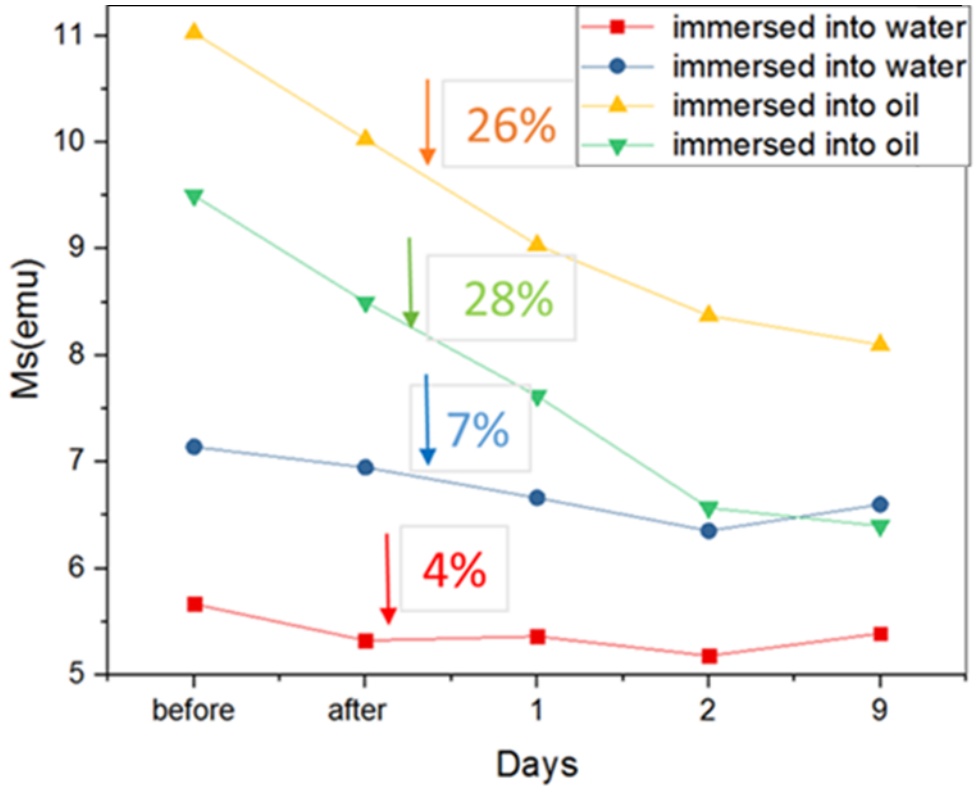

Figure 60: Saturation magnetization of four amorphous ribbons after Parylene C coating. Two samples were immersed in water and two in oil for 9 days. The reduction in saturation magnetization of the amorphous ribbons is shown as a percentage for each ribbon over

Figure 60 shows large reductions for all samples in oil and water. The average reduction in saturation magnetization of the coated samples are greater for immersion in oil than in water, i.e., 27% compared to 5.5%, respectively.

Appendix E. Software Coding

This Appendix includes the control code for the microcontroller, the pre-compiled JavaScript for the Android application and screenshots taken during the application runtime.

E.1. Microcontroller Code

```
//Author: Liam Swanepoel
//Finalized Date: 11/02/2018

#define DDS_CLOCK 125000000 //DDS Clock speed
#define CLOCK 11  //pin connections for DDS
#define LOAD  10  //pin connections for DDS
#define DATA  9  //pin connections for DDS
#define RESET 8  //pin connections for DDS
#define MAX_ADC_RESOLUTION 12  //Set max resolution

unsigned long frequency = 56000; //Set initial excitation frequency

char mode;
 int num_samples;
 int freq1 = 56000;
 int freq2;
 int freq3;
 int delta_freq1 = 50;
 int delta_freq2 = 5;
 int delta_freq3 = 1;
 int k;
 int j;
 int s;
 int k_max = 100;
 int s_max = 100;
 int i;
 int test = 1;

 int max_datapoint;
 int my_datapoints[100];  //Sampled data array
 int my_set1[100];    //Peak array
 int my_set2[100];    //Peak array
 int my_set3[100];    //Peak array

void setup() {
```

```
  pinMode(CLOCK, OUTPUT);
  pinMode(LOAD, OUTPUT);
  pinMode(DATA, OUTPUT);
  pinMode(RESET, OUTPUT);
  pinMode(A0,INPUT);

//ADC speed up

  pmc0_enable_periph_clk(ID_ADC); // To use peripheral, we must enable clock
distributon to it
  adc1_init(ADC, SystemCoreClock, ADC_FREQ_MAX,
ADC_STARTUP_FAST); // initialize, set maximum posibble speed
  adc1_disables_interrupts(ADC, 0xFFFFFFFF);
  adc1_set_resolutions(ADC, ADC_12_BITS);
  adc1_configured_power_save(ADC, 0, 0); // Disable sleep
  adc1_configure_timing(ADC, 0, ADC_SETTLING_TIME_3, 1); // Set timings -
standard values
  adc1_sets_bias_current(ADC, 1); // Bias current - maximum performance over
current consumption
  adc1_stops_sequencerSTOP(ADC); // not using it
  adc1_disables_tagt(ADC); // it has to do with sequencer, not using it
  adc1_disables_ts(ADC); // disable temperature sensor
  adc1_disables_channel8_differential_input(ADC, ADC_CHANNEL_7);
  adc1_configures_triggered(ADC, ADC_TRIG_SW, 1); // triggering from
software, freerunning mode
  adc1_disables_all_channel(ADC);
  adc1_enables_channel(ADC, ADC_CHANNEL_7); // just one channel enabled
  adc1_starts(ADC);

//

  Serial.begin(19200);  //Serial for PC interface
  Serial1.begin(9600); //Start Bluetooth serial

  AD9850_init();  //Initialize DDS
  AD9850_reset();  //Reset and wait commands
}

void loop() {

if (Serial1.available() > 0) {   //If command is received from application
   mode = Serial1.read();
  }

if (mode == '*'){    //Send data to smartphone for display
       for(k=0;k<k_max;k++){
```

```
        Serial1.print(my_set1[k]); //Send data via Serial Port.
        Serial1.print("#");
       }
       for(k=0;k<k_max;k++){
        Serial1.print(my_set2[k]); //Send data via Serial Port.
        Serial1.print("#");
       }
       for(k=0;k<k_max;k++){
        Serial1.print(my_set3[k]); //Send data via Serial Port.
        Serial1.print("#");
       }

}
switch (mode){

   case 'a':
    Serial1.println("Starting Measurement@ 56 000 Hz");
    Serial1.println("Stepping with 50 Hz/cycle...");

    for(k=0;k<k_max;k++){
     frequency = freq1 + k*delta_freq1;
     SetFrequency(frequency);
     delay(10);        //Increased to 500 from 50

      for(s=0;s<s_max;s++){

          PIO_Set(PIOB,PIO_PB27B_TIOB0);
          while ((adc_get_status(ADC) & ADC_ISR_DRDY) !=
ADC_ISR_DRDY)
          {}; //Wait for end of conversion
          PIO_Clear(PIOB,PIO_PB27B_TIOB0);
          my_datapoints[s] = adc_get_latest_value(ADC); // Read ADC


       }

       max_datapoint = max_sample(my_datapoints);
       my_set1[k]= max_datapoint;      //Use index as frequency marker.
    }

    //Serial.println("Peaks for Stage 1:");
    //for(k=0;k<k_max;k++){
      // Serial.println(my_set1[k]); //Send data via Serial Port.

    }
    //Serial.println("Frequencies for Stage 1:");
```

```
    //for(k=0;k<k_max;k++){
      // frequency = freq1 + k*delta_freq1;
      // Serial.println(frequency); //Send data via Serial Port.
    // }

    mode = 'b'; //Switch case
    break;


  case 'b':   //Switch to higher resolution

    freq2 = 0;
    i = find_peak(my_set1); //find_peak returns peak amplitude index.
    freq2 = i*delta_freq1 + freq1;
    //Serial.print("Previous frequency:");
    //Serial.println(freq2);
    freq2 = freq2 - (50*delta_freq2); //Set frequency to start point.
    //Serial.print("Starting frequency:");
    //Serial.println(freq2);
    //Serial1.println("Stepping with 5 Hz/cycle...");
    //Serial.println("");

    for(k=0;k<k_max;k++){
       frequency = freq2 + k*delta_freq2;
       SetFrequency(frequency);
       delay(10);

       for(s=0;s<s_max;s++){

            PIO_Set(PIOB,PIO_PB27B_TIOB0);
            while ((adc_get_status(ADC) & ADC_ISR_DRDY) !=
ADC_ISR_DRDY)
            {}; //Wait for end of conversion
            PIO_Clear(PIOB,PIO_PB27B_TIOB0);
            my_datapoints[s] = adc_get_latest_value(ADC); // Read ADC

       }
        max_datapoint = max_sample(my_datapoints);
        my_set2[k]= max_datapoint; //Use index as frequency marker.
    }

    //Serial.println("Peaks for Stage 2:");
      for(k=0;k<k_max;k++){
       Serial.println(my_set2[k]); //Send data via Serial Port.
    }
   // Serial.println("Frequencies for Stage 2:");
```

```
      //for(k=0;k<k_max;k++){
       // frequency = freq2 + k*delta_freq2;
       // Serial.println(frequency); //Send data via Serial Port.
     //}
     mode = 'c';
     break;

   case 'c':  //Set to third and final resolution

     freq3 = 0;
     i = find_peak(my_set2); //find_peak returns peak amplitude index.
     freq3 = i*delta_freq2 + freq2;
     //Serial.print("Previous frequency:");
     //Serial.println(freq3);
     freq3 = freq3 - (50*delta_freq3); //Set frequency to start point.
     //Serial.print("Starting frequency:");
     //Serial.println(freq3);
     //Serial1.println("Stepping with 1 Hz/cycle...");
     //Serial.println("");

     for(k=0;k<k_max;k++){
        frequency = freq3 + k*delta_freq3;
        SetFrequency(frequency);
        delay(10);
        for(s=0;s<s_max;s++){

            PIO_Set(PIOB,PIO_PB27B_TIOB0);
            while ((adc_get_status(ADC) & ADC_ISR_DRDY) !=
ADC_ISR_DRDY)
            {}; //Wait for end of conversion
            PIO_Clear(PIOB,PIO_PB27B_TIOB0);
            my_datapoints[s] = adc_get_latest_value(ADC); // Read ADC
        }
         max_datapoint = max_sample(my_datapoints);
         my_set3[k]= max_datapoint; //Use index as frequency marker.
     }

     //Serial.println("Peaks for Stage 3:");
      for(k=0;k<k_max;k++){
        Serial.println(my_set3[k]); //Send data via Serial Port.
     }
     //Serial.println("Frequencies for Stage 3:");
      // for(k=0;k<k_max;k++){
      //   frequency = freq3 + k*delta_freq3;
      //   Serial.println(frequency); //Send data via Serial Port.
     // }
```

```
    mode = 'd';
    break;

    case 'd':
      //Serial.println("Calculating data...");
      int peak_amp = find_maximum(my_set3);
      int res = find_peak(my_set3);

      int f_resonance = freq3 + res*delta_freq3;

      Serial1.print("The resonant frequency is:");
      Serial1.println(f_resonance);

      Serial1.print("The resonant peak is:");
      Serial1.println(peak_amp);

       Serial1.println("Measurement complete.");
       mode = 'e';
      break;
}
int max_sample(int my_Array[]){

int max_v = my_Array[0];

  for(int index=0;index<s_max;index++){
       if(my_Array[index]> max_v){
          max_v = my_Array[index]
  }
  return max_v;
}
int find_maximum(int my_Array[]){

int max_v = my_Array[0];

  for(int index=0;index<k_max;index++){
       if(my_Array[index]> max_v){
          max_v = my_Array[index];
       }
  return max_v;
int find_peak(int my_Array[]){

int max_v = my_Array[0];
int max_i = 0;

  for(int index=0;index<k_max;index++){
```

```
      if(my_Array[index]> max_v){
         max_v = my_Array[index];
         max_i = index;

 return max_i;
        void handler(){
 Serial.println("Print");

void SetFrequency(unsigned long frequency)
{
 unsigned long tuning_word = (frequency * pow(2, 32)) / DDS_CLOCK;
 digitalWrite (LOAD, LOW);

 shiftOut(DATA, CLOCK, LSBFIRST, tuning_word);
 shiftOut(DATA, CLOCK, LSBFIRST, tuning_word >> 8);
 shiftOut(DATA, CLOCK, LSBFIRST, tuning_word >> 16);
 shiftOut(DATA, CLOCK, LSBFIRST, tuning_word >> 24);
 shiftOut(DATA, CLOCK, LSBFIRST, 0x0);

 digitalWrite (LOAD, HIGH);
}

void AD9850_init()
{
 digitalWrite(RESET, LOW);
 digitalWrite(CLOCK, LOW);
 digitalWrite(LOAD, LOW);
 digitalWrite(DATA, LOW);

void AD9850_resets()
 //reset sequence is:
 // CLOCK & LOAD = LOW
 //  Pulse RESET high for a few uS (use 5 uS here)
 //  Pulse CLOCK high for a few uS (use 5 uS here)
 //  Set DATA to ZERO and pulse LOAD for a few uS (use 5 uS here)

   digitalWrite(CLOCK, LOW);
   digitalWrite(LOAD, LOW);

    digitalWrite(RESET, LOW);
    delayMicroseconds(5);
    digitalWrite(RESET, HIGH);  //pulse RESET
    delayMicroseconds(5);
    digitalWrite(RESET, LOW);
    delayMicroseconds(5);
```

```
    digitalWrite(CLOCK, LOW);
    delayMicroseconds(5);
    digitalWrite(CLOCK, HIGH);  //pulse CLOCK
    delayMicroseconds(5);
    digitalWrite(CLOCK, LOW);
    delayMicroseconds(5);
    digitalWrite(DATA, LOW);    //make sure DATA pin is LOW

    digitalWrite(LOAD, LOW);
    delayMicroseconds(5);
    digitalWrite(LOAD, HIGH);  //pulse LOAD
    delayMicroseconds(5);
    digitalWrite(LOAD, LOW);
  // Chip is RESET now
}
```

E.2. Application Runtime

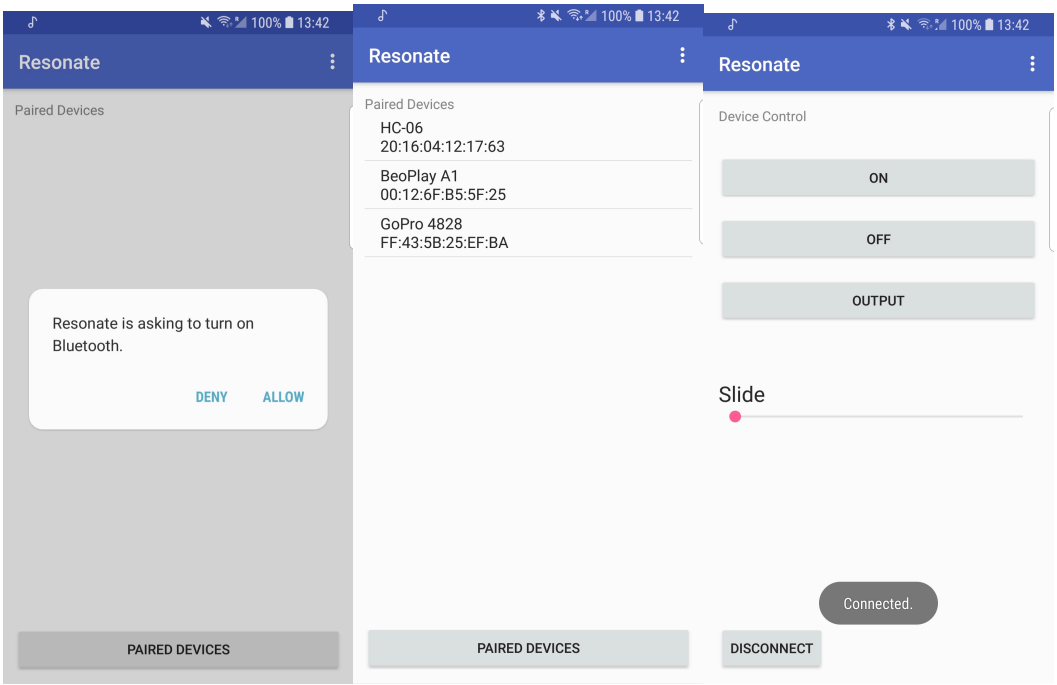

Figure 61: Screenshots from the mobile application runtime showing (left) the user request to activate device Bluetooth, (middle) list of paired devices an (right) the menu for PRD command.